POLITECNICO
MILANO 1863

SCUOLA DI INGEGNERIA INDUSTRIALE
E DELL'INFORMAZIONE

EXECUTIVE SUMMARY OF THE THESIS

Rate-rule development for recombination reactions of large Polycyclic Aromatic Hydrocarbons (PAHs) based on ab-initio quantum chemistry calculations

TESI MAGISTRALE IN CHEMICAL ENGINEERING – INGEGNERIA CHIMICA

AUTHOR: VERONICA VARINI

ADVISOR: Prof. MATTEO PELUCCHI

ACADEMIC YEAR: 2020-2021

1. Introduction

The formation of solid carbon nanoparticles from reacting gases is of interest to a wide range of scientific, technological, and societal problems, including air quality, global climate, human health, and material synthesis. The continuous increase of world energy demand is nowadays one of the main focuses from an environmental point of view especially in those countries where the phenomenon of fast-growing economies is present [1]. The generation by combustion processes of airborne species of current environment and health concern such as Polycyclic Aromatic Hydrocarbons (PAHs) and soot particles necessitates a detailed understanding of chemical reaction pathways responsible for their formation [2]. The soot formation mechanism is not consolidated, and it is still object of investigation starting from some key precursors such as PAHs, which play an important role in soot nucleation as recognized since the mid of 1980s. The first model developed by Frenklach and co-workers is still considered a pioneer step toward the use of detailed kinetic models to describe PAH and soot formation in incomplete combustion conditions [3]. Over the years one of the main focuses has been the transition from gaseous PAHs to "solid" carbonaceous particles referred to as soot nucleation. The formation of soot is a complex process involving gas-phase chemical kinetics, heterogeneous reactions on the particle surface, and particle dynamics. Nucleation mechanism is just one of the steps involved in soot formation. To reach a deep comprehension of soot reactivity many studies have been carried out. It is widely accepted that, in sooting environments, Resonantly Stabilized Radicals (RSR) are abundant, and they grow and cluster together with hydrocarbons and other radicals. Once formed, soot nuclei continue to grow via surface chemical reactions, PAH condensation and particle agglomeration. Particle's coalescence drives to larger structures while the growth firstly come from PAHs deposition on the surface of smaller ones and because of absorption of gas-phase on the solid surface of soot the result is like stacking of PAHs. After the first core of soot is formed it collides to

generate bigger structures in the coagulation process. Coalescence occurs when two particles collide and merge to form a single larger particle. The coalescence process tends to reduce free surface to minimize free energy. Following coagulation, agglomeration occurs, and particles collide sticking to each other to form chain-like fractal structures. Agglomerated structured reached at the end of the process are spot like particles. Soot oxidation process needs also to be considered in the modeling approach being of relevant importance as it is competitive to soot growth [4].

The purpose of this work is to build on a reactivity and bond energy analysis by estimating the rate constants for cross-linking reactions between PAHs of different types. Different reactive edges are going to be considered, such as σ-radicals and π-radicals, for a rate-rule development to describe the reactivity of larger PAHs assuming smaller structures as reference. A wide range of species and correlated reactions are lumped according to the reactive edges and the corresponding kinetic parameters will be implemented in the CRECK kinetic mechanism for soot formation as a validation trial, the final goal is an accurate match of experimental data to correctly represent by modeling techniques this complex phenomena.

2. Methodology

In this work all the calculations performed to predict the electronic structure of reacting molecules and the treatments of chemical kinetics are carried out using the EStokTP framework [5] [6]. Providing molecular structures as input the main purpose of the tool is the prediction of rate constants for some classes of reactions. EStokTP allows to perform electronic structure optimization and master equation calculations in a fully integrated manner, but it can be useful also to investigate the Potential Energy Surfaces (PES). Ab-initio electronic structure calculation have been performed using DFT in Gaussian09. Simulations at level 0 and level 1, in this work, have been performed for recombination reactions with the M062X functional and the 6–311+G(d,p) basis set. The M062X method has been selected as it is suitable to describe chemical kinetics with reasonable accuracy [7]. Density functional theory has been employed in conjunction with canonical transition state theory (TST) and variational theory (VTST) to provide an initial estimate for the rate constants and of the cross-linking reactions considered to analyze which are likely to be relevant at flame temperatures (T>1200 K). The EStokTP routine for rate constants computation has been exploited dealing with reactions with an energy barrier, where PES exploration is followed by master equation calculations using the MESS program [8]. Counter wise, rate constants computation for barrierless reactions requires PES reconstruction to locate the minimum flux of reactants molecules, according to the variational formulation of TST (VTST). This procedure provides much higher computational effort adopting the broken-symmetry approach as a good compromise being, in any case, less expensive than a multi-reference study for such large structures, i.e. PAHs. The unrestricted DFT, i.e., UM06-2X/6–311+G(d,p) need to be implemented to correctly account for long-distance correlation energy [9] [10]. The kinetic parameters computed as mentioned above are then implemented in the CRECK kinetic mechanism. The aim is to track the evolution from parent molecule to multi-ring PAHs and, ultimately, to soot, in a highly controlled flame under incipient soot conditions, to ensure compatibility of the diagnostics with soot load. The structure of the flames is computed using 1-D governing equations and so 1-D laminar flames configurations, i.e., premixed burner-stabilized, premixed burner-stabilized stagnation and counterflow diffusion flames. Laminar flame governing equations have been solved as implemented in the OpenSMOKE++ suite of programs [11].

3. PAHs Reactivity Investigation and Rate Rule Development

Several different types of PAHs with different reactive edges are known to exist and they play an important role in soot formation also by means of dimerization reactions [12]. Monomers interact and cluster together to form incipient soot starting from flat and curved PAHs [13]. In this work three classes of PAHs have been investigated and considered as monomers, i.e., σ-radicals and π-radicals considering both scenario of localized and delocalized radicals, which are of interest because of their propensity to dimerize, owing to their high concentration in high T combustion environment [14]. The structures considered in this study are

those reported in Figure 1 grouped according to the radical delocalization character. The radicals of types A (aryl σ-radicals), B (localized π-radicals), and C (delocalized π-radicals) presented in Figure 1 recombine leading to dimers formation, starting from these 5 monomers 15 dimers have been investigated spacing from 9 to 26 carbon-atoms.

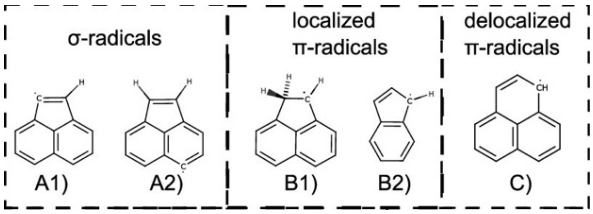

Figure 1: PAH monomers adopted from [15].

Geometry optimization and electronic energy computation have been carried out to compute Bond Dissociation Energy (BDE) considering the scission mechanism implemented on EStokTP. Some cross-linking reactions results as barrierless but some of them feature a transition state, i.e., a not null energy barrier as reported respectively in Table 1 and Table 2.

Reactions	Bond Energies [kcal/mol]
A1 + A1 → A1A1	126.96
A1 + A2 → A1A2	121.65
A1 + B1 → A1B1	93.51
A1 + B2 → A1B2	87.57
A1 + C → A1C	69.26
A2 + A2 → A2A2	117.27
A2 + B1 → A2B1	87.42
A2 + B2 → A2B2	82.35
A2 + C → A2C	65.93
B1 + B1 → B1B1	61.95
B1 + C → B1C	39.42
B2 + B2 → B2B2	49.12

Table 1: Recombination Energies for Barrierless Reactions computed with M06-2X/6-311+G(d,p).

Reactions	Bond Energies [kcal/mol]	Energy Barriers [kcal/mol]
B1 + B2 → B1B2	30.78	0.76
B2 + C → B2C	32.97	0.24
C + C → CC	16.89	3.94

Table 2: Energy Barrier computed with M06-2X/311+G(d,p).

In Table 1, barrierless reactions have been identified mainly by those involving σ-radicals, i.e., A1 and A2, which are the most reactive radicals leading to higher BDE. Localized radicals, known as rim-linked hydrocarbons, are less reactive concerning this reaction class but still more reactive than delocalized species as shown by their cross-linking energies which are higher. In general, the formation of a cross-linking between two aromatics leads to a small drop in the band gap, leading to conjugation effect which give stabilization to the product. In Table 2 reactions with a barrier are reported, i.e., B1B2, CC and B2C cross-linking. Recombination reactions which present an energy barrier involve some of the previously mentioned monomers, which are the most abundant in flame environment because of their stabilization by resonance (e.g. B1 and B2). Also monomer C which is characterized by a more delocalized electron density has been considered. These considered reactions lead to reasonably high energy barriers. This would suggest that bonds between five-membered rings are likely less favorable, unless there is sufficient radical character among the reacting PAHs. Counter wise, when the barrier is low, the bonds formed are easier to be formed but weaker.

After these preliminary calculations rate constants computation have been performed. It is possible to highlight different rate constant profiles with temperature dealing with barrierless reactions or with reactions with barrier as reported in Figure 2. In this second case, reactions are slower and the rate constants smaller, ultimately being less favored. Counter wise, barrierless reactions are generally faster involving much more reactive radicals.

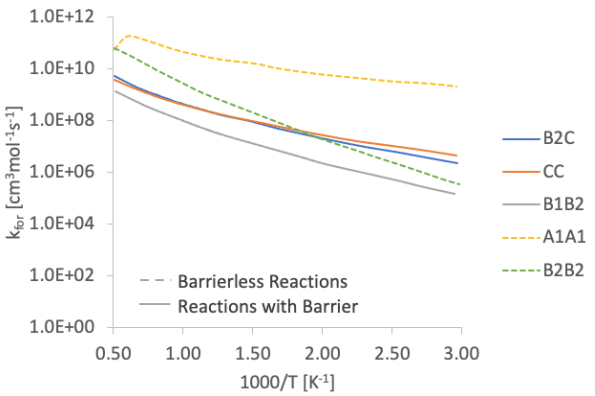

Figure 2: Rate Constants Temperature-dependent profiles.

In Figure 2 the entire set of reactions with barrier is reported despite of just some barrierless recombination reactions which have been selected according to the radicals involved being A1A1 and B2B2 respectively the upper and the lowered limit. This is due to the different reactivity of the radical A1 and to the stabilization by resonance of B2, as mentioned above.
The following step in this work is the rate rule development. As the computational costs of this kind of investigations is to some extent prohibitive, rate rules allow generalization of the findings to similar system, without the need of performing any further theoretical investigation. The prediction of the reactivity of complex molecules such as larger PAHs is obtained starting from the rate constants of smaller structures computed above as a reference. The goal is to understand the reactivity of a specific reaction classes involving PAHs and to develop a rate rule-based model able to describe the kinetic of PAHs with analogous radical behavior but increasing the C-atoms number. Rate rules definition is a powerful tool to describe PAHs reactivity, being a wide class of reactions involving thousands of different isomers. For each class of larger PAHs, such as A1-type, B2-type and C-type, dimerization energies have been compared with the correspondent smaller PAH as reported in Table 3.

Reactions	Bond Energies [kcal/mol]
σ-radicals	
$2C_{12}H_7 \rightarrow C_{24}H_{14}$	126.96
$2\ C_{16}H_9 \rightarrow C_{32}H_{18}$	127.92
$2\ C_{20}H_{11} \rightarrow C_{40}H_{22}$	127.86
localized π-radical	
$2\ C_9H_7 \rightarrow C_{18}H_{14}$	49.12
$2\ C_{13}H_9 \rightarrow C_{26}H_{18}$	50.61
$2\ C_{17}H_{11} \rightarrow C_{34}H_{22}$	49.48
delocalized π-radical	
$2\ C_{13}H_8 \rightarrow C_{26}H_{16}$	16.89
$2\ C_{17}H_{11} \rightarrow C_{34}H_{22}$	8.87

Table 3: Bond Recombination Energy for larger PAH structures computed with M06-2X/311+G(d,p).

Rate rules for the PAH family has been determined with a scaling approach based on the assumption that the reactivity of the system remains substantially unchanged even if the radical structure becomes larger following aromatic rings addition. To formulate rate rules for a whole reaction class it is a necessary condition that the network does not change with the system size. For the specific systems under investigation, dominated by recombination reactions mainly behaving as barrierless it is important that no additional channels become active as reactants get larger. The same behavior needs to be exploited by reactions with barrier [16]. In Table 4 rate rules results are provided and divided according to the class of radicals involved, such as σ-radical, localized π-radical and delocalized π-radical. Being the BDE of larger PAHs consistent with those of the reference reactions a unitary scaling factor has been considered for the kinetic parameters' derivation.
The kinetic parameters reported below have been derived according to the modified Arrhenius expression, $k=A*T^n*\exp(-E_a/RT)$, for reactions with barrier, and as the sum of two modified Arrhenius expressions for barrierless reactions.

Reference reactions	A1	n1	Ea1	A2	n2	Ea2
σ-radicals $2\ C_{12}H_7 \rightarrow C_{24}H_{14}$	23.3	2.83	-0.24	6.26E+04	2.65	26.26
localized π-radical $2\ C_9H_7 \rightarrow C_{18}H_{14}$	146	2.62	5.95	2.42E+36	-5.54	76.25
delocalized π-radical $2\ C_{13}H_8 \rightarrow C_{26}H_{16}$	2.02	2.64	5.6	-	-	-

Table 4: Rate rules adopted in PAH molecules. Units are mol, cm3, kcal, s.

4. Model Validation

Starting from PAH recombination reactions previously discussed, an attempt to validate the CRECK kinetic model has been considered necessary. PAH-rich flames have been simulated substituting the parameters computed in this work with the rate parameters determined according to the rate rules in the CRECK model. The main difference is how barrierless reactions have been considered. In the original CRECK kinetic

mechanism no temperature dependance is accounted for when dealing with barrierless reactions, while in this study those rate constants have been computed as the sum of two modified Arrhenius equations carrying some non-negligible temperature dependance. Some simplifying assumptions have been done to lump the whole set of species provided in the model in reactions classes as those analyzed in this work. Generally, a good qualitative agreement has been observed between the modeled and experimental results, for both gaseous species and soot. However, in this case study the comparison between soot formation rates in these two different scenarios report an overestimation of the rate constants in the original CRECK kinetic mechanism leading to the same corresponding behavior in the soot nucleation rate. By implementing the PAH radical recombination rates computed in this work, the soot model prediction capability has been improved, as shown in Figure 3, where measured soot volume fraction from different jet-fuel counterflow flames has been compared with the original and the updated CRECK soot model.

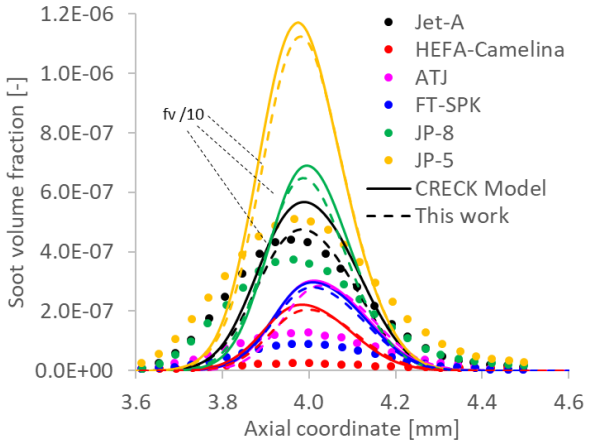

Figure 3: Comparison of measured and simulated soot volume fraction in different jet-fuel flames.

Generally, both models overpredicts the measured soot volume fraction in all the jet-fuel flames considered, with a much larger overestimation in flames characterized by aromatic-rich fuels (Jet-A, JP-8 and JP-5). However, by implementing in the updated model the much lower recombination rate constants calculated in this work, soot yield overestimation decreases thus approaching the experimental values. Specifically, a consistent larger reduction in the predicted soot yield is observed in aromatic-rich fuel flames (Jet-A, JP-8 and JP-5), where PAH radical recombination has a much more significant contribution to soot inception compared to aromatic-poor jet-fuel flames (ATJ, HEFA-Camelina and JP-5).

This result highlights the larger accuracy of the recombination rates computed in this work. However, additional kinetic analyses have shown that, to further improve soot yield prediction, it is necessary to also investigate the rate constant of other mechanisms governing soot inception that are implemented, or some that might be missing in the soot model at present.

5. Conclusions and Future Perspective

Following a preliminary PAHs reactivity analysis, recombination reactions have been considered to develop rate rules which highlight the independence of the kinetic parameters on structures dimensions. As this article has showed, the rate constants computed herein allow to reach improvements in soot formation modeling, improving the model predictive capability for soot formation at flame conditions in different experimental targets. A further investigation is necessary to better understand the soot formation mechanism and to match different experimental setups in a wider range of operative conditions. In particular, a deeper comprehension of the recombination pattern can give an important contribution to the improvement of the detailed soot kinetic model playing a key role in the transition from gas phase to the solid phase. The present findings also carry important implications for flame synthesis of carbon materials, for hydrogen and value-added carbon solids production from methane and hydrocarbons cracking.

6. Bibliography

[1] Agency for Toxic Substances and Disease Registry (ATSDR), "Public Health Statement: Polycyclic Aromatic Hydrocarbons (PAHs)," *Atsdr.Cdc.Gov*, p. 6, 1995, [Online]. Available: http://www.atsdr.cdc.gov/toxprofiles/tp16-a.pdf.

[2] W. Yuan, Y. Li, and F. Qi, "Challenges and perspectives of combustion chemistry research," *Sci. China Chem.*, vol. 60, no. 11,

pp. 1391–1401, 2017, doi: 10.1007/s11426-017-9066-9.

[3] M. Frenklach and A. M. Mebel, "On the mechanism of soot nucleation," *Phys. Chem. Chem. Phys.*, vol. 22, no. 9, pp. 5314–5331, 2020, doi: 10.1039/D0CP00116C.

[4] M. Commodo, G. De Falco, A. Bruno, C. Borriello, P. Minutolo, and A. D'Anna, "Physicochemical evolution of nascent soot particles in a laminar premixed flame: from nucleation to early growth," *Combust. Flame*, vol. 162, no. 10, pp. 3854–3863, Oct. 2015, doi: 10.1016/j.combustflame.2015.07.022.

[5] C. Cavallotti, M. Pelucchi, Y. Georgievskii, and S. J. Klippenstein, "EStokTP: Electronic Structure to Temperature- and Pressure-Dependent Rate Constants-A Code for Automatically Predicting the Thermal Kinetics of Reactions," *J. Chem. Theory Comput.*, vol. 15, no. 2, pp. 1122–1145, 2019, doi: 10.1021/acs.jctc.8b00701.

[6] C. Cavallotti, M. Pelucchi, and S. J. Klippenstein, "EStokTP From Electronic Structure to Temperature and Pressure Dependent Rate Constants," pp. 1–42, 2017.

[7] M. Walker, A. J. A. Harvey, A. Sen, and C. E. H. Dessent, "Performance of M06, M06-2X, and M06-HF Density Functionals for Conformationally Flexible Anionic Clusters: M06 Functionals Perform Better than B3LYP for a Model System with Dispersion and Ionic Hydrogen-Bonding Interactions," *J. Phys. Chem. A*, vol. 117, no. 47, pp. 12590–12600, Nov. 2013, doi: 10.1021/jp408166m.

[8] Y. Georgievskii, J. A. Miller, M. P. Burke, and S. J. Klippenstein, "Reformulation and Solution of the Master Equation for Multiple-Well Chemical Reactions," *J. Phys. Chem. A*, vol. 117, no. 46, pp. 12146–12154, Nov. 2013, doi: 10.1021/jp4060704.

[9] H. Nakata, D. G. Fedorov, S. Yokojima, K. Kitaura, M. Sakurai, and S. Nakamura, "Unrestricted density functional theory based on the fragment molecular orbital method for the ground and excited state calculations of large systems," *J. Chem. Phys.*, vol. 140, no. 14, p. 144101, Apr. 2014, doi: 10.1063/1.4870261.

[10] E. Ruiz, J. Cano, S. Alvarez, and P. Alemany, "Broken symmetry approach to calculation of exchange coupling constants for homobinuclear and heterobinuclear transition metal complexes," *J. Comput. Chem.*, vol. 20, no. 13, pp. 1391–1400, 1999, doi: 10.1002/(SICI)1096-987X(199910)20:13<1391::AID-JCC6>3.0.CO;2-J.

[11] A. Cuoci, A. Frassoldati, T. Faravelli, and E. Ranzi, "OpenSMOKE++: An object-oriented framework for the numerical modeling of reactive systems with detailed kinetic mechanisms," *Comput. Phys. Commun.*, 2015, doi: 10.1016/j.cpc.2015.02.014.

[12] H. B. Zhang, X. You, H. Wang, and C. K. Law, "Dimerization of polycyclic aromatic hydrocarbons in soot nucleation," *J. Phys. Chem. A*, vol. 118, no. 8, pp. 1287–1292, 2014, doi: 10.1021/jp411806q.

[13] J. W. Martin *et al.*, "Reactivity of Polycyclic Aromatic Hydrocarbon Soot Precursors: Implications of Localized Radicals on Rim-Based Pentagonal Rings," *J. Phys. Chem. C*, vol. 123, no. 43, pp. 26673–26682, 2019, doi: 10.1021/acs.jpcc.9b07558.

[14] A. Menon *et al.*, "Reactive localized π-radicals on rim-based pentagonal rings: Properties and concentration in flames," *Proc. Combust. Inst.*, vol. 38, no. 1, pp. 565–573, 2021, doi: 10.1016/j.proci.2020.07.042.

[15] A. Menon, J. W. Martin, J. Akroyd, and M. Kraft, "Reactivity of Polycyclic Aromatic Hydrocarbon Soot Precursors: Kinetics and Equilibria," *J. Phys. Chem. A*, vol. 124, no. 48, pp. 10040–10052, 2020, doi: 10.1021/acs.jpca.0c07811.

[16] E. Ranzi, M. Dente, T. Faravelli, and G. Pennati, "Prediction of Kinetic Parameters for Hydrogen Abstraction Reactions," *Combust. Sci. Technol.*, vol. 95, no. 1–6, pp. 1–50, 1993, doi: 10.1080/00102209408935325.

POLITECNICO
MILANO 1863

SCUOLA DI INGEGNERIA INDUSTRIALE E DELL'INFORMAZIONE

Corso di Laurea Magistrale in Chemical Engineering - Ingegneria Chimica

Rate-rule development for recombination reactions of large Polycyclic Aromatic Hydrocarbon (PAH) based on ab-initio quantum chemistry calculations

Relatore: Prof. Matteo Pelucchi

Correlatore: Ing. Andrea Nobili, Ph.D

Tesi di Laurea Magistrale in Ingegneria Chimica di:

VERONICA VARINI

Matricola 941021

A.A. 2020-2021

To my family

Contents

List of Figures

List of Tables

Abstract

Soot is one of the main products of combustion processes leading to not negligible environmental and health issues. Airborne soot particles absorb solar energy and act as condensation nuclei for cloud droplets, leading also to lung cancer and respiratory diseases. Many research works have been carried out to better clarify the process by which soot forms even if soot formation mechanism is still not well understood because of the complexity of soot particles morphology and of the high reactivity of radicals which contribute to the proposed pathways. Complex hydrocarbon fuel molecules break down and react to form gaseous molecules that are the precursors of soot. Polycyclic Aromatic Hydrocarbons (PAHs) are known to play an important role in the kinetic mechanism and many reactions have been already studied starting from gas phase emissions. The transition from the gas phase to the solid phase is currently object of investigation to better understand soot evolution in combustion processes. Starting from gas phase hydrocarbons the first aromatic ring formation occurs and large PAHs are formed. PAHs grow into layered structure that resemble graphite. Soot nucleation is one of the main objects of study driving PAHs from physical to chemical dimerization. Once formed, soot nuclei continue to grow via surface chemical reactions, PAH condensation and particle agglomeration. The reactions that turn gaseous fuel molecules into that layered structure are difficult to measure and extremely rapid, current models cannot account for the speed at which the reactions occur. In this thesis PAHs reactivity has been investigated dealing with smaller structures, which have been assumed as reference for calculations, and with larger ones reached by dimerization reactions. The considered monomers have been studied as divided in classes according to their reactive edges, following a previous H-abstraction. The goal of this work is a rate rule development to accurately describe the reactivity of this class of reactions considering progressively enlarged monomers dimensions. Preliminary ab-initio quantum chemistry calculations have been performed concerning molecular geometry optimization and electronic energy computation. Gaussian09 allows to investigate the accuracy of DFT methods for bond dissociation energy and rate constants estimation with the aim to overcome computational issues correlated to the complexity of the considered molecules. Rate constants have been implemented in the soot CRECK kinetic mechanism as a validation trial. Flames simulations with different aromatic content have been performed with the OpenSMOKE++ suite. PAHs recombination rates reported in the model provide results which show an overestimation of the experimental values dealing with soot formation rates when PAHs are dominant in flame environment. The model cannot satisfactorily reproduce the measurements even if assuming the updated rate constant parameters computed in this work a more accurate representation of experimental values is reached. However, further theoretical, and experimental investigations on the still poorly understood nucleation pattern are required for an effective assessment of the kinetics involved in the PAHs recombination process leading to the transition from gas phase to solid phase.

Riassunto

Il soot è uno dei prodotti principali dei processi di combustione responsabile di problemi sia ambientali che sanitari non trascurabili. Le particelle di soot nell'aria assorbono l'energia solare e agiscono come nuclei di condensazione, inoltre rappresentano una delle principali cause connesse alla comparsa di cancro ai polmoni e di malattie respiratorie. Molte ricerche sono state condotte per comprendere meglio il processo attraverso il quale si forma il soot anche se il meccanismo di formazione non è ancora stato delineato nel dettaglio a causa della complessità della morfologia delle particelle e dell'elevata reattività dei radicali che vi contribuiscono. Gli Idrocarburi Policiclici Aromatici (IPA) sono molecole in fase gas identificabili come precursori del soot e sono noti per svolgere un ruolo importante nel meccanismo cinetico che li vede coinvolti in molteplici reazioni. Il passaggio dalla fase gassosa alla fase solida è attualmente oggetto di indagine per comprendere meglio l'evoluzione del soot nei processi di combustione. A partire dagli idrocarburi emessi in fase gas avviene la formazione del primo anello aromatico che porta progressivamente a strutture aromatiche più gradi. La successiva nucleazione è uno dei principali oggetti di studio e, una volta formati, i nuclei di soot continuano a crescere attraverso reazioni chimiche superficiali, condensazione di IPA e agglomerazione di particelle. Le reazioni che trasformano le molecole di combustibile gassoso in strutture stratificate sono difficili da misurare ed estremamente rapide, i modelli attuali non possono tenere conto della velocità con cui tali reazioni si verificano. In questo lavoro di tesi la reattività delle strutture aromatiche è stata studiata a partire dalla trattazione di strutture più piccole, assunte come riferimento nei calcoli, sino a quelle più grandi ottenute da reazioni di ricombinazione radicalica. I monomeri considerati possono essere suddivisi in classi sulla base della diversa reattività esplicata, a seguito di una preventiva estrazione di idrogeno. L'obiettivo di questo lavoro è lo sviluppo di rate rules per descrivere accuratamente il comportamento di questa classe di reazioni. Sono stati eseguiti calcoli preliminari ab-initio che prevedono l'impiego della chimica quantistica per l'ottimizzazione della geometria delle molecole e il calcolo delle energie. Gaussian09 ha permesso di analizzare l'accuratezza dei metodi DFT per la stima dell'energia di dissociazione del legame e delle costanti cinetiche con l'obiettivo di evadere i problemi computazionali correlati alla complessità delle molecole considerate. Le costanti cinetiche sono state successivamente implementate nel meccanismo cinetico soot CRECK come tentativo di convalida per fiamme a diverso contenuto di aromatici simulate con OpenSMOKE++. Le velocità di ricombinazione degli IPA riportate nel modello si sono dimostrate essere una sovrastima rispetto ai valori sperimentali in riferimento alla velocità di formazione del soot nelle fiamme in cui questi risultano essere dominanti. Il modello non è pertanto in grado di riprodurre in modo soddisfacente le misurazioni anche se assumendo le costanti cinetiche aggiornate la rappresentazione dei dati sperimentali risulta più accurata. Tuttavia, ulteriori indagini teoriche e sperimentali sono necessarie al fine di una valutazione consistente della cinetica coinvolta nel processo di crescita per ricombinazione degli IPA, ad oggi ancor poco compreso.

Chapter 1 – Introduction

The formation of solid carbon nanoparticles from reacting gases is of interest to a wide range of scientific, technological, and societal problems, including air quality, global climate, human health, and material synthesis. The generation by combustion processes of airborne species of current environment and health concern such as Polycyclic Aromatic Hydrocarbons (PAHs) and soot particles necessitates a detailed understanding of chemical reaction pathways responsible for their formation. The present chapter discusses a general overview of the worldwide energy consumption, of energy sources and of main atmospheric pollutants leading to health and environmental issues.

1.1 Worldwide Consumption Overview

The continuous increase of world energy demand is nowadays one of the main focuses from an environmental point of view especially in those countries where the phenomenon of fast-growing economies is present. Energy consumption per capita of a country is regarded as an important indicator of economy development and according to 2019's data [1] China, U.S., India and Russia are the leading countries worldwide. The reasons for the increase of energy requirement are the economic development, the growing population, and the growing needs of many people and goods around the globe.

BP Chemicals 2019's Statistical Review [1] show primary energy consumption grew by 1.3%, oil remained on top with 40% of the global requirement and natural gas contributed the second largest increments with 36% as shown in Figure 1.1. Cumulatively, fossil fuels still supply 79% of world's energy consumption including natural gas, petroleum, and coal even if renewables coverage is progressively increasing.

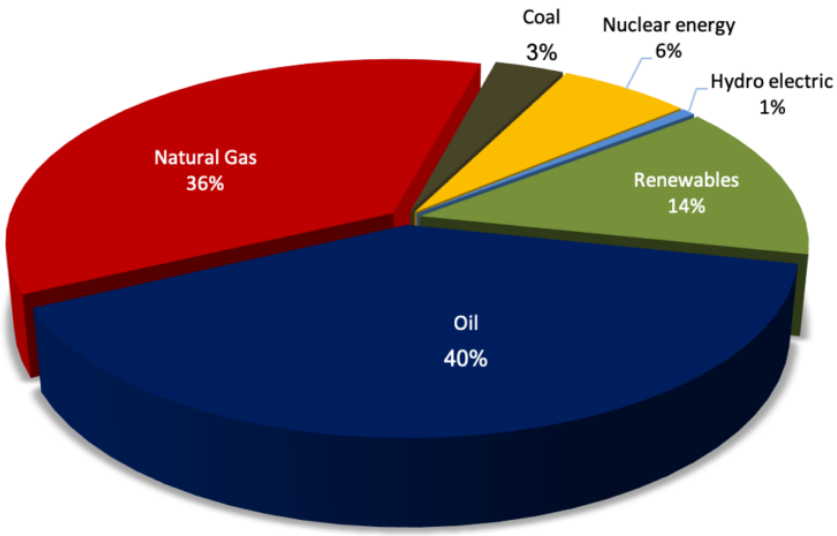

Figure 1.1: 2019's Primary Energy Consumption [1].

Global energy demand is estimated to have fallen by 4.5% in 2020 due to Covid-19 pandemic [2]. This is the largest recession since the end of World War II, driven by an unprecedented collapse in oil demand, as the imposition of lockdowns around the world decimated transport-related request. The drop in oil consumption accounted for around three-quarters of the total decline in energy demand. Natural gas showed greater resilience, helped primarily by strong growth in China. According to Figure 1.2 despite of 2020's collapse oil is still the dominant fuel in Africa, Europe and the Americas followed by natural gas and coal in the Asia Pacific Region.

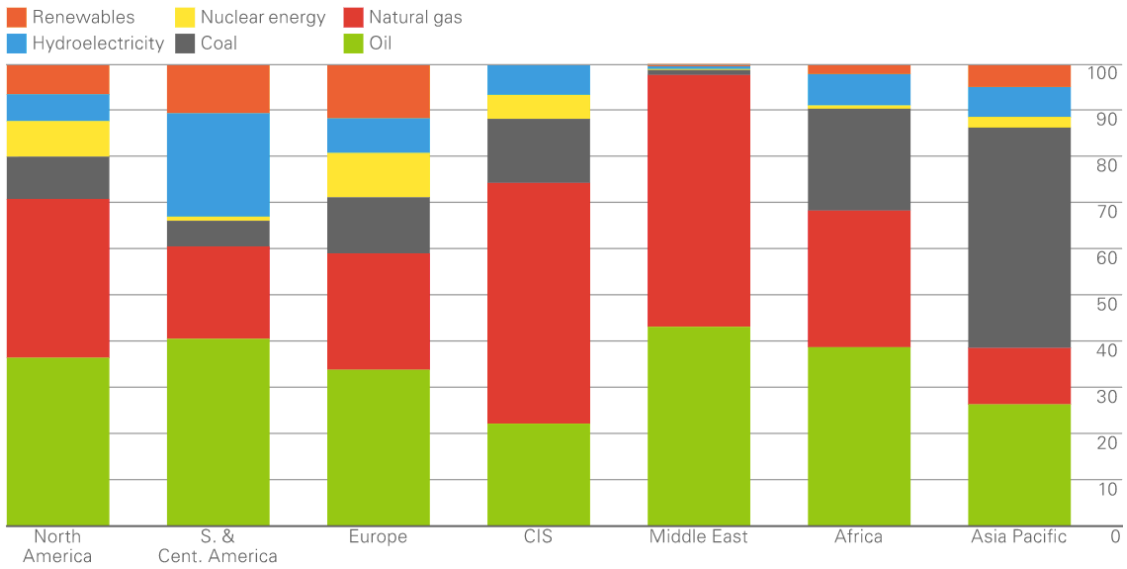

Figure 1.2: Regional Consumption Pattern [1].

As the main related consequence to fossil fuels consumption also the fall in carbon emissions from energy use was equally notable, with emission falling over 6% in 2020 – again, the largest decline since 1945. From an historical perspective, the falls in energy demand are obviously dramatic but from a forward-looking perspective, the rate of decline in carbon emission observed in 2020 is what the world would need to reach every year for the next 30 years to be on track to meet climate goals.

1.2 Air Pollution from Combustion

Fossil fuels combustion for electricity generation and transport are the largest emitters of greenhouse gasses, such as H_2O, CO_2, N_2O and CH_4 that are vented to the atmosphere. However, emission growth in 2019 was only 0.5% and in 2020 it reached a reduction of ~6%, as mentioned above, which was less than half the 10-years average. As a result of the 50 billion tons emitted a year climate change is linked to greenhouse effect and at current emission rate earth temperature will increase by 1.5 °C before 2030.

Air pollutants can be classified into two different categories which are primary and secondary air pollutants. The first concerns direct emissions in the atmosphere such as CO, CO_2, volatile organic compounds (VOCs),

and soot together with nitrogen monoxide (NO) generated during combustion processes at high temperature. Secondary air pollutants are formed through chemical or physical transformation processes in the air, and they include ozone, which is formed from the reaction between hydrocarbons and nitrogen oxide in the presence of air, and NO_2, formed when NO is oxidized by atmospheric oxygen. From fossil fuels combustion a huge amount of sulfur oxides (SO_x) and hydrogen sulfides (H_2S) is also produced [3].
Gaseous emissions are just a percentage of the total emissions, indeed solid sources of pollutants are generated from Polycyclic Aromatic Hydrocarbons (PAHs) and Particulate Matter (PM) that play a central role as primary emissions from combustion devices as engines and furnaces. Incomplete combustion occurs when the oxygen supply is below stoichiometry and leads to the release of carbon in the form of carbon monoxide, carbon particles and unburned hydrocarbons. PAHs are a result of incomplete fuel combustion, and they are soot precursors. Non-ideal burning conditions are generally present in practical cases due to local cold spots, inadequate fuel and oxidizer mixing, too short residence time at high temperature, sudden cooling of the flame gases through combustion chamber walls, insufficient pulverizing of solid fuels or atomizing of liquid fuels can all cause soot formation. Beside the unavoidable loss in efficiency, i.e., heat of combustion not fully exploited, such conditions promote the formation of particulate matter.

Air contains aerosols, i.e., mixtures of gaseous and particulate matter (PM) pollutants released from natural and anthropogenic sources. An aerosol is a dynamic system where different compounds can be in gas, liquid, or solid phase depending on their thermodynamic equilibrium. Ambient PM is a complex mixture of inorganic elements, water soluble ions (acids, alkalines and salts) forming secondary inorganic aerosols, carbonaceous aerosols including organic carbon (OC) and elemental carbon (EC), organic compounds such as PAHs, VOCs, secondary organic aerosols (SOAs), and inhalable biological matter, including bacteria, fungi and pollen [4].
Aerosol can also behave as viruses' carrier, such as for Covid-19. Airborne transmission is different from droplet transmission as it refers to the presence microbes within droplet nuclei, which are generally considered to be particles <5 μm in diameter, and which result from the evaporation of larger droplets or exist within dust particles remaining in the air for long periods of time [5].

PM can be distinguished in different classes depending on the carbonaceous particles dimensions as shown in Figure 1.3. Different sources lead to different ranges of dimensions. The smallest particles, i.e. $PM_{0.1}$, include mainly manufactured nanoparticles and diesel exhaust. $PM_{2.5}$ can be also constituted by sea salt nuclei, tobacco smoke and metal fumes, while PM_{10} includes coal dust and coal fly ash, too. Depending on the dimension PM can be classified as respirable particles with a diameter smaller than 2.5 μm which are the most damaging for human health because of deep penetration into the cardiovascular and respiratory system, and inhalable particles since they can be breathed mouth and nose [6].

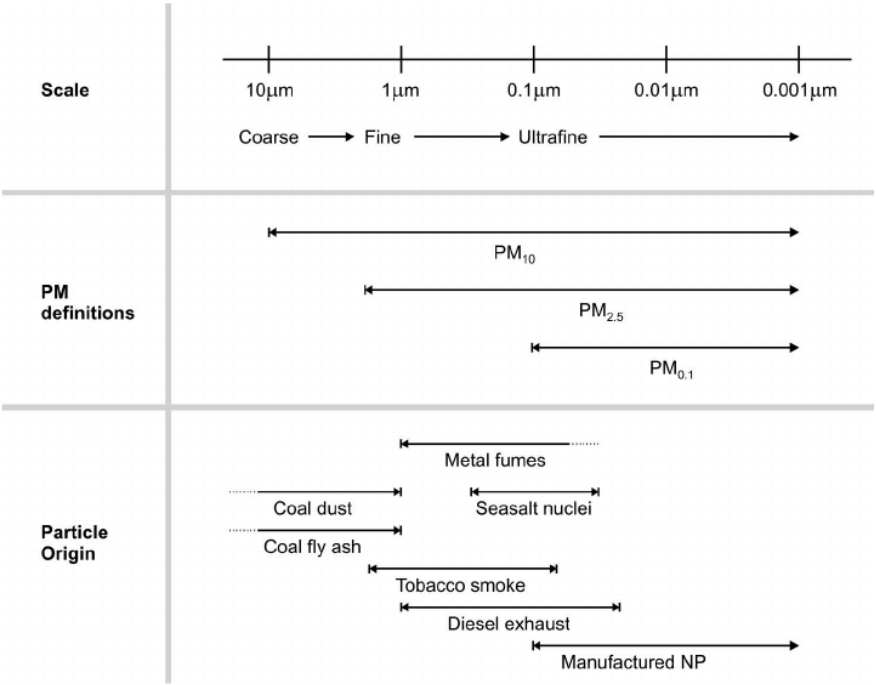

Figure 1.3: Classification of Particulate Matter (PM) and Source of Particles [7].

In urban areas, most PM emissions originate from local anthropogenic sources, such as traffic, industry, domestic fuel burning, and other combustion-related emissions, along with long-range transport of $PM_{2.5}$. As shown in Figure 1.4 different regions of the Earth are characterized by different pollution source and dimension distribution. In Africa and Central Europe $PM_{2.5}$ emissions are dominated by domestic fuel burning, while in South America, Southwestern Europe, and Asia, except for China, traffic is the main source of $PM_{2.5}$. Globally, 25 % of urban ambient air pollution by $PM_{2.5}$ comes from transportation, while 15% of $PM_{2.5}$ is contributed by industrial activities. Even though PM is a complex mixture of primary and secondary particles and condensates, epidemiological studies often focus on health effects of $PM_{2.5}$ or PM_{10} mass concentrations, regardless of their chemical composition, biological activity, or particles morphologies [8].

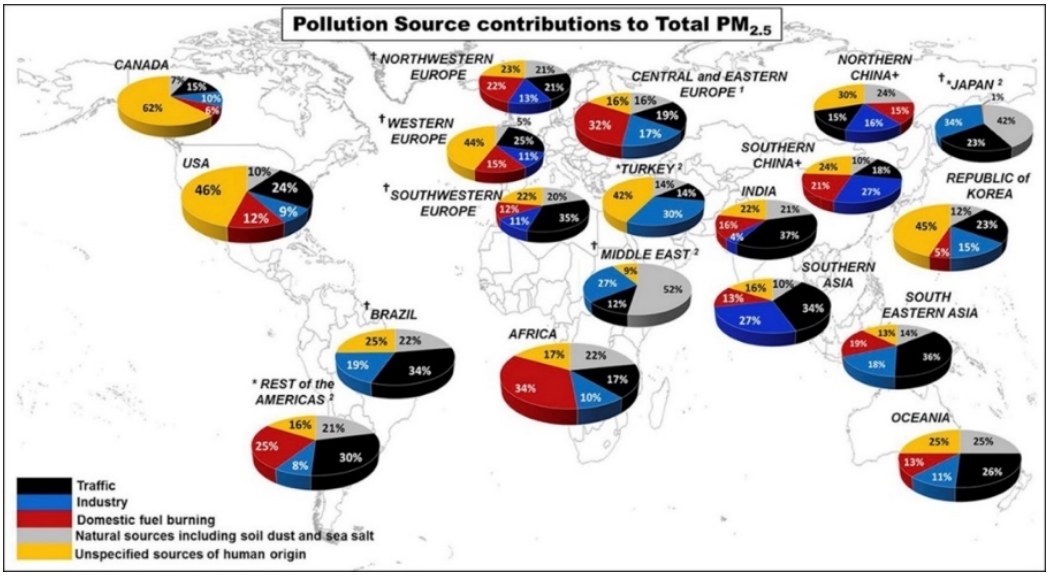

Figure 1.4: Relative Source Contribution to $PM_{2.5}$ in Different Urban Sites [9].

Figure 1.5 shows the global emission of PAHs listed by the U.S. Environmental Protection Agency (EPA) as a risk for human health and environment. Among the total PAHs emission, roughly 6% of the emissions were in the form of high molecular weight carcinogenic compounds.

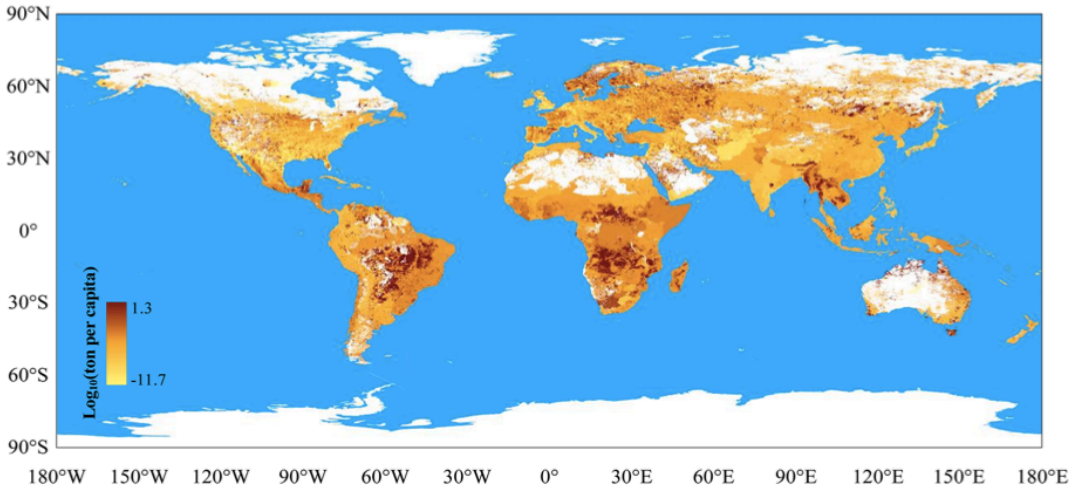

Figure 1.5: PAH emissions [10].

1.3 Soot Effects on Environment and Human Health

Nanoparticles are of interest not just from an environmental point of view driving to global warming and darkening of polar icecaps, but also concerning human health problems such as respiratory and cardiac diseases caused by their inhalation. Due to their negative impacts on environment and human health, future regulations on soot emissions are expected to become stricter, in particular by controlling the size of the emitted particles [11]. PM_{10} can be breathed into the nose or mouth, while particles smaller than 2.5 µm ($PM_{2.5}$) can reach the terminal bronchioles into the lungs and causing extremely serious health diseases [8]. In epidemiological studies air pollution was positively associated with death from lung cancer and cardiopulmonary disease. As previously mentioned, fine particles, defined by a diameter equal to or below 2.5 µm, are thought to pose a particularly great risk to health because they are more likely to be toxic than larger particles and can be breathed more deeply into the lungs but also, they can easily gain access to the blood stream and be transported towards organ and tissues, causing cardiovascular diseases and inflammations [12]. According to the European Environmental Agency (EEA), ambient air $PM_{2.5}$ concentrations alone caused *ca*. 400,000 premature deaths in the last decades [13].

Emitted particulate matter is not just correlated to human health diseases but past research has shown that the dominant influence on recent global climate changes comes from greenhouse gas increases with implications for future temperature growth since Earth globally absorbs sunlight rather than reflecting. The need to control the emission of combustion products of environmental and health concern while also promoting more efficient utilization of fossil energy resources requires the development of cleaner and more

economic combustion equipment which in turn requires a better physical and chemical understanding of combustion processes.

One mitigation proposal for environmental issues due to particulate matter and so soot is to reduce black carbon aerosol emissions taking into account of particles dimensions that are a key characteristic for the estimation of the correlated risks to obtain a better understanding of their fate and human exposure. It is important to regulate not only the total mass of particles emitted, but also their number and size. In fact, the smallest particles have a negligible contribution to the total mass, but they are much more toxic than the bigger one. Nowadays the debate is still open dealing with the compensation approaches for emission abatement and the paradigm shift regarding carbon-hydrogen reutilization.

1.4 PAHs Contribution

Soot contribution to environmental issues and health problems is known to be important with a strong correlation to particle dimensions. The understanding of the formation mechanism is important, but it is not consolidated, and it is still object of investigation starting from some key precursors such as PAHs. To reach a deep comprehension of soot interactions and growth many studies have been carried out. Particle's morphology and chemical composition have been of interest to study their interactions with the surrounding environment and their reactivity.

PAHs are a large family of organic compounds that are typically composed of two or more fused aromatic rings, and they behave as the building blocks of soot formation. PAHs generally occur as complex mixtures, not as a single compound. They are found throughout the environment in the air, water, and soil. They are in the air, either attached to dust particles or as solids [14]. Since PAHs in environmental samples have multiple origins rather than a single one, it is not always simple to predict the major PAH sourced and their relative contributions.

Soot associated PAHs such as naphthalene, acenaphthylene, acenaphthene, and fluorene are influenced by environmental aging conditions. While PAHs are produced from various combustion sources, soot is also generated from volatiles formed within flames that subsequently produce carbon-rich material through a complex mass growth process. Considering higher residence time for pyrolysis in postflame zone the polyaromatic material generates an amorphous phase that while growing it is turning into progressively more graphitic material thanks to the stacking of planar Polycyclic Aromatic Hydrocarbon (PAHs) with an H/C ratio in mature aggregates about 0.1. Higher ratio of carbon in the edge sites versus basal plane sites leads to easier accessibility of carbon and higher reactivity.

It is known that the soot nanostructure greatly influences the reactivity of the soot, e.g., oxidation rates. Soot that incorporates curved graphitic planes shows a higher reactive character because of molecular strain.

Being C atoms easier to access on the edge sites, the amorphous structures is confirmed to be more reactive. Chemical composition as well as size particles play an important role concerning health issues. Accounting for this aspect the transition from gas-phase to particle phase requires a deeper understanding, the so-called soot inception mechanism. The most widely accepted mechanism for modeling soot particle inception is the irreversible dimerization of two PAHs due to π- π interactions. Experiments have shown that the size distribution of soot particles in flames exhibits a bimodal behavior, which may be well reproduced by assuming dimerization as the soot inception step.

However, dimerization reactions give just a small contribution to soot formation driving to larger PAHs formation and to soot nucleation. Radicals involved in the mechanism coming from an H-abstractions on PAHs are very reactive and so in low concentration in the combustion environment making experimental data collection very difficult because of the enounced reactivity of these species. At this point, ab initio quantum chemistry calculations are the main source of information which help to deal with the chemical and physical complexity of these reactive systems.

1.5 Current Challenges in Soot Modeling

The need to control emissions of combustion products of environmental and health concern while also promoting more efficient utilization of fossil fuels energy resources requires the development of cleaner and more economic burning equipment which in turn requires a better physical and chemical understanding of combustion processes. Therefore, the study of their formation and chemical and physical properties is object of intense scientific and technical investigation, aimed to improve the technology of practical combustion and the quality of fuels. Combustion optimization can be achieved through the improvement of engine design or creating new fuel formulations. Some emission control techniques are of interest with the aim to limit correlated risks. In general, the greatest achievement is an efficiency of 99.8% by weight removal from the raw gas input. Most widely used technologies are electrostatic precipitators (EPs), fabric filters, cyclone precipitation, and wet scrubbers. However, efficiency strongly depends on particles composition and dimensions.

Thanks to recent research works some alternatives have been consolidate such as innovative materials for applications in solar cells, biological labeling, sensor, and catalyst [15]. Carbon Particles Nanostructures (CPNs) showed strong mechanical stability and adhesivity. Furthermore, the whole synthesis process resulted cost-effective and easily reproducible, thus proving the scalability to industrial application of CNPs-based materials [16] [17].

Hydrogen is the other attractive components of PAHs, and it can find applications from a variety of sectors as a potentially valuable decarbonizations tools. The majority of hydrogen produced today is used for oil

refining and ammonia production, but proponents argue its applications can be expanded to wider industrial uses, transportations, buildings, and even power generation. Hydrogen can ben produces in several ways, both with fossil fuels and with renewable energy, however, decarbonized hydrogen is currently not cost-competitive with hydrogen derived from fossil fuels. Currently, 95% of global hydrogen is produces through a process of steam methane reforming (SMR) of fossil fuels which needs to be coupled with carbon capture and storage (CCS) to reduce CO_2 emissions, this approach referred to as 'blue' hydrogen. The most widely discussed and proposed alternative approach is to produce hydrogen through electrolysis, this is referred to as 'green' hydrogen. A novel alternative that in many ways sits somewhat between blue and green hydrogen is the 'methane pyrolysis' – turquoise hydrogen. The feedstock used is still methane, but the carbon released is solid, as particulate, rather than CO_2. As a result, there is no requirement for CCS and the carbon can even be used in other applications [18].

Adverse health effects and negative impacts on the earth environment previously mentioned are the most cited reasons for the interest and motivation in developing a fundamental understanding and ability to model the formation of soot and its properties.

1.6 Thesis Organization

This thesis focuses on PAHs reactivity in flame conditions and their contribution as soot precursor. This analysis provides a deep investigation on PAH properties and how they influenced radical-recombination reactions involved in soot growth pathways. Different reactive edges have been investigated and a rate rules study has been developed accounting for progressively larger PAHs structures considering how molecules dimensions impact on the reactive system. The rate constants computation together with model validation trials concerning laminar and premixed flames is a key step to understand the relative contribution of radical species. The ultimate goal, also for future development, is the validation of the CRECK soot kinetic mechanism involving PAHs radicals and molecules to reach an accurate representation of experimental data.

This chapter, Chapter 1, provides a brief overview of pollutants generated by combustion and their negative effects on both human health and environment. PAHs contribution is also mentioned together with some future applications to contribute to the still open debate about soot formation and emissions compensation. Chapter 2 provides the description of the soot formation mechanism starting from incomplete combustion conditions. PAHs state of the art is also reported focusing on dimerization reactions which play a central role dealing with the soot inception step. Chapter 3 provides insight to the governing equations and to the theoretical methods used to derive kinetic parameters focusing on quantum molecular modeling and computational tools adopted to perform ab-initio calculations. Chapter 4 discusses in detail PAHs reactivity together with recombination energy and rate constants computation for some classes of PAH recombination reactions. Rate rule formulation for larger PAH structures has been presented. Chapter 5 reports a model

validation trial for the CRECK soot model. Chapter 6 draws conclusions of the work presented and future research explanation.

Chapter 2 – State of the Art

Combustion processes are major sources of airborne pollutants, including Polycyclic Aromatic Hydrocarbons (PAHs) and soot. Soot formation detailed description requires a complex mechanism. However, there is a very poor understanding of the chemical pathways from light gaseous species to large PAH molecules and soot particles. Soot formation mechanism is described in this chapter, acetylene is the main precursor together with benzene which is the first aromatic ring leafing to enlarging structures, till reaching solid phase. The proposed pathways involve first-aromatic-ring formation, with increasing dimensions leading to larger PAHs structures, inception, surface growth and coagulation. Soot oxidation process is reported too being of relevant importance as it is competitive with soot growth. Finally, a general overview about modeling approaches is presented.

2.1 Soot Formation Mechanism Overview

In the past decades, substantial understanding has been gained on the mechanism of soot formation, showing that evolving from gas-phase, molecules with size of a few angstroms, Polycyclic Aromatic Hydrocarbons (PAHs) are first formed, followed by solid particles inception, growth, and parallel oxidation, finally reaching aggregation into mature soot with the size of a few micrometers as shown in Figure 2.1. The time scale of the entire process is on the order of few milliseconds (10-100 ms) [19].

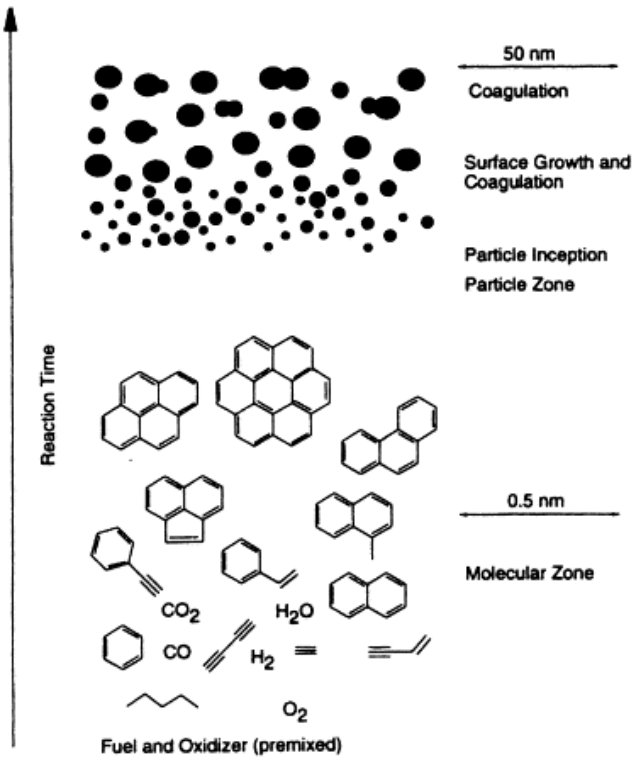

Figure 2.1: Soot Formation Mechanism [20].

PAHs play an important role in soot formation as recognized since the mid of 1980s. The first model developed by Frenklach and co-workers is still considered a pioneer step toward the use of detailed kinetic models to describe PAH and soot formation in combustion [21]. The model was able to predict the correct order of magnitude of the incipient soot particle concentration, but it underestimated the mean soot particle size. In subsequent works it has been highlighted that condensation via physical association of PAHs as small as pyrene was necessary to correctly reproduce the soot particle size distribution, but more recent investigations confuted this previous hypothesis, underling the relevance of chemical contribution. The reactive PAH dimerization is important to reduce soot nucleation reversibility as reported in Figure 2.2. Accounting for PAH chemical bond formation stabilizes dimers and increases the soot concentration, in good agreement with the Laser Induced Incandescence (LII) measurements. The abundance of dimers of small PAHs highlights the dominant role of PAH concentration over their size [22]. Acetylene, benzene, and ethanol flame leads to different pathways and combustion products. Acetylene is the most mentioned precursor, and its analysis requires the coupling of the gas phase kinetic scheme with soot kinetic model [23].

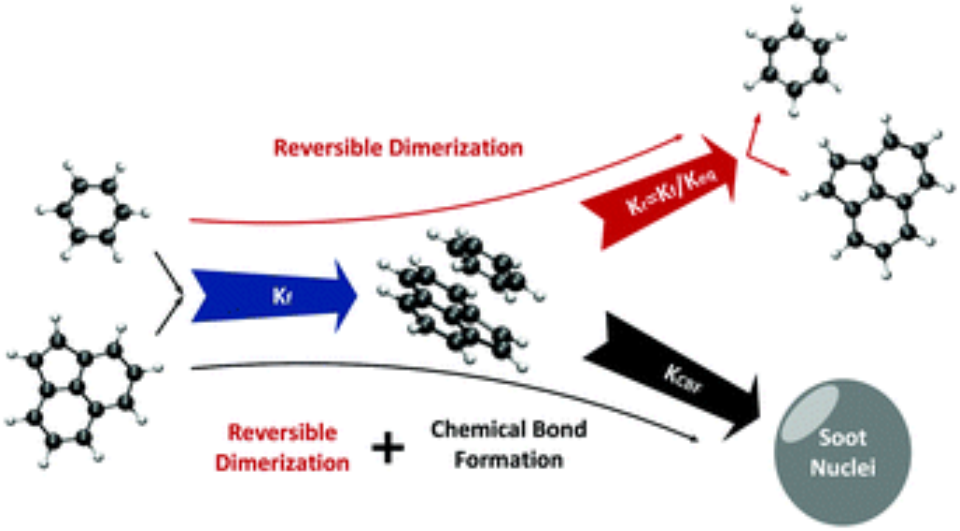

Figure 2.2: PAHs reversible dimerization scheme [22].

Soot Basic Structural Units (BSUs) consist of a stack of several parallel polyaromatic hydrocarbons exhibiting some amount of curvature. The quantity of soot generated, and the nanostructure of the particles largely depend on their formation conditions. High Resolution Transmission Electron Microscopy (HRTEM) studies by Vander Wal et al. showed that the initial fuel composition, e.g., the aromatic and aliphatic fuel content in the fuel mixture, as well as the temperature have a significant effect on the nanostructure of soot particles. Furthermore, under engine conditions, not only fuel and temperature, but also parameters like injection timing, turbulence intensity, exhaust gas recirculation level, and the pressure impact the soot structures [24]. The HRTEM showed that the sizes of particles within nascent soot were fairly constant at the core and edges, and consistent with PAHs containing approximatively 20 carbon atoms or 5-rings. The Laser Micro-probe Mass Spectrometry (LMMS) was used in previous studies to determine the ass of PAHs found within nascent

particles. The masses were found to be consistent with PAHs of approximatively 20 to 21 carbons while PAHs containing 38 as many as 38 carbons were detected in more mature soot particles.

Over the years one of the main focuses has been the transition from gaseous PAHs to “solid” carbonaceous particles referred to as soot nucleation. The formation of soot is a complex process involving gas-phase chemical kinetics, heterogeneous reactions on the particle surface, and particle dynamics. It is commonly assumed that soot inception occurs by collision of Polycyclic Aromatic Hydrocarbon (PAH) molecules driving the growth by addition of mass on the surface through chemical reactions [20] [25]. Nucleation mechanism is just one of the steps involved in soot formation. It is important to examine PAHs growth starting with benzene till two-three-ring level by means of radical addition reactions and cyclization of resonantly stabilized radicals. The generation of free radicals during combustion processes plays an important role in the reaction mechanism. Soot particles formation depends on a wide range of parameters including temperature, pressure, fuel type, and oxygenated additives [26]. The net formation rate of aromatics increases monotonically with C/O ratio, and at a fixed C/O ratio, it passes through a maximum as temperature is increased as shown in Figure 2.3.

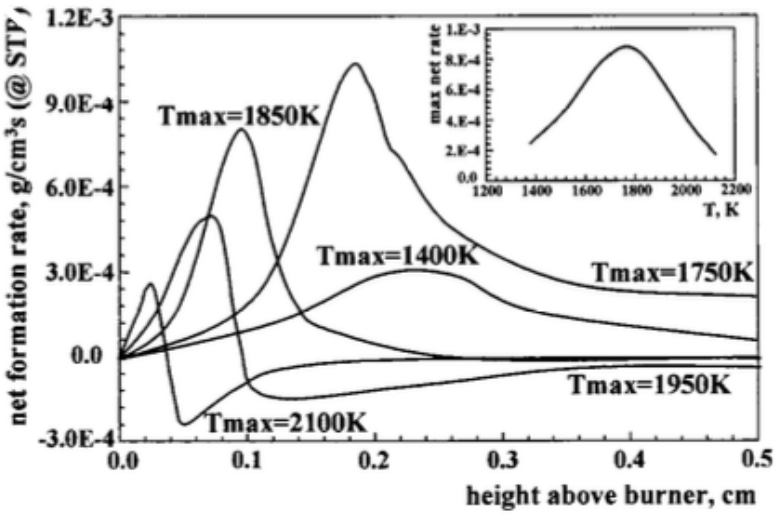

Figure 2.3: Net rate of larger aromatic formation predicted at different flame temperatures and at a fixed C/O ratio of 0.80 [27].

The concentration profile of soot is “bell-shaped” leading to the formulation of the hypothesis that the formation of two- and three-ring structures may be the rate-determining step in soot formation. Also, a lower H/C ratio of the fuel leads to indicate more carbonization in the high temperature environment [27].

2.2 First Aromatic Ring

The development of a comprehensive description of soot formation requires the understanding of the chemistry of molecular growth beyond the first aromatic ring and the identification of key intermediates. Production of larger PAHs and then soot is believed to be controlled by the formation of small aromatic

species, containing from one to few aromatic rings. Acetylene is known to play an important role as a PAHs precursor and soot nucleation following the H-abstraction and C_2H_2-addition (HACA) mechanism which progressively increases the size of PAHs from C2, C3, C4 hydrocarbons with subsequent inception and formation of soot particles [28] [29].

In many studies dealing with the analysis of the starting steps involved in the mechanism methane, ethane, ethylene, acetylene and 1,3-butadiene were used as fuels, alone or in mixtures. Gas chromatographic analysis show that the principal stable products are ethane, ethylene, acetylene, methylacetylene, diacetylene, vinylacetylene, butadiene and benzene concerning fuel pyrolysis zone. The relative amounts of these species vary with the type of considered fuel. Methyl radicals are responsible for the relatively high concentrations of methylacetylene observed in methane flames, but not with other fuels. With diffusion flames containing unsaturated molecules, sharp increase in the concentration of acetylene is observed.

Both acetylene pyrolysis and first aromatic ring formation are considered starting points for PAHs growth and the key step is the acetylene contribution given by HACA leading to benzene [30]. As already mentioned, the first aromatic ring is produced mainly through the recombination of small molecules and radicals. Cole et al. [31] proposed an additional key reaction between acetylene and 1,3-butadiene leading to the cyclization of aromatic and the release of H•. Acetylene addition onto C_4H_5 isomers was also studied through ab-initio calculations performed by Senosiain and Miller [32]. Both n−C_4H_5 and i-C_4H_5 react giving fulvene ($C_5H_4CH_2$), while benzene is generated by only n-C_4H_5 [33].

$$n\text{-}C_4H_5 + C_2H_2 \rightarrow C_5H_4CH_2 + H\bullet$$

$$n\text{-}C_4H_5 + C_2H_2 \rightarrow C_6H_6 + H\bullet$$

$$i\text{-}C_4H_5 + C_2H_2 \rightarrow C_5H_4CH_2 + H\bullet$$

Fulvene from i-C_4H_5 rapidly rearranges to benzene under fuel-rich conditions by reaction with H• radicals [32]:

$$H\bullet + C_5H_4CH_2 \rightarrow H\bullet + C_6H_6$$

Cole and coworkers suggest cyclization from n-C_4H_3 with acetylene contribution [34]:

$$n\text{-}C_4H_3 + C_2H_2 \rightarrow C_5H_4CH$$

$$n\text{-}C_4H_3 + C_2H_2 \rightarrow C_6H_5\bullet$$

$$i\text{-}C_4H_3 + C_2H_2 \rightarrow C_5H_4CH$$

Vinyl radical (C_2H_3) in 1,3-butadiene flame is an important contributor to the radical mechanism:

$$C_2H_3\bullet + C_4H_4\bullet \rightarrow C_6H_5\bullet + H\bullet$$

C_3H_3 radical is resonantly stabilized, and its recombination gives odd-carbon-atom formation. In the study on benzene potential energy surface (PES), Miller and Klippenstein [35] found the following main product channels for aromatic ring formation:

$$C_3H_3\bullet + C_3H_3\bullet \rightarrow C_6H_6$$

$$C_3H_3\bullet + C_3H_3\bullet \rightarrow C_6H_5\bullet + H\bullet$$

$$C_3H_3\bullet + C_3H_3\bullet \rightarrow C_5H_4CH_2$$

$$C_5H_4CH_2 \rightarrow C_6H_6$$

$$C_5H_4CH_2 \rightarrow C_6H_5\bullet + H\bullet$$

Wu et al. [23] studied high temperature condition flames (2000-2500 K) and the radical pathways has been deeply investigated being the favorite one. Experimental analysis on acetylene pyrolysis is carried out in a wide range of conditions, from 900 to 2500 K, not only to highlight the competition between the molecular and the free radical pathways but also to analyze the successive condensation reactions for the formation of PAHs and the growing soot particles.

Frenklach et al. [21] investigating previously mentioned steps highlighted that not just acetylene but also vinylacetylene and diacetylene as molecules and radicals are important intermediates, as shown in Figure 2.4. Chain lengthening of acetylene leads to the formation of unsaturated C4, C6, C8, etc. radical species which can either stabilize as polyacetylenes, or in some cases, either by formation of a branched radical with ring-closure or by cyclization, form an aromatic ring with a 2-carbon sidechain (i.e. C6-C2) [36] [37].

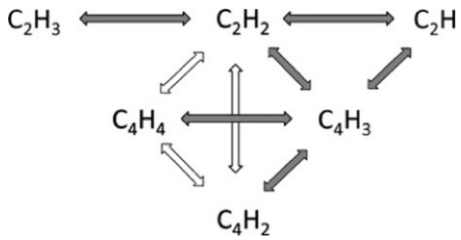

Figure 2.4: Vynylacetylene and diacetylene molecules and radicals' paths [38].

In the presence of oxygen (air), the number of free radicals participating in the reactions is considerably increased. Oxygen molecules react with the initial free radicals generated by heating of the fuels and followed by a multitude of reactions. Free radicals such as $H^{\bullet}$, $OH^{\bullet}$, $OOH^{\bullet}$, and $O{:}$ further interact with the fuel molecules, producing, by propagation, a multitude of other reactions [39] [40].

$$O_2 + C_6H_5\bullet \rightarrow C_6H_5O\bullet + O\bullet$$

$$C_6H_5O\bullet \rightarrow C_5H_5\bullet + CO$$

$$C_6H_5O\bullet + H\bullet \rightarrow C_6H_5OH$$

$$C_6H_5OH \rightarrow C_5H_6 + CO$$

Nowadays correlations between fuel structure and soot formation have been established and accordingly different pathways and contributions have been identified. Sooting tendencies was shown to decrease in the order: naphthalenes > benzenes > diolefins > monoolefins > paraffins.

While ring closure is reached radicals can progressively react increasing their dimensions. On the other hand, those reactive intermediate hydrocarbons may form relatively inactive polycyclic aromatics by intramolecular rearrangements or by splitting off parts in which the aromatic structure is already formed.

2.3 Polycyclic Aromatic Hydrocarbons (PAHs)

Low PAHs concentration and their short lifetime make the study and experimental measurements very complicated forcing to perform measures far from real aperitive conditions, i.e., low pressure. Theoretical tools are used to reach a deep understanding of PAH kinetics [41] [42] [43], through Potential Energy Surface (PES) and rate constant calculations of key-reactions of aromatic chemistry. Theoretical tools allow the development of robust and physically bound kinetic models even at conditions beyond experimental limitations. Polycyclic aromatic compounds are formed in concentration about 100 times larger than aliphatic fuel for the same C/O ratio. Their maximum concentration is reached within the oxidation zone and decrease at the end of it where most of them nucleates as carbonaceous solid particles. Following the first aromatic ring formation (see Figure 2.5), HACA governs molecular growth.

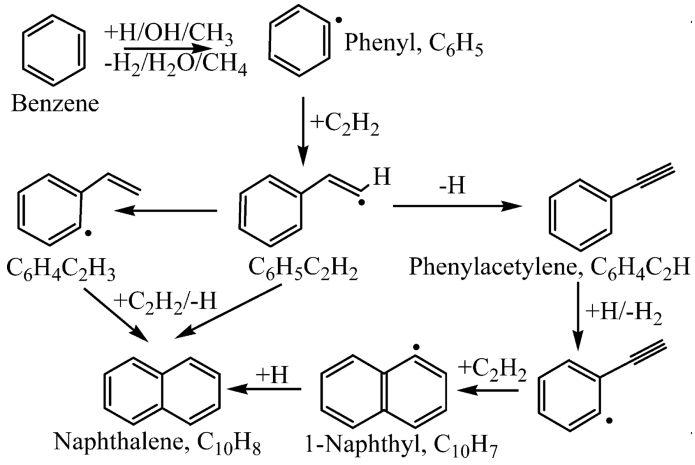

Figure 2.5 - HACA mechanism [44] .

Resonance-Stabilized-Radicals (RSRs) clustering contributes to PAHs and other hydrocarbons to increase their dimensions, recombining at high temperatures. The mechanism is initiated and propagated by RSRs with unpaired electron to allow extended conjugation [25]. Radical-radical and radical-molecule hydrocarbon reactions lead to larger PAHs and regenerates RSRs keeping their concentration high making them to act as clustering nuclei. This mechanism is called Clustering of Hydrocarbons by Radical-Chain Reactions (CHRCR) [45].

Addition of acetylene (C_2H_2) or vinyl (C_2H_3) to an RSR forming a larger radical can also occur. Such radicals are not consumed, but they enlarge the structure surviving long enough to act as clustering seeds for other hydrocarbons. As shown in Figure 2.6 also vinylacetylene plays an important role leading to naphthalene formation ($C_{10}H_8$).

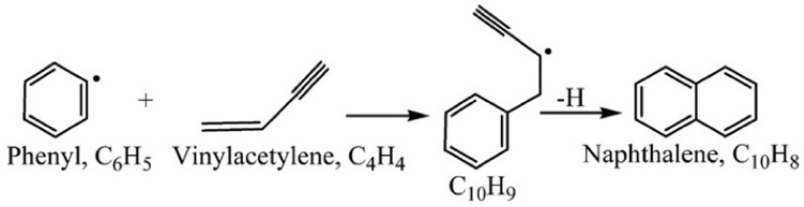

Figure 2.6: Vinylacetylene Addition to Phenyl [44].

Carbon Addition and Hydrogen Migration (CAHM) mechanism proposed by Zang et al. described PAH and soot formation when HACA mechanism in not favored. It consists in the direct acetylene addition on the edge of di-radical or multi-radical PAHs, followed by H atom migration as in Figure 2.7.

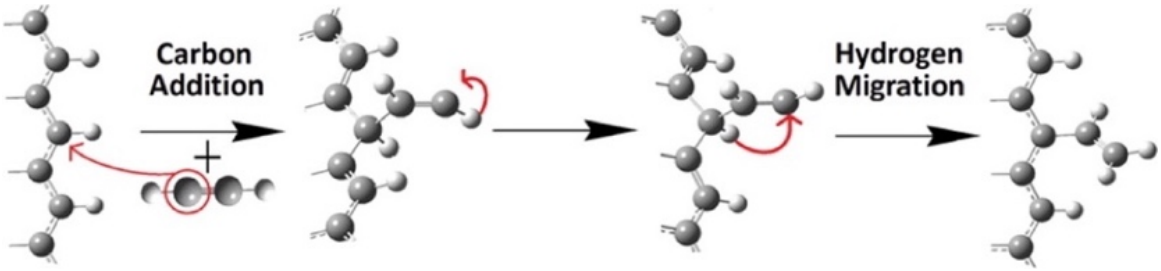

Figure 2.7: Carbon Addition and Hydrogen Migration (CAHM) Mechanism [46].

It is widely accepted that the large PAH formation rate is essentially determined by the process of aromatic growth which is partially controlled by HACA mechanism according to Zhang et al. [46] even if more recently Warumporn et al. [47] consolidated complementary interpretation. HACA step requires that the hydrogen atoms are sufficiently abundant to form active sites.

In Figure 2.8 the relative contributions of HACA mechanism and PAH condensation reactions to the growth of soot is reported at low pressure (dashed lines) and atmospheric pressure (solid lines). The thickness of the arrows represents the importance of different pathways showing acetylene as the most involved species.

The role of C_2H_2 and HACA mechanism in the successive soot growth decreases, because of the preferential addition to most abundant PAH. Mainly in very rich flames at high pressure, benzene and heavy PAHs condensation reactions on soot particles play a relevant role. At lower pressure instead, acetylene addition dominates over PAH condensation, as PAH concentration strongly depends on pressure. It is also believed that soot mass growth is not likely to occur at temperatures below 1500 K in the post flame region because of the correspondingly low concentration of hydrogen atoms [26] [48]. When conditions listed above are present the aromatic core is first formed in the high-temperature region of the premixed flame, followed by the formation of the aliphatic shell over the aromatic core when temperature decreases. Due to delocalized π electrons, generated PAHs have delocalized properties [49].

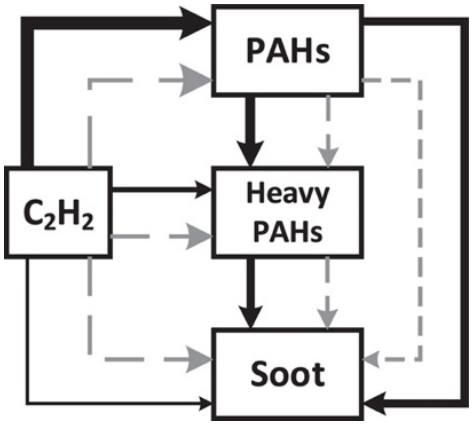

Figure 2.8: C_2H_2 relative contribution to PAHs growth.

PAH growth encounters a thermodynamic barrier at the two-three ring level caused by the decrease in entropy in molecular addition steps. Many of the carbon addition reactions at this stage proceed backward because of this. A critical step for soot formation is the still widely debated physical-chemical dimerization of PAHs.

Sabbah H. et al. present experimental measurements concerning dimerization reactions for some small molecules such as pyrene showing that such class of reaction is not favored at high temperature even taking into account of Van der Waals interactions [50]. Their results show that the equilibrium of the reaction strongly favors the dissociation of the dimer proving that pyrene cannot be a key intermediate in hot environments. Despite case-studies on small radicals [51], it has been demonstrated that some examples of dimerization reaction drive to covalently bound closed-shell dimers. The dimerization process is a barrierless reaction and the product conjugation loss leads to energy lower than a typical C-C bond energy as for indenyl (C_9H_7), i.e., π-radicals resonantly stabilized. The barrierless dimerization and the lowered successive H-abstraction energy requirement release more than 100 kcal/mol (zero-point corrected energies), minimizing reversibility. As a direct consequence the dimer is much more stable, and the successive propagation step is much more favored. These reactions represent a repeatable class of pathways for cluster formation to extend the sizes of clustered species by RSR addition to accelerate the growth process. This scheme concentrates

clustering on a limited number of seeds and readily attaches species too volatile to condense via dispersive forces at high temperatures as in the study of Martin et al. [52]. RSR extended conjugations requires an unpaired electron and clustered species add edge sites that can become activated through H-abstraction.

From subsequent work by Martin et al. [53] sigma-radicals were found to be the most reactive species, forming larger radicals and some reactive closed shell edge PAHs. Partially saturated rim-based pentagonal rings were found to form localized π-radicals with high reactivity by sticking. These radicals can form strongly bound stacked complexes, indicating their potential important role in soot formation.

The presence of five-membered rings observed in several PAHs, as in indene, is of vital importance for the final structure of soot nanoparticles subsequently originated because of their abundance [54]. As observed by Dente et al. [55] cyclopentadienyl radical (C_5H_5•) by self-recombination generates the route to naphthalene ($C_{10}H_8$).

Theoretical calculations have been carried out by Cavallotti et al. [54] with a re-examination of the PES with complete set of $C_{10}H_{10}$ isomers highlighting recombination of cyclopentadienyl leading to the formation of azulyl radicals at 1200 K and the fulvalenyl one at 1450 K. The experimental study of toluene pyrolysis performed by Colket and Seery [56] observed the importance of the benzyl radical (C_7H_7•) leading to decomposition to cyclopentadiene and to radicals' recombination products. Accordingly, addition of heavy unsaturated and aromatics species was included, as for phenyl addition to naphthalene, naphthyl addition to benzene and so on.

The gas-phase kinetics involves the formation of the first aromatic hydrocarbons up to the first component of the soot kinetic mechanism ($C_{20}H_{16}$ and $C_{20}H_{10}$).

The soot kinetic model is based on species and reaction lumping, analogy, and rate rules. Similarity with gas phase kinetics is used to extend the soot mechanism up to the formation of species with more than 10^8 carbon atoms. Lumping approach is commonly adopted in kinetic modeling of large PAHs to address an otherwise un unmanageable problem in terms of species and chemical pathways. While dealing with kinetic mechanism PAHs and their isomers are classified in peri-condensed aromatic hydrocarbons (PCAH) with only double bonds among carbon atoms, and incompletely condensed oligomers of PAHs with a less unsaturated structure which come from the Aromatic Aliphatic Linked Hydrocarbons (AALH) class. The first class is characterized by lower H/C similarly to graphene sheet [57]. Subsequent dehydrogenation of oligomers can lead to PCAH. PCAH are characterized by lower H/C, which decreases with the increase of the size of the molecule up to the asymptotic value of a graphene sheet, as shown in Figure 2.9.

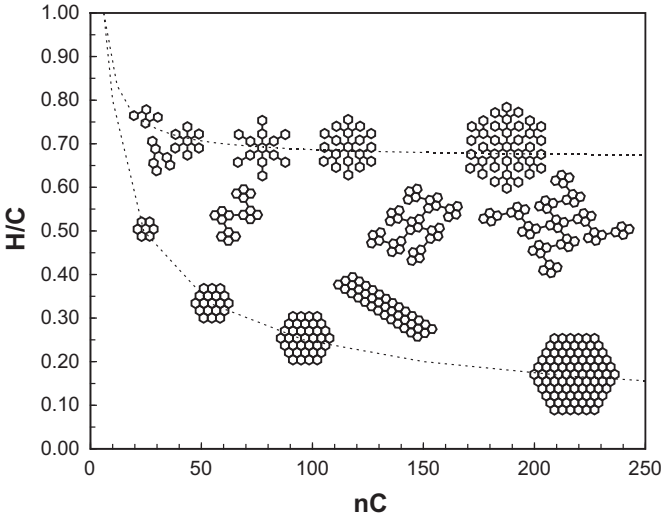

Figure 2.9: H/C trend for PAHs with increasing numbers of carbon atoms (nC) [58].

It is universally accepted that sequential inception, coagulation, surface growth and agglomeration steps take place. In a laminar diffusion flame, inception leads to the first soot nuclei up to primary particles, till reaching mature aggregates as the unburnt gas cool down, as reported in Figure 2.10.

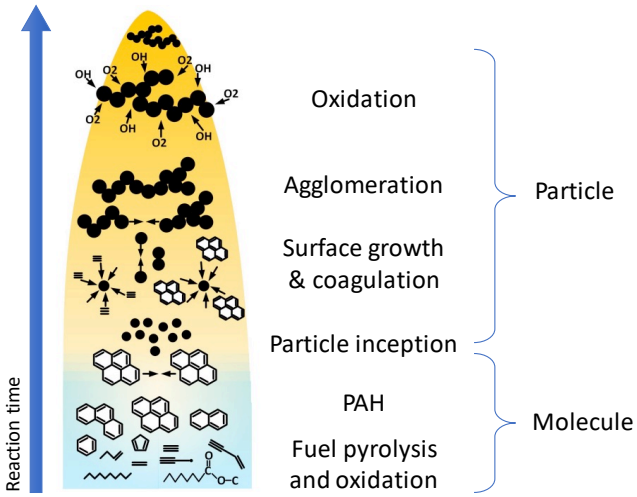

Figure 2.10: Soot Formation Steps [59].

2.4 Soot Formation and Oxidation

As previously discussed, transition from gas-phase to the solid one is the most challenging aspect in the understanding of soot formation mechanism. A critical point is the dimerization of PAHs previously described that can occur following different pathways:

I. Fullerenic mechanism expects the coupling of two-members PAH with five-membered rings into curved structures.

II. Coagulation pathway is proved to be the most relevant one at high temperature conditions, while chemical growth is balanced by thermal fragmentation, thus favoring thermal reversibility. This

mechanism explains dimerization thanks to physical coagulation, and it proves consistent with strong electrostatic and dispersive forces.

III. Aliphatic linkages are adopted as the third and last option, reactions between aromatic molecules and aryl radical govern the chemical coalescence of PAHs.

However, the above conceptual pathways cannot correctly explain the transition from gas to particles and additional alternatives are required.

Frenklach and co-workers, suggested that "starting with a prescribed size" PAHs begin clustering. The numerical model is constructed in harmony with the knowledge of particle internal structure, PAH-precursor hypothesis, and surface growth and oxidation, assuming that the PAH clustering is due to physical forces as at point I [60]. As already discussed in the previous paragraph, the thermodynamic stability of small PAHs is alarmingly low and consequently possible forces holding them together as for their clusters have been investigated as in point II and III and two possible factors were highlighted: ionic forces and crosslinking as proposed by Miller et. al [57]. This mechanism allows to explain soot particles growth considering not just aromatics structures but also aliphatic and it is generally applicable for conditions under which hydrocarbon radicals can form and react at high temperature. Additional studies are needed to investigate reaction rates and yield of these RSRs, rates and identities of nucleated particles and to deeply understand the surface growth mechanism. Soot nucleation is one of the main objects of studies driving PAHs from physical to chemical dimerization. Wang suggested that the pathways of moderated-sized PAH-PAH interactions binding together with a bond as strong as a typical covalent bond reaching a mechanism more like chemical dimerization than a physical one. Johansson et al. proposed a new mechanism involving radical-chain reaction (CHRCR) leading to increasingly larger and more stable radicals. Resonantly stabilized radicals grow mainly through acetylene and vinyl addition, followed by the clustering between available hydrocarbons and radicals produced in the first stage [45]. Once formed, soot nuclei continue to grow via surface chemical reactions, PAH condensation and particle agglomeration. Particle's coalescence drives to larger structures while the growth firstly come from PAHs deposition on the surface of smaller ones and because of absorption of gas-phase on the solid surface of soot the result is like stacking of PAHs. After the first core of soot is formed it collides to generate bigger structures, this process is called coagulation. Coalescence occurs when two particles collide and merge to form a single larger particle like two colliding liquid droplets. The coalescence process tends to reduce free surface to minimize free energy. Following coagulation, agglomeration occurs, and particles collide sticking to each other to form chain-like fractal structures. Agglomerated structured reached at the end of the process are spot like particles [61]. Coagulation changes soot morphology, number density and particle size distribution, without changing the total mass of soot

formed. It can be distinguished in two types of coagulation, i.e., coalescence and agglomeration, as depicted in Figure 2.11.

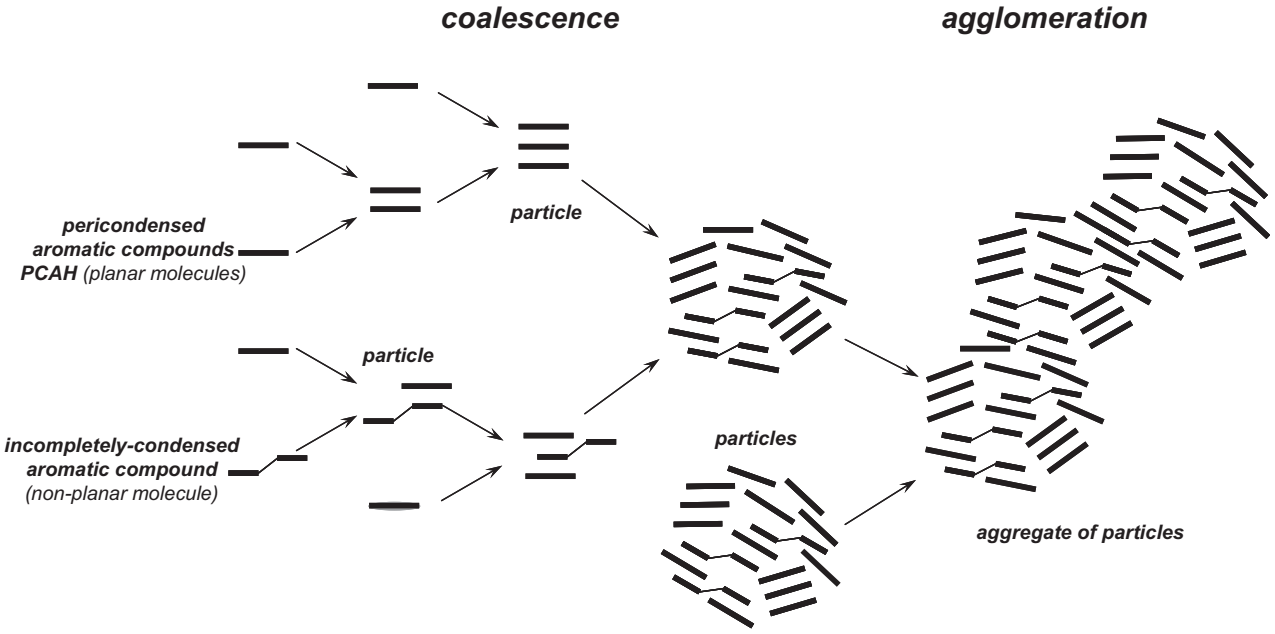

Figure 2.11: Scheme of the coagulation process [62].

Numerous experimental studies have been performed to understand the transformation of PAH soot particles but there is still a lack of complete understanding of the key intermediates, either neutral or radical in nature that populates the mechanistic pathways of this fundamental process.

Soot oxidation process is of interest for pollution control in industrial flames, engines etc. Oxidation can be achieved with oxygen, carbon dioxide, water vapor or nitrogen dioxide leading to the removal of soot particles from exhausted gaseous species [63]. Gaseous oxidant must move to the surface and be adsorbed to form surface intermediates, which rearrange, desorbs and escape in gas phase [64]. Soot oxidation is a combination of different phenomena, and it is influenced by conditions, curvature and, soot nanostructure [65]. The complexity of the process makes difficult to understand the mechanism and the incorporation inside kinetic models and flame simulations.

The solid black phase is oxidated in gas phase mainly by the contribution of OH•, O•, and O_2 [66]. The identified main reaction is the oxidation via OH radical collision on the particle surface while molecular oxygen is of interest because of induced fragmentation [67] [68]. O_2 can penetrate inside soot particles or through bridges of soot aggregates till they break up, counter wise OH• is too reactive and it is quickly consumed. At flame temperature i.e., 1500 K, O_2 diffusivity does not control the process but it is a chemical regime-controlled scenario [69].

Many studies have been carried out concerning soot oxidation dealing with different operative conditions and, both premixed-flame and counter-flow diffusion flames. Experimental data have been collected and together with their validation, mechanism studies are still of interest because the soot oxidation process is considered a competitor of the growth one as shown in Figure 2.12.

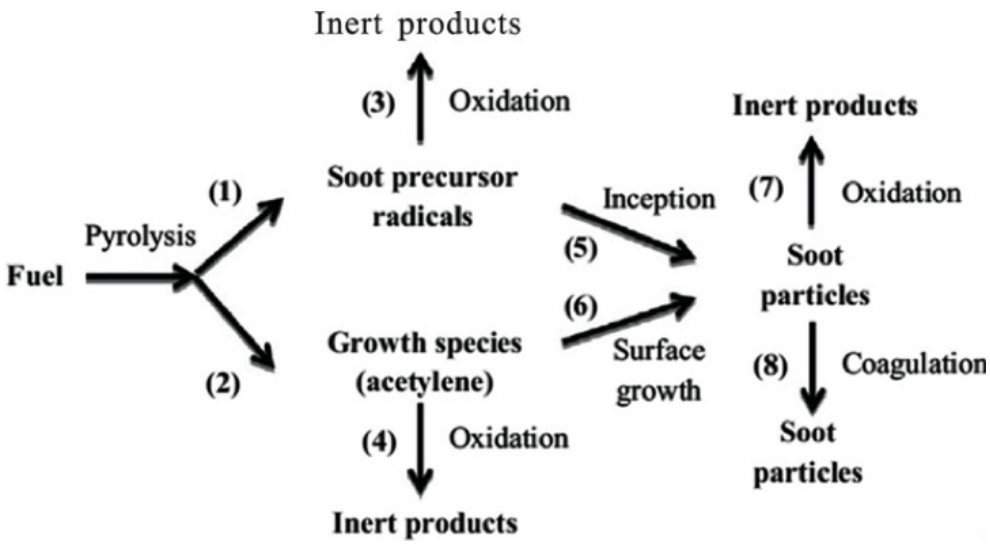

Figure 2.12: Schematic Diagram of Soot Model [70].

Furthermore, oxidation is affected by the soot aging [71] [72]. Young particles are characterized by a more disordered structure and with oxygen insertion into the core the oxidative process is carried out from the inside, while the more mature they are, the more they are graphitic, and oxidation occurs at the surface. During aggregates oxidation, the graphitic shell of primary particles burns away [73]. The remaining amorphous cores subsequently coalescence each other, and form new large spherical-like cluster before they are completely burned away. Empirically derived rate expressions as Nagle and Strickland-Constable (NSC) have been developed as for physically based model such as the one from Appel at al. (ABF) [74] [34].

Soot formation models involves large chemical reaction mechanism and aerosol dynamics to describe the complex superposition of many phenomena such as gas pyrolysis, particles inception, and surface growth. The types of soot models can be divided up into three main groups: empirical, semi-empirical and detailed soot models [75]. In order to accurately predict the soot emission from different practical fuels' combustion, the detailed description of soot precursor formation in the key sub-model is required. Detailed theoretical models are comprehensive of both gas-phase kinetic and dynamic of soot particles. Despite of the wide range of reactions and components involved in these models the main drawbacks are the computational cost and lack of applicability especially when it is integrated into CFD simulations of engine combustion.

2.5 PAHs Dimerization Kinetics

Dimerization reactions investigated in previous work by Menon et al. [76] involve some classes of PAHs as monomers characterized by different reactive edges, including aromatic compounds which become radicals when subjected to H-abstraction and rim-based pentagonal rings have been observed to be thermally stable [77].

Five-membered rings are not aromatically stabilized and thus provide a free edge with double-bond character and significant reactivity. Low aromaticity free edges are supposed to react with carbon σ-radicals, leading to the formation of dimers in flame through the Aromatic Aliphatically Linked Hydrocarbon (AALH) mechanism [52].

σ-radicals studied are aryl-type radicals, as A1 and A2 in Figure 2.13, which can be generated by the abstraction of a hydrogen atom from the rim of a PAH. A1 has the radical site in the five-member ring, while A2 on the six-member ring. Different classes of reactions are studied concerning those monomers reacting with both five-member ring PAHs and delocalized π-radicals following the CHRCR mechanism [53].

The second group of monomers is the one involving localized π-radicals, i.e., B1 and B2 in Figure 2.13. Localization of π-radicals was also demonstrated in partially saturated rim-based pentagonal rings, methylene groups and five-membered rings which react following Aromatic Rim-Lined Hydrocarbons (ARLH) [76]. Localized π-radicals can include partially saturated rim-based pentagons, such as B1, and those with odd number of electrons in the π-network like B2. This class of monomers are so called because of their concentrated spin density on a specific site.

Finally, also delocalized π-radicals such as C (see Figure 2.13) are considered. PAHs like C have an odd-number of C-atoms, but the electron density delocalizes across the network, indicating that their reactivity dissipates across the rim.

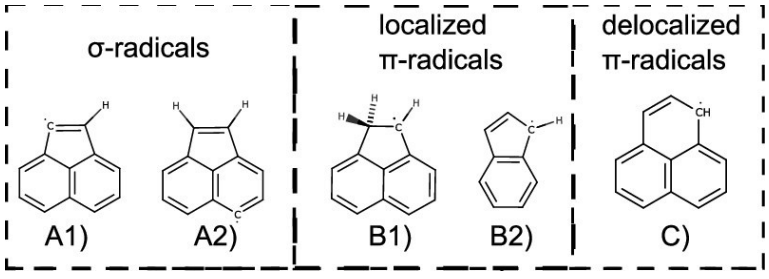

Figure 2.13: PAH monomers adopted from [76].

Figure 2.14 shows how spin density is distributed on carbon atoms dealing with different PAHs. For instance, according to what previously mentioned, case c) presents a radical localization on a particular site, which is the unsaturated pentagonal ring site, as highlighted in blue. The fact that this site is not significantly delocalized makes it the most reactive one.

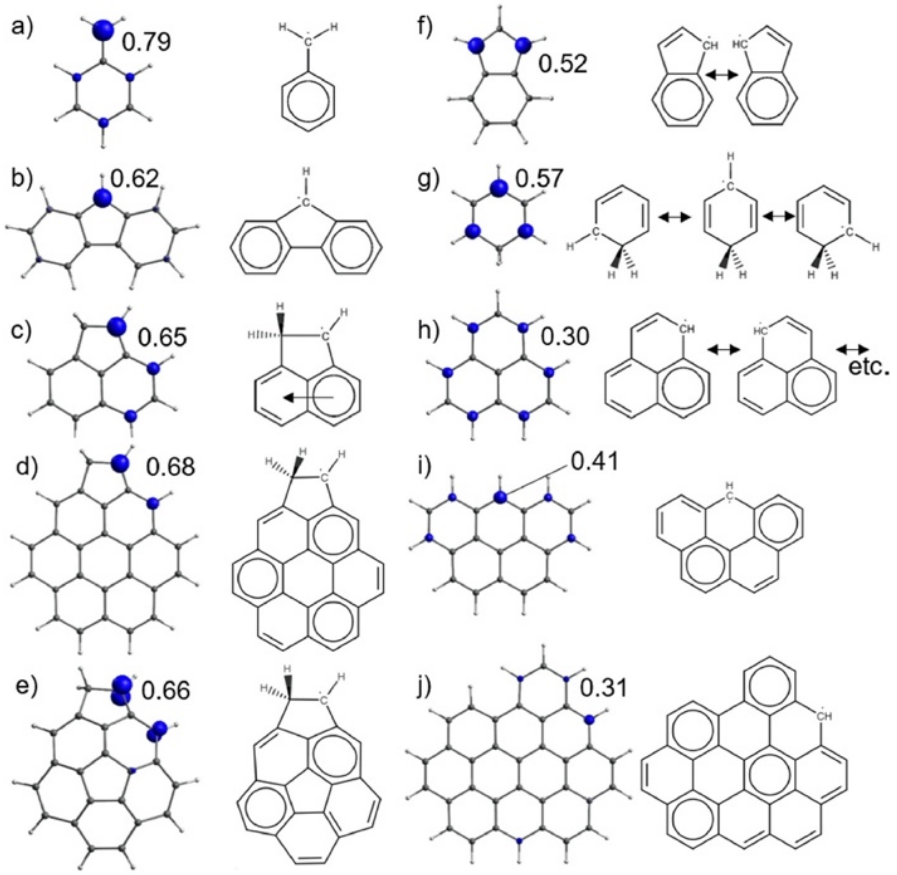

Figure 2.14: Spin Density on Molecular Geometry adopted from [77].

In Figure 2.15 some resonance structures for 1,2-dihydroacenaphthylen-1-yl are depicted, even if by the analysis of the average local ionization potential and spin density they have been proved to not uniformly populates the environment at flame temperature [77]. The first two resonance structures have a sextet on the hexagonal rings with the radical localized to the pentagonal ring and they are the preponderant ones. The third and the fourth resonance structures have the radical on the aromatic ring, i.e., the β- and δ-positions from the pentagonal site. To keep the aromaticity on the six-membered ring localization of the five-membered one is exploited.

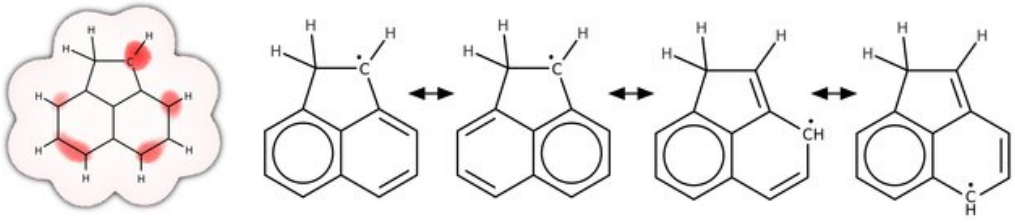

Figure 2.15: Resonance Structures of 1,2-dihydroacenaphthylen-1-yl adopted from [77].

Case f) in Figure 2.14 shows the impact of delocalization of the radical character but the aromaticity still drives the location of the delocalized π-radicals to a favored configuration. Indenyl is characterized by resonance between two sites which are equivalent.

Case h) in Figure 2.14 shows that the π-radical in completely delocalized on the entire PAH. The six-membered ring delocalized π-radical has the unpaired electron split over six different sites, still driven by aromaticity. This electronic configuration provides an enhanced stability of the monomer leading to lower reactivity concerning dimerization reactions sometimes leading to the introduction of an energy barrier as will be discussed later.

Previous work from Menon et al. [76] provides a kinetic study on the monomers mentioned above while dealing with PAH recombination reactions participating to PAHs growth. As shown in Figure 2.13, the reactive edges have been described and grouped. All the monomers geometries already mentioned have been optimized, with Gaussian09 [78], at both level 0 and level 1 with M062X/cc-pVTZ from Menon et al. [77], along with energies and thermodynamic properties investigation. The aim of that study was to consider just the first bond formed from the recombination of these small species so corresponding dimers have been optimized too with the same functional and basis set. Single-point energy calculations have been performed to refine previous values with M062X/cc-pVTZ taking care of the presence of a dihedral angle which provide the reciprocal rotation of the two monomers in the dimer configuration.

Coupling together reactants and products results, recombination energies, corresponding the bond dissociation energies, have been computed.

The full set of monomers has been considered and the entire class of product from recombination reaction has been investigated from an energetical point of view as preliminary calculations. Then, as a second step, the kinetic analysis with rate constants estimation has been carried out.

2.5.1 Barrierless Reactions

Starting from five monomers (see Figure 2.13), twelve reactions are analyzed and classified as barrierless. Reactions among the monomers of different radical type are accounted for. The barrierless reactions include the reactions of the aryl σ-radicals with any other PAH with a radical edge type, i.e., A1 and A2 reacting with any PAH with edge types A, B or C, reactions of localized π-radical B1 with itself and delocalized π-radical C, as well as reaction between indenyl (B2) and itself.

Barrierless reactions are generally those between radicals of different types that result in the highest bond energies as highlighted in green in Figure 2.16.

Menon et al. [76] found that bond energies decrease in strength from the aryl σ-radical types seen as A1 and A2 down to low aromaticity. Consequently, aryl-linked hydrocarbons are more likely to form bonds stable at flame temperatures and the dimer would be long-lived. Localized σ-radicals, known as rim-linked hydrocarbons, are less reactive concerning this reaction class but still more reactive than delocalized species

according to their cross-linking energies which are higher. The formation of a cross-linking between two aromatics leads to a small drop in the band gap, leading to conjugation effect which give stabilization to the product. It is of particular interest the formation of bonds when σ-radicals as A1 are involved because the minimum energy configuration of the dimer is planar thanks to the absence of steric hindrance due to hydrogen atom. Conversely, when both A2 and B1, the reciprocal position of the monomers in the dimer configuration is not as flat as in the case of A1-A1, leading to a less stable dimer configuration. Finally, when a RSRs such as indenyl (B2) participate to the recombination reaction, the bond energy is lower than a single C – C bond (90 kcal/mol) and it seems to be independent from the nature of the other monomers. RSRs reacting together generate fewer stable dimers with respect to σ-radicals as A1 because of limited conjugation and stabilization by delocalization. Also, C monomer recombination is the less favored because of the high monomer's stability due to the unpaired electron delocalization, which contributes to reduce of the BDE.

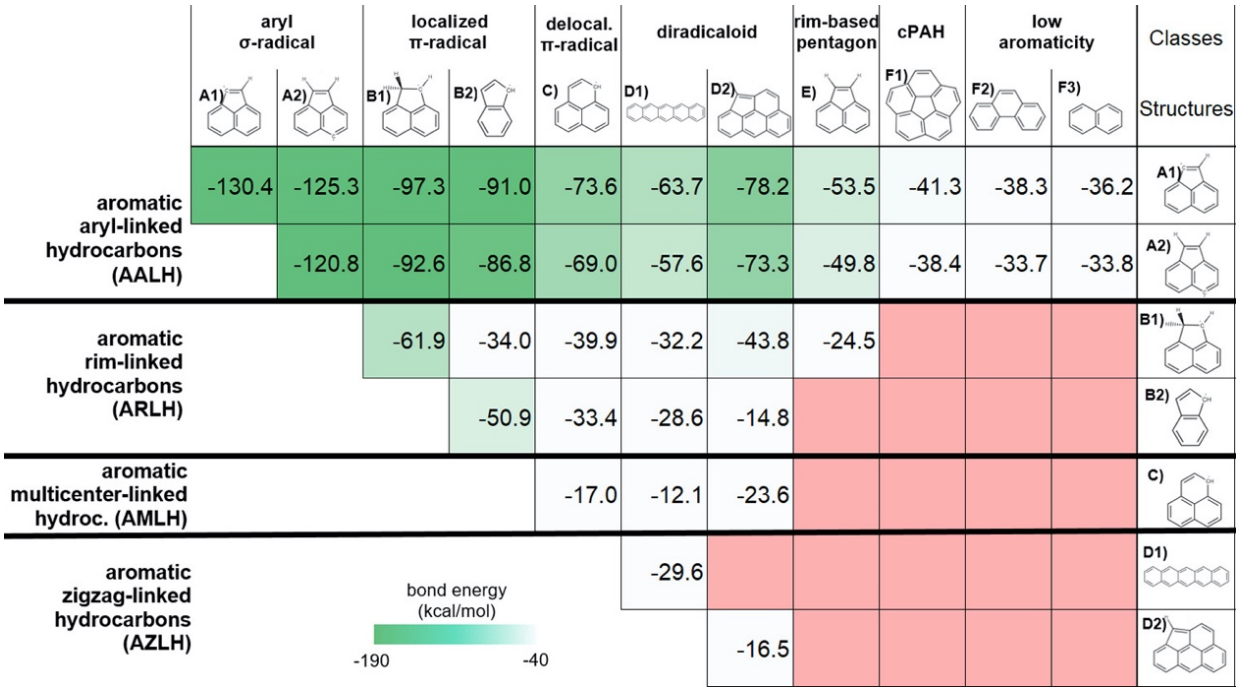

Figure 2.16: Bond energies of cross-linking between PAHs of different edge types computed at the M06-2X-D3/cc-pVTZ level of theory. The red shading indicates a bond energy less than 10 kcal/mol. A gradient of green shading is applied starting from bond energies of 40 kcal/mol. Adopted from [76].

Following this preliminary introduction and considering this class of reactions involving VTST routine, Potential Energy Surface has been scanned and reconstructed by Menon et al. [76] performing a step-by-step simulation with scission mechanism leading to dimer dissociation.

Figure 2.17 shows the potential energy surfaces for barrierless reactions involving the monomers and studied by Menon et al. This reaction class is of interest because it plays a key role in PAH growth. Barrierless dimerization reactions are presented in Figure 2.17 with the corresponding cross-linking energy computed by Menon et al. [77], as mentioned above. The first-bond formation is conceptually important for the cross-

linking reaction as the reaction is not entropically favored due to the reduction in the number of species and therefore the bond energy directly corresponds to the likelihood of the complex fragmenting according to the enthalpy of reaction.

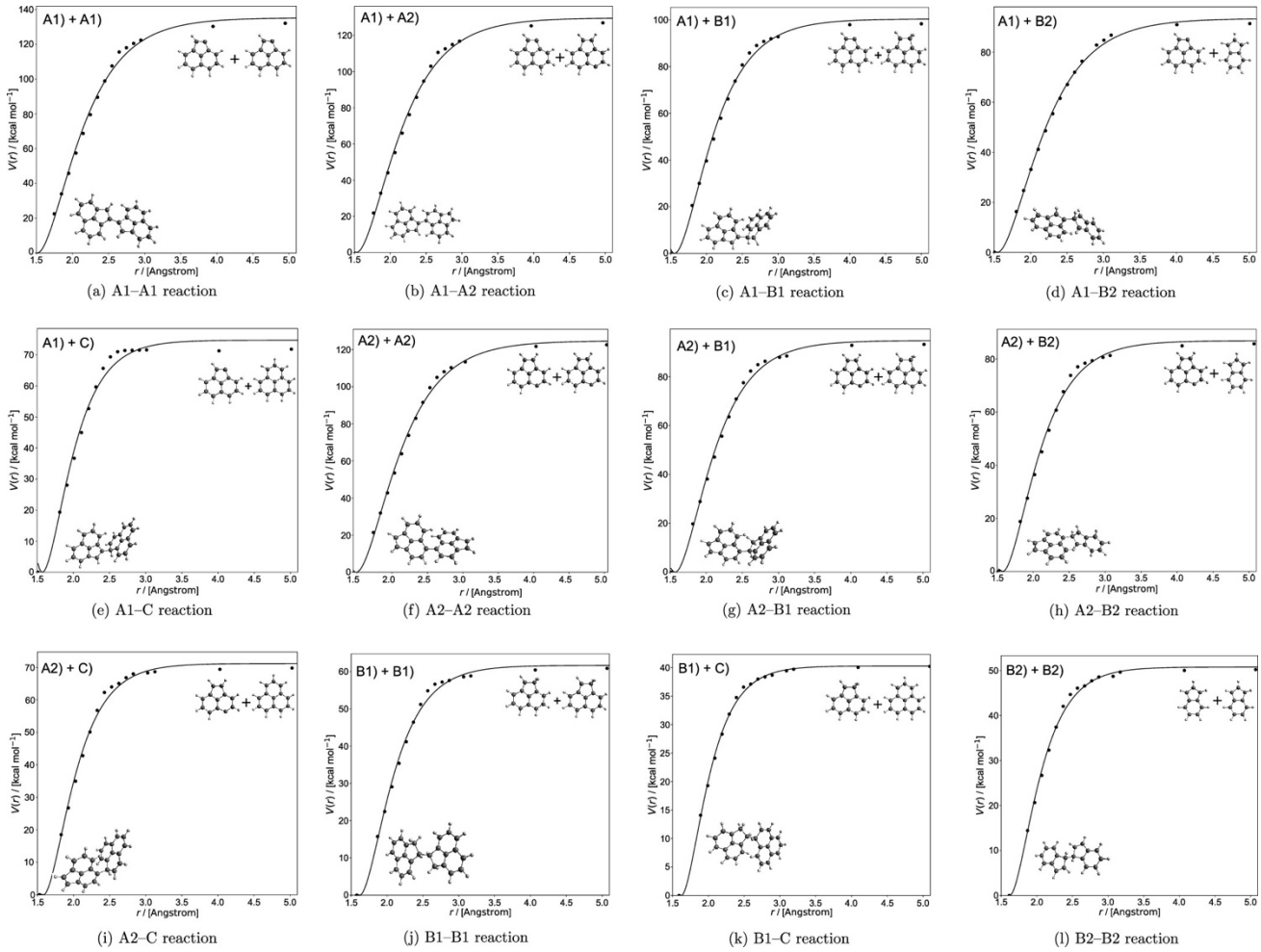

Figure 2.17: Potential Energy Surfaces for barrierless cross-linking reactions adopted from [76].

2.5.2 Reactions with Barriers

As briefly mentioned in the previous paragraph some cross-linking reactions results as barrierless but some of them features a transition state, i.e., a not null energy barrier. As for barrierless reactions, the energy of the products is much lower than that of the reactants, leading to a more stable configuration.

Reactions with barrier have been investigated by Menon et al. [76] using the same method as for barrierless reactions. It is known that barrier heights for a family of reactions tend to have a linear relationship between the barrier height and the enthalpy of reaction [53].

Cross-linking reactions considered involve the delocalize π-radical C with other edge types, reaction of localized π-radical edge type B with non-diradicaloid edge types as B and C, and reactions of the aryl σ-radical types A with planar PAHs. Cross-linking reactions involving delocalized π-radical C generally show high energy

barriers. This is mainly correlated to its aromatic stabilization, which also results in a delocalized electron density and lower reactivity. In general, chemical bonds between five membered rings seem to be less favorable unless there is sufficient radical character among the reacting PAHs. This reaction class is characterized by an energy barrier larger than 2 kcal/mol and an enthalpy lower than 40 kcal/mol, with an almost linear relationship among larger aromatic structure with analogous radical behavior.

2.5.3 Rate Constants

Rate constants computation has been performed by Menon et al. for the entire set of recombination reactions previously reported. The forward rate constants for the reactions with barriers are concave in nature, with the phenomenological activation energies increasing with temperature. Looking at the rate constants, at the higher temperature range of interest to flames (1500K-2000K), the rate constants span four orders of magnitude, from approximatively 10^8 $cm^3mol^{-1}s^{-1}$ to 10^{12} $cm^3mol^{-1}s^{-1}$. In the case of barrierless reactions, at the temperature range of 1500-2000 K, the rate constants are in a similar range, from approximatively 10^8 $cm^3mol^{-1}s^{-1}$ for the reactions with the lowest bond energies between localized π-radical B and delocalized π-radical C to slightly below 10^{12} $cm^3mol^{-1}s^{-1}$ for the higher bond energies between reactive edges type A and B.

In Figure 2.18 rate constants for barrierless reactions shown in Figure 2.17 are reported. It can be seen that the barrierless reactions between two indenyls or B2 and between B1 and C are lower in magnitude and more temperature-dependent. In contrast, the reactions between A1 and A2, A1 and B1, A1 and B2 and A2 and B2 are higher in magnitude. Also, it is commonly observed that other reactions involving σ-radicals are weakly temperature-dependent which is commonly observed for barrierless reactions. The rate constants for all the barrierless reactions show regions of negative temperature dependence around 1600-1700 K. Recombination rate constants involving species A1 are larger than for the counterpart reactions involving species A2 suggesting that the reactivity of the σ-radical is higher for a radical site on a rim five-member ring than a six-member ring. The importance of localized π-radical is exemplified by the fact that the rate constants for the reactions between A1 and the localized π-radicals B1 and B2 are some of the largest. This suggest that reactions between σ-radicals and π-radical are possible and may indeed be important.

The concentration of radical PAHs is likely to be lower than that of PAH molecules, the higher rate constants for cross-linking between edge types A and B could be offset by their lower concentration. Substantial radical concentrations are also required for the cross-linking reactions of aryl σ-radicals and localized π-radicals to play a role.

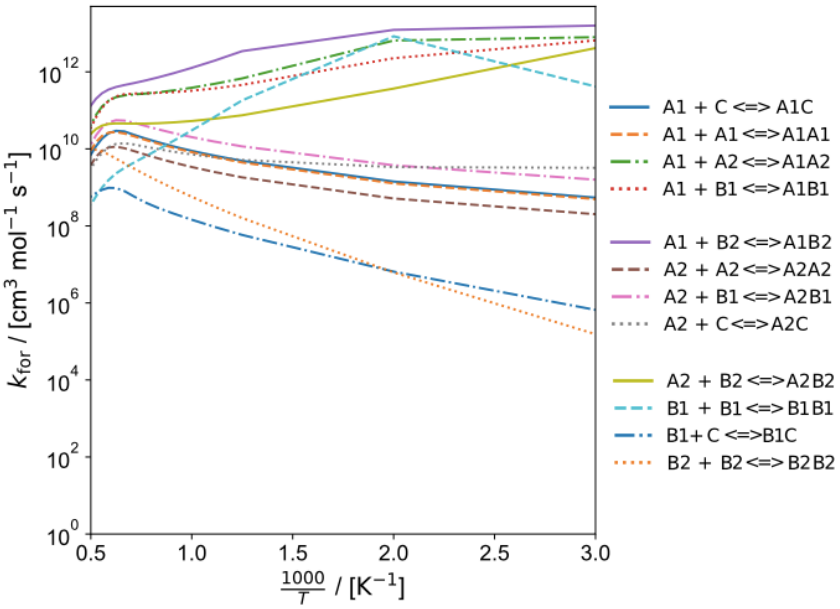

Figure 2.18: Rate Constants for Barrierless Reactions adopted from [76].

In the case of reactions with barriers, the forward and reverse rate constants have been fitted to the modified Arrhenius expression:

$$k = AT^{n} exp\left(-\frac{Ea}{RT}\right) \qquad 2.1$$

In the case of barrierless reactions the forward rate constants requires a sum of two modified Arrhenius expression.

2.5.4 Thesis further developments

In this thesis the work form Menon et al. [76] has been taken as reference to start a deeper investigation into PAHs reactivity exploiting more accurate theoretical methods with the aim to reach more valid results for reaction classes governing PAHs growth and soot formation.

Some steps can be highlighted to better understand the implemented approach:

- Preliminary ab initio calculations for reactants, products, and transition states and so bond energy and barrier heights computation with the method suggested by Menon et al. and with additional DFT functionals providing comparisons between different accuracy levels.
- PES reconstruction and rate constants computation for reaction with and without barriers respectively with TST and VTST.
- Larger PAHs investigation starting from geometry optimization and electronic energy computation until bond energy calculation involving self-recombination reactions.

- Rate rules development for some classes of reactions starting from smaller structures which are progressively enlarging by one to three aromatic ring additions.
- CRECK soot kinetic mechanism update and validation implementing rate constants of reactions previously analyzed as a reference and to lump the entire set of species and reactions involved to avoid inclusion of unimportant intermediates and reaction classes.

Chapter 3 – Methods

In the present chapter, a brief overview about general concepts of Computational Quantum Chemistry is presented together with methods used for preliminary calculations. A complete description of the theoretical background can be found in computational chemistry book [79] [80]. Ab initio calculations are a powerful tool used for the determination of molecular structures, energies, and frequencies. Finally, some notions concerning rate constants computations are discussed taking into account of both temperature and pressure dependence.

3.1 Computational Quantum Chemistry Overview

The aim of the next paragraphs is to establish the basic elements of the most widely used quantum mechanical methods in molecular modeling. Computational chemistry simulates chemical structures and reactions numerically through the fundamental laws of physics. Some methods can be used to simulate not just stable molecules, but also short-lived, unstable intermediate and even transition state. The development of quantum mechanical techniques that are more generally applicable and that can be implemented on a computer (eliminating the need for much laborious by-hand calculation) means that quantum mechanism can now be used to perform calculations on molecular systems of both real and practical interest. Quantum mechanics explicitly represents the electrons in a calculation, and so it is possible to derive properties that depend upon the electronic distribution and to investigate chemical reactions in which bonds are broken and formed [81]. Quantum mechanics problems seems to be very challenging and as a simplification, very simple system can be applied to much more complex ones.

Concerning kinetic study on large PAHs several reactions will be investigated in this thesis. Energies and thermodynamic properties of all the chemicals species that are of interest are determined using Rigid Rotor Harmonic Oscillator Approximation (RRHO). Rigid Rotor means that the distance between atoms in a molecule do not change as they rotate. Even if a molecule vibrates as it rotates, and the bonds are elastic rather than rigid, RRHO can be considered a reasonable approximation to reach the main goal: molecules behavior simulation [82].

There are two broad areas within computational chemistry devoted to the structure of molecules and their reactivity: molecular mechanics and electronic structure theory. They both perform the same type of calculations:

- Computing the energy of a particular molecular structure and related properties.
- Performing geometry optimizations, which locates the lowest energy molecular structure according to the energy gradient as the first derivative of the energy with respect to atomic position.

- Computing the vibrational frequency of molecule resulting from interatomic motion within the molecule expositing the second derivative dependance of the energy with respect to atomic structure.

There are many different molecular mechanics methods and each one is characterized by its force field. The set of equations defining the potential energy dependance on molecule varies with the locations of its component atoms. A series of atom types defines the characteristics of an element within a specific chemical context. Atom types prescribe different characteristics and behavior for an element depending upon its environment. Atom types depend on hybridization, charge, and the type of the other atoms to which it is bonded. Parameter sets which define force constants are values used in the equations to fit with experimental data such as bond length and angles.

Molecular mechanics calculations do not explicitly treat the electrons in a molecular system. Calculations are based on nuclei interactions. Electronic effects are implicitly included in force fields through parametrization. On the other hand, electronic structure methods use the laws of quantum mechanics rather than classical physics as the basis for their computations. The starting point for any discussion of quantum mechanics is the Schrödinger equation. The Schrödinger equation is a linear partial differential equation that governs the wavefunction of a quantum-mechanical system. It gives the evolution over the time of a wave function leading to the quantum-mechanical characterization of an isolated physical system. The wave function provides a complete description of the system. The full, time-dependent form of this equation is:

$$\left\{-\frac{\hbar^2}{2m}\left(\frac{\partial^2}{\partial x^2}+\frac{\partial^2}{\partial y^2}+\frac{\partial^2}{\partial z^2}\right)+\mathcal{V}\right\}\Psi(\boldsymbol{r},t)=i\hbar\frac{\partial\Psi(\boldsymbol{r},t)}{\partial t} \qquad 3.1$$

Equation 3.1 refers to a single particle of mass m which is moving through space (given by the position vector ($r = xi + yj + zk$), and time (t) under the influence of an external field $\mathcal{V}$ (which might be the electrostatic potential due to the nuclei of a molecule). $\hbar$ is Plank's constant divided by 2π and $i = \sqrt{-1}$. Ψ is the wavefunction which characterizes the particle's motion and in turn particle properties.

When the external potential $\mathcal{V}$ is independent of time then the wavefunction can be written as the product of spatial term and time term: $\Psi(r,t) = \Psi(r)\mathrm{T}(t)$ leading to the time-independent form of the equation:

$$\left\{-\frac{\hbar^2}{2m}\left(\frac{\partial^2}{\partial x^2}+\frac{\partial^2}{\partial y^2}+\frac{\partial^2}{\partial z^2}\right)+\mathcal{V}\right\}\Psi(\boldsymbol{r})=E\Psi(\boldsymbol{r}) \qquad 3.2$$

Here, E stands for the energy of the particle.

$$\nabla^2=\frac{\partial^2}{\partial x^2}+\frac{\partial^2}{\partial y^2}+\frac{\partial^2}{\partial z^2} \qquad 3.3$$

$$\mathcal{H} = \left\{ -\frac{\hbar^2}{2m}\nabla^2 + \mathcal{V} \right\} \quad 3.4$$

In 3.4 the Hamiltonian operator includes the terms related to the kinetic and potential energy, respectively. By substituting both 3.3 and 3.4 in 3.2 the reduced Schrödinger equation is obtained:

$$\mathcal{H}\Psi = E\Psi \quad 3.5$$

To solve the Schrödinger equation, it is necessary to find values of Ψ and E such that, when the wavefunction is operated upon the Hamiltonian, it returns the wavefunctions multiplied by the energy.

The Schrödinger equation falls into the category of equations known as partial differential eigenvalue equations in which an operator acts on a function (the eigenfunction) and returns the function multiplied by a scalar (the eigenvalue). In the Schrödinger equation Ψ is the eigenfunction and E the eigenvalue. The Schrödinger equation can be solved exactly only for few problems, such as particle in a box, the harmonic oscillator, the particle on a ring, the particle on a sphere and the hydrogen atom. Assuming the previously cited RRHO approximation we can simplify the Schrödinger equation formulation as follow:

$$\left\{ -\frac{\hbar^2}{2m}\left(\frac{\partial^2}{\partial x^2}\right) \right\} \Psi + \frac{1}{2}m\omega^2 x^2 \Psi = E\Psi \quad 3.6$$

Where x is the displacement and ω the angular frequency.

$$\Psi_n(x) = \sqrt{\frac{1}{2^n n!}} \left(\frac{m\omega}{\pi\hbar}\right)^{1/4} e^{-\frac{m\omega x^2}{2\hbar}} \mathcal{H}_n\left(\sqrt{\frac{m\omega}{\hbar}}x\right) \quad 3.7$$

$$\Psi_n(x) = \frac{1}{\sqrt{n!}}\left(\sqrt{\frac{m\omega}{2\hbar}}\right)^n \left(x - \frac{\hbar}{m\omega}\frac{d}{dx}\right)^n \left(\frac{m\omega}{\pi\hbar}\right)^{1/4} e^{-\frac{m\omega x^2}{2\hbar}} \quad 3.8$$

In equation 3.8 the solution in space where $n \in \{0, 1, 2, \ldots\}$ and $\mathcal{H}_n$ the Hermite polynomials of order n.

$$E_n = \left(n + \frac{1}{2}\right)\hbar\omega \quad 3.9$$

E_n from 3.9 are the eigenvalues, the case $n = 0$ is called the ground state, its energy is called the zero-point energy and the corresponding wave function is a Gaussian.

Electronics structure methods are characterized by various mathematical approximation leading to Schrödinger equation solution. There are two major classes of electronic structure methods:

- Semi-empirical methods which involve the approximated solution of the Schrödinger equation that depends on having appropriate parameters.
- Ab initio methods which do not use experimental parameters in their computations.

Semi-empirical and ab initio methods differ in the trade-off made between computational cost and accuracy of result. Semi-empirical calculations are relatively inexpensive and provide reasonable qualitative description of molecular systems. In contrast, ab initio calculations provide high quality quantitative predictions for a broad range of system, but they require a high computational cost.

The least expansive ab initio method is the Hartree-Fock theory which was the most common method for the solution of the electronic Schrödinger equations until the implementation of Density Functional Theory (DFT) based methods.

3.1.1 Hartree Fock Theory

As previously mentioned, the Hartree-Fock (HF) method is an approximation for the determination of the wave function and the energy of a quantum many-body system in a stationary state. In literature it is also called Self-Consistent Field Method (SCF). Nowadays, HF is indeed useful for the understanding of all the methods developed afterwards. The derivation comes from a set of N-coupled equations for the N spin orbitals. A solution of these equations yields the Hartree-Fock wavefunction and energy of the system.

The Hartree-Fock method is typically used to solve the time-independent Schrödinger equation for a multi-electron atom or molecule following the Born-Oppenheimer approximation. The problem is solved numerically by nonlinear method such as iterative ones. Variational theorem states that energy calculated from an approximation to the true wavefunction will always be grater that the true value. The better the wavefunction, the lower the energy. At a minimum, where the best wave function is located, the first derivative of the energy, ∂E, will be zero.

Deriving an approximated solution of the Schrödinger equation in the non-time dependent form (equation 3.6), by numerical resolution with iterative methods returns the wavefunction. HF theory is based on a simple approximation to the true many-body wavefunction: the wavefunction is given by a single Slater Determinant (SD) of N-spin orbitals.

$$\Psi = \begin{pmatrix} \psi_1(x_1) & \cdots & \psi_1(x_N) \\ \vdots & \ddots & \vdots \\ \psi_N(x_1) & \cdots & \psi_N(x_N) \end{pmatrix} \qquad 3.10$$

Where x variables include the coordinates of space and spin. The wavefunction can be written as a Hartree products $\psi_i(x_i)$ which is the product of the spatial part and the spin part.

Most importantly, the wavefunction is antisymmetric with respect to an interchange of any two-electron position. This property is required by the Pauli exclusion principle:

$$\Psi(x_1, x_2, \ldots, x_i, \ldots, x_j, \ldots, x_N) = -\Psi(x_1, x_2, \ldots, x_j, \ldots, x_i, \ldots, x_N) \qquad 3.11$$

The wavefunction can be inserted into the Hamiltonian and the expression for the total energy can be derived. Choosing ψ as an orthonormal set and introducing a Lagrange multiplier ϵ_i to impose the condition that ψ are normalized it is possible to minimize with respect to ψ.

$$\frac{\delta}{\delta\psi}\left[\langle\widehat{H}\rangle - \sum_j \epsilon_j \int |\psi_j|^2 d\boldsymbol{r}\right] = 0 \qquad 3.12$$

$$-\frac{1}{2}\nabla^2\psi_i(\boldsymbol{r}) + V_{ion}(\boldsymbol{r})\psi_i(\boldsymbol{r}) + U(\boldsymbol{r})\psi_i(\boldsymbol{r}) = \epsilon_i\psi_i(\boldsymbol{r}) \qquad 3.13$$

Where $U(\boldsymbol{r})$ is a non-local potential and $V_{ion}(\boldsymbol{r})$ is the local ionic potential. The one-electron equations resemble single-particle Schrödinger equation.

$$\begin{aligned}\epsilon_i\psi_i(\boldsymbol{r}) = \left(-\frac{1}{2}\nabla^2 + V_{ion}(\boldsymbol{r})\right)\psi_i(\boldsymbol{r}) + \sum_j \int \frac{|\psi_j(\boldsymbol{r}')|^2}{|\boldsymbol{r}-\boldsymbol{r}'|}\psi_i(\boldsymbol{r})d\boldsymbol{r}' \\ - \sum_j \delta_{\sigma_i\sigma_j}\int \frac{\psi_j^*(\boldsymbol{r}')\psi_i(\boldsymbol{r}')}{|\boldsymbol{r}-\boldsymbol{r}'|}\psi_j(\boldsymbol{r})d\boldsymbol{r}'\end{aligned} \qquad 3.14$$

Equation 3.14 is the full Hartree-Fock equation. The right terms are given by the kinetic energy contribution and the electron-ion potential. The third term, named Hartree term, is the simply electrostatic potential arising from the charge distribution of N electrons. Hartree-Fock theory neglects correlation between electrons. Electrons are subject to an average non-local potential arising from the other electrons, which can lead to a poor description of the electronic structure.

Numerical solution of the HF equation can be provided by expanding the orbitals in a basis set $\psi_i = \sum_k^M c_{ik}\phi_k$ where c_{ik} are expansion coefficients while ϕ_k the basis functions. Hartree-Fock orbitals are optimized iteratively until the change in total electronic energy falls below a predefined threshold. In this way a set of self-consistent one-electron orbitals is calculated and the HF wavefunction can be used to compute any desired chemical or physical property within the framework of the method according to approximations employed.

3.1.2 Density Functional Theory

Density Functional Theory (DFT) is a computational quantum mechanical modelling method used to investigate the electronic structure of many-body systems as atoms, molecules, and condensed phases. DFT implementation cost is relatively low, and it is the most versatile method available. Assuming the Born-Oppenheimer approximation nuclei of the treated molecules and clusters are seen as fixed generating a static external potential V, in which the electrons are moving. A stationary electronic state is described by the wavefunction $\Psi(\boldsymbol{r}_1,\ldots,\boldsymbol{r}_N)$ satisfying the many-electron time-independent Schrödinger equation. The previously mentioned Hartree-Fock method is the simplest one to provide a solution while the DFT one

provides an appealing alternative, being more versatile. In DFT the key variable is the electron density $n(\boldsymbol{r})$ which for normalized Ψ is given by:

$$n(\boldsymbol{r}) \;=\; N \int d^3\boldsymbol{r}_2 \;.\;.\;. \int d^3\boldsymbol{r}_N \;\Psi^*(\boldsymbol{r}_1,\ldots,\boldsymbol{r}_N)\Psi(\boldsymbol{r}_1,\ldots,\boldsymbol{r}_N) \qquad 3.15$$

The energy functional can be written as:

$$E[n] \;=\; T[n] \;+\; U[n] \;+\; \int V(\boldsymbol{r})n(\boldsymbol{r})d^3\boldsymbol{r} \qquad 3.16$$

Where $T[n]$ and $U[n]$ are the kinetic energy and the electron-electron contribution, respectively, while the last term accounts for the potential energy from the external field due to positively charged nuclei. Kohn-Sham equation can be derived assuming non-interacting system:

$$\left[-\frac{\hbar^2}{2m}\nabla^2 \;+\; V_s(\boldsymbol{r})\right] \psi_i(\boldsymbol{r}) \;=\; \epsilon_i\psi_i(\boldsymbol{r}) \qquad 3.17$$

In 3.17 $\psi_i(\boldsymbol{r})$ are the orbitals. The variational problem of minimizing the energy functional can be solved by applying the Lagrangian method of undetermined multipliers reaching the effective single-particle potential:

$$V_s(\boldsymbol{r}) \;=\; V(\boldsymbol{r}) \;+\; \int \frac{n(\boldsymbol{r}')}{|\boldsymbol{r}-\boldsymbol{r}'|}\, d^3\boldsymbol{r}' \;+\; V_{XC}\,[n(\boldsymbol{r})] \qquad 3.18$$

Where $V(r)$ is the external potential, the second term accounts for electron-electron repulsion and V_{XC} is the exchange-correlation potential. Usually, the starting point is an initial guess for $n(\boldsymbol{r})$, then $V_s(\boldsymbol{r})$ is calculated till solving for the electron density equation. This procedure is then repeated until convergence is reached.

The most important feature of density functional theory is the way in which it directly incorporates exchange and correction effects. One of the most important developments for the practical application of DFT were methods for calculating analytical gradients of the energy with respect to the nuclear coordinates. This enables molecular geometries to be optimized. Comparing DFT method with the HF one a potential problem is that the use of grid-based integration schemes makes it difficult to provide exact expression of the gradients. However, the errors associated with the grid-based method generally is very small and does not cause problems during the optimization procedure.

3.1.3 Determination of Rate Constants

To properly understand the reactivity of a system and to estimate the rate constant for complex reactions where significant rearrangement of molecules is occurs, atoms motion description is required. Internal molecular motion is of complex description, and it is important to understand the spatial evolution in time

of atoms involved in the reactive process. Dealing with a multi-body system the center of mass is assumed to be the reference and the molecular motion can be recognized as external and internal. The former accounts for roto-translational motions while the latter regards vibrations of atoms modelled in first approximation as a set of harmonic oscillators as already discussed.

In this context, microcanonical systems are isolated systems of N particles each one with energy, ε_i. Boltzmann introduced the concept of microstate which is characterized by a well-defined microscopic energetic configuration such as energy distribution among particles. The probability of a generic microstate can be expressed as:

$$\omega_i = \frac{N_i(E)}{\Omega(E)} \qquad 3.19$$

Where $\Omega(E)$ is the total number of microstates.

Microcanonical system mentioned above are usually difficult to be studied as real systems because of the isolation assumption. In general, a system significantly exchanges with the surrounding environment. A macrocanonical system can be represented as a portion of space defined by control surface which exchange energy. The probability of the system of being in a particular energetic state is expressed as a function of its total energy defined as $E_R = \sum_{i=1}^{\infty} N_i \varepsilon_i$ which is the sum for each molecule of the contribution that it is able to store:

$$\omega_s(E_R) = \frac{exp(-\beta E_R)}{\sum exp(-\beta E_R)} \qquad 3.20$$

$$Q_i = \sum exp(-\beta \varepsilon_i) \qquad 3.21$$

$$Z_D = \left(\sum_{i=1}^{N_L} Q_i\right)^N \qquad 3.22$$

$$Z_I = \sum exp(-\beta E_R) \qquad 3.23$$

In equations 3.22 and 3.23 Z is defined as the partition function for both cases of distinguishable and undistinguishable particles. The problem of calculating Z is reduces to that of understanding how a molecule can store energy considering a system of N particles as a function of the energy levels accessible to a molecule N_L. In the scenario of undistinguishable particles for similarity with Z is called partition function too.

From the analysis of internal degrees of freedom of a molecule the possible motions are three: translation, rotation, and vibration. A molecule will thus be able to store energy in the form of kinetic energy (translational motions), inertial rotational energy (rotational motions), and elastic internal energy (vibrational motions). Electronic energy contribution needs to be added as it is associated to electrons and nucleus

interactions but also to intermolecular interactions due to van der Waals forces also known as London interactions.

$$\varepsilon_i = \varepsilon_i^{trasl} + \varepsilon_i^{rot} + \varepsilon_i^{vibr} + \varepsilon_i^{el} \quad 3.24$$

$$Q = \sum exp\left(-\frac{\varepsilon_i}{k_B T}\right) = \sum exp\left(-\frac{\varepsilon_i^{trasl} + \varepsilon_i^{rot} + \varepsilon_i^{vibr} + \varepsilon_i^{el}}{k_B T}\right) = Q_{trasl} Q_{rot} Q_{vibr} Q_{el} \quad 3.25$$

The energy states are obtained by solving the Schrödinger equation. However, for an isolated molecule of ideal gas, the total energy can be regarded as the sum of independent translational, rotational, vibrational, and electronic contributions, whose product will result in the total Q.

$$Q_{trasl} = \left(\frac{2\pi m k_B T}{h^2}\right)^{\frac{3}{2}} \quad 3.26$$

$$Q_{rot} = \frac{8\pi^2 (2\pi k_B T)^{\frac{3}{2}} \sqrt{I_x I_y I_z}}{\sigma h^3} \quad 3.27$$

$$Q_{vibr} = exp\left(-\frac{ZPE}{k_B T}\right) \prod_{i=1}^{3N-6} \frac{1}{1 - exp\left(-\frac{h\nu_i}{k_B T}\right)} \quad 3.28$$

$$Q_{el} = g^{el}\, exp\left(-\frac{E_{el,tot}}{k_B T}\right) \quad 3.29$$

Where $I_x\, I_y\, I_z$ are the principal moments of inertia, σ is the rotational symmetry number, g^{el} is the electronic degeneracy.

Molecular partition functions are estimated thanks to previously mentioned quantum mechanics tools, and they are used to estimate microcanonical rates for chemical reactions according to traditional Transition State Theory (TST) for reactions with barrier or its variational form (VTST) while dealing with barrierless reactions.

The traditional Transition State Theory (TST) is based on two fundamental hypotheses and three restrictive hypothesis that limit the field of applicability.

The two fundamental hypothesis are:

1. The Born-Oppenheimer approximation states that it is possible to treat the motion of electrons and of nuclei independently: during the translation of nuclei, electrons are always in the equilibrium position, in the lowest quantum state. Like in classical mechanics, the nuclei move according to the potential generated by the electronic energy of the reacting molecule. This leaves out quantum

effects such as quantum tunneling, that might be relevant for accurate calculation of rate constants. The adiabatic assumption concerning the lowest quantum state excludes the treatment of spin forbidden reactions, involving an intersystem crossing (e.g. jump from a singlet to a triplet potential energy surface as in singlet-to-triplet reactions).

2. The velocity distribution of molecules is defined by the Maxwell-Boltzmann distribution function.

The three restrictive hypotheses are:

- Non-recrossing hypothesis, i.e., once the reactants overcome the transition state (TS) configuration they can only proceed to products, without the possibility of moving back to previous configurations.
- In the region around the TS, δ, the motion of the system can be treated as a pure translation.
- TS is in equilibrium with the reactants.

The final expression for the kinetic constant can be expressed as:

$$k_{TST} = \frac{k_B T}{h} \frac{Q_{\neq}^{trasl} Q_{\neq}^{rot} Q_{\neq}^{vibr} g_{\neq}^{el}}{Q_R^{trasl} Q_R^{rot} Q_R^{vibr} g_R^{el}} exp\left(-\frac{E_A}{k_B T}\right) \quad 3.30$$

Where $\neq$ stands for transition state while R for reactants.

The activation energy is:

$$E_A = \left(E_{el,tot} + ZPE\right)_{\neq} - \left(E_{el,tot} + ZPE\right)_R \quad 3.31$$

The corresponding PES presents, at the maximum energy state, a transition state configuration named as tight transition state, as reported in Figure 3.1.

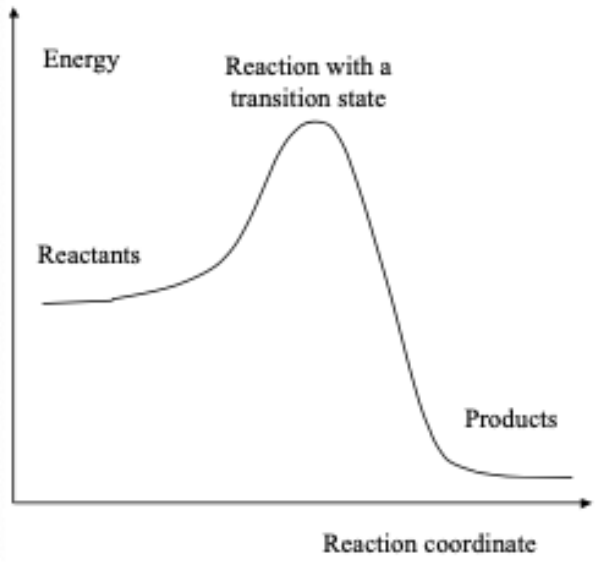

Figure 3.1: Potential Energy Surface for reactions with barrier.

In the transition state theory, the change of geometrical conformation is accounted for and described along the reaction coordinate, taking care of internal motions passing from reactant to product configuration. It is worth mentioning that in Figure 3.1 the y-axis reports the energy as the sum of electronic energy and zero-point energy (ZPE) till reaching a maximum. Concerning this reaction class, TST can be used for rate constant computation. At the transition state, one of the internal motion degenerates from vibrational to a translational motion. This is consistent with the fact that, treating the motion along the reaction coordinate as a vibration, any deviation from equilibrium position would involve a decrease in the energy of the system leading to imaginary vibration frequencies according to the harmonic oscillator approximation.

However, traditional TST is not suitable for barrierless reactions which are treated with the variational form (VTST). In barrierless reactions the configuration of the TS would coincide with that of the products, as they correspond to the maximum energy, according to what is called a "tight" TS. In this case, the non-recrossing assumption used in TST formulation breaks down and k_{TST} is overestimated. To overcome this issue the rate constants is computed along the Minimum Energy Path (MEP) on the Potential Energy Surface (PES), and its lower values is taken as the upper limit of the real rate constant. In VTST, the reactive flux is taken as the bottleneck for the reaction.

The bond length has been progressively increased starting from that of the dimer where the parent monomers are sticked till reaching complete separation. Transition states have been located by means of PES scan along the bond coordinate at the same level of theory before implemented. As barrierless reaction, the transition state search procedure does not give any results and no imaginary frequency was present. By using traditional unrestricted DFT methods [77], when increasing progressively the bond length as internal coordinate, simulations do not provide the correct value for the energy gap between the dimer and the monomers separated at a fixed distance. Therefore, some corrections as the broken symmetry approach must be accounted for to properly predict the PES, as discussed in the following. The bond length has been progressively frozen, and simulations have been run taking account of a beta-scission reaction from the dimer till dissociation in two monomers.

$$E_{TS} = \left[E_{PR1\_hl} + E_{PR2\_hl}\right] + \left[E_{distXY\_hl} - E_{dist10.0\_hl}\right] + \left[ZPE_{PR1\_hl} + ZPE_{PR2\_hl} + ZPE_{dist10.0\_hl}\right] \quad 3.32$$

$$E_{MEP\_disXY} = \left[E_{TS} + ZPE_{TS}\right] - \left[E_{PR1\_hl} + E_{PR2\_hl} + ZPE_{PR1\_hl} + ZPE_{PR2\_hl}\right] \quad 3.33$$

For each point on the PES, the energy computed for the corresponding transition state is computed with the corrections provided in 3.32 and 3.33, where distXY stands for the increasing bond length till 10 A.

All those values refer to level 0 and level 1 calculations for each transition state and then to high level calculations using DFT methods in the unrestricted form to better account for orbitals interactions. The broken symmetry approach has been adopted as a compromise where multireference calculation cannot be implemented because of a too high computational cost with such large molecules [77]. Broken symmetry states are very interesting from a computational point of view as they are designed to construct the electronic density of the system, which is the real quality with physical meaning at the heart of DFT, as the square of a Slater determinant (N-electrons) [83].

According to VTST, the "S-shape" PES profile corresponds to a rate constant curve along the reaction coordinate, i.e., the distance between the parent monomers, which reaches a minimum in proximity of the minimum flux of reactant molecules that passing through a specific portion of the PES as schematized in Figure 3.2. The Minimum Energy Path can be described as the union of steepest paths from the saddle point to the minima, it is located in correspondence of any point on the path which is at an energy minimum in all directions perpendicular to the path.

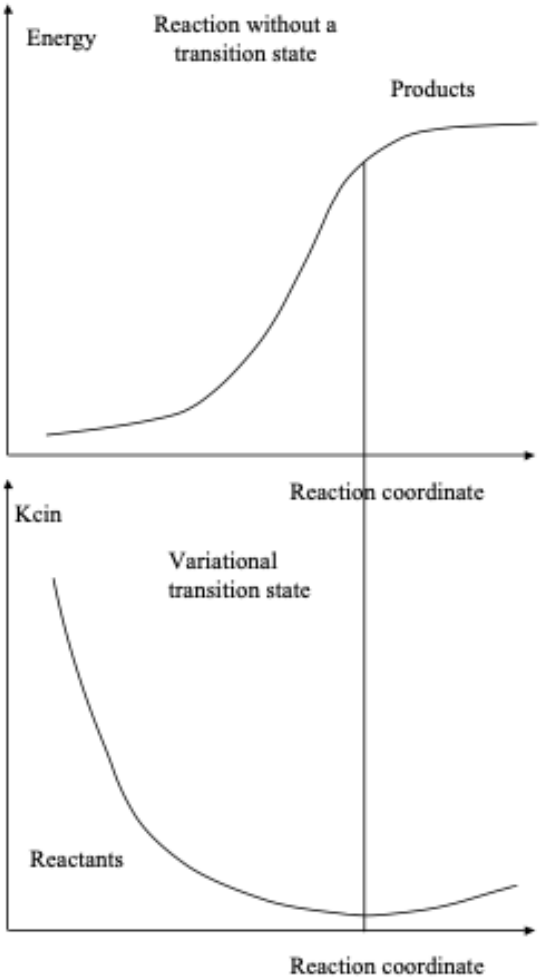

Figure 3.2: Potential Energy Surface (PES) and Rate Constant along the reaction coordinate for barrierless reaction.

In this work VTST is used to simulate scission reactions. TS was searched by performing a scan on the reaction coordinate, and the geometry with highest energy was used as first guess for subsequent optimization, as discussed in Chapter 4.

3.1.4 Master Equation

As already mentioned, both traditional and variational Transition State Theories assume that the reacting system is in equilibrium with the surrounding environment at fixed T and P. The resulting rate constant has no dependence on pressure, and this leads to an overestimation of the k value under conditions far from the high-pressure limit. The reactant molecule of a uni-molecular reaction acquires energy from intermolecular collision to overcome the barrier, such that the translational energy of the colliding body is transferred to the reactant in the form of vibrational contribution. The colliding body is also called third body and it can be a reactant, a product, or an inert and it involves the pressure dependance. Hence, at low P also k decreases due to poor energy transfer to the reactants. This phenomenon is called "fall-off regime" as named by Lindemann in 1922.

Lindemann theory is not accurate in intermediate pressure regions because it does not account for energy redistribution among different energy states upon a collision. To do so a microcanonical representation of the system is requires such as the RRKM-ME theory which estimates the kinetic constant together with the determination of the population balance of each energy level to determine the reactive behavior.

$$k(E) = \int_{E_A}^{E} \frac{\upsilon(E^*)}{2\delta} P(E^*) dE^* \qquad 3.34$$

$$P(E^*) = \frac{\rho^{vibr}(E - E^*)\rho^{trasl}(E^*)}{\rho^{vibr}(E)} \qquad 3.35$$

In equations 3.34 and 3.35 $\upsilon(E^*)$ is the velocity in terms of kinetic energy E^*, $P(E^*)$ is the probability of the state with energy E^* and $\rho(E)$ indicates the number of ways the energy is able to redistribute among molecule motions. However, the actual population of an excited level with energy E is unknown. To fill this gap, it is necessary to solve a population balance known as "Master Equation" (ME).

Master Equation is used to describe the time evolution of a system that can be modelled as a probabilistic combination of states at any given time and the switching between states is determined by a transition rate matrix. Equations involved are differentials over time of the probability that the system occupies each of the different states. Chemical Master Equation govern the evolution of the probability distribution of configurations of a reaction network. Crucially, this family of models accounts for stochasticity inherent in reaction processes that play functional roles in chemical processes [84].

The problem from now on has a probabilistic connotation and the population balance can be written:

$$\frac{dn(E)}{dt} = Z \sum_{E^I=0}^{\infty} \left(P(E,E^I)n(E^I) - P(E,E^I)n(E)\right) - k(E)n(E) \qquad 3.36$$

In 3.36 $n(E)$ represents the population of the energy level E while $P(E,E^I)$ is the probability for a molecule to move from an energy state E^I to E after a collision. Z is the number of collisions per unit of time and volume, $k(E)$ the kinetic constant of the reaction corresponding to energy E.

The probability of an energy jump can be normalized to 1 between 0 and ∞ with different models as the exponential down model, the gaussian model, the double exponential down model and the asymmetrical exponential model which are the most widely implemented. The probabilities of transition are linked by thermodynamic consistency as $f(E^I)P(E,E^I) = f(E)P(E,E^I)$.

According to rotational and transitional partition functions simplification the distribution function $f(E)$ can be written:

$$f(E) = \frac{\rho(E)}{Q} exp\left(-\frac{E}{k_B T}\right) \qquad 3.37$$

Equation 3.37 is named distribution function of the vibrational energy of Boltzmann. The partition function can be expressed as:

$$Q = \int \rho(E)\ exp\left(-\frac{E}{k_B T}\right) dE \qquad 3.38$$

$$k|_{T,P} = \sum_{E_A}^{E_{max}} n(E)k(E) \qquad 3.39$$

The resulting problem is a complex integral-differential equation as in 3.39 and the final rate constant is expressed as a function of T and P.

3.2 Computational Environment and Numerical Simulations

In this thesis all the calculations performed to predict the electronic structure of reacting molecules and the treatments of chemical kinetics are carried out using EStokTP framework [42] [41], which decomposes the problem in subsequent steps as reported in Figure 3.3. The EStokTP computational environment is designed to directly couple the electronic structure, Transition State Theory (TST) and Master Equation (ME) evaluations to automatically obtain a priori predictions of the temperature and pressure dependent rate constants. Providing molecular structures as input the main purpose is the prediction of rate constants for

some classes of reactions. EStokTP allows to perform electronic structure optimization and master equation calculations, but it can be also useful also to investigate complicated Potential Energy Surfaces (PES).

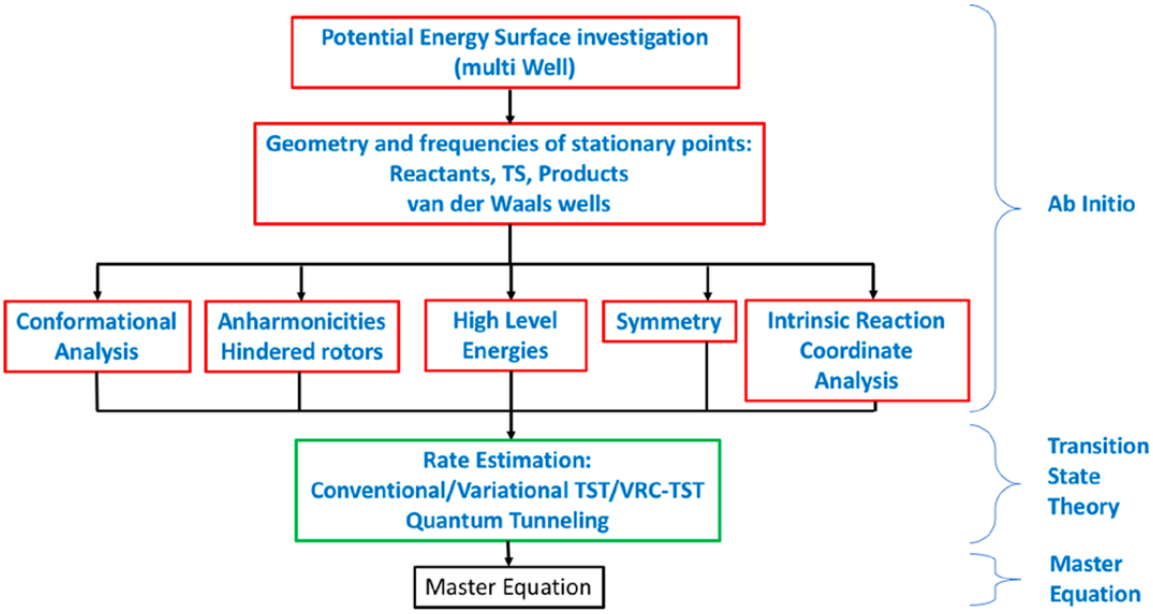

Figure 3.3: Computational steps required for an automatic implemented protocol to compute rate constants for an arbitrary chemical reaction [42].

In general, the prediction of rate constants involves two steps, with the first consisting of a set of electronic structure calculations and the second in the application of some form of kinetic solver, such as the traditional TST or the variational form, which is the one effectively adopted in the present work for barrierless reactions.

EStokTP provides a fully integrated treatment of both steps through calls to external codes to perform first electronic and then ME calculations [43]. The code implements one or multidimensional hindered rotor treatments based on intrinsic reaction coordinate. The Ab Initio Transition State Theory-based Master Equation (AITSTME) approach in here used and it performs calculations in three different steps:

- Molecular properties for stationary points on the PES such as reactants, products and, if present, transition state by ab initio (AI) calculations.
- Microcanonical rates for chemical reaction are, then obtained.
- Phenomenological rate constants are reached with ME solver codes with microcanonical rate constants and intermolecular energy transfer rates.

However, for high accuracy predictions, some additional features need to be considered such as hindered rotor corrections, variational effects, and tunneling contributions. Gaussian09 [78] is the software used for advanced calculations such as energies prediction, molecular structures optimization and spectroscopic data.

Computational quantum mechanical modeling methods are used to perform electronic structure calculation as listed above. In this thesis those calculations are performed using M06 method [85] which is a global hybrid functional between HF and DFT.

As already mentioned, Hartree-Fock theory has some limitations related to the absence of electron correlations: the energy contributions arising from electrons interacting with one another [86]. Additional results are presented for B3LYP and B97D density functionals.

Most methods require a basis set to represent a set of functions (called basis functions) that are used to represent the electronic wave function of HF method or in the DFT one to turn partial differential equations into algebraic equations suitable for efficient computer implementation. The basis set can be composed of atomic orbitals, plane waves or real-space approaches. Within the basis set, the wavefunction is presented as a vector, the components of which correspond to coefficients of the basis functions in linear expansion. The smallest basis sets are called minimal basis sets in which a single basis function is used for each orbital in HF calculation. If additional functions are used to describe polarization of electron density, they are called polarization functions. Another common addition to basis sets is the addition of diffuse functions to give flexibility to atom orbitals far away from the nucleus. In this work different basis set have been exploited such as 6-311+G(d,p) which is a Pople basis set accounting for polarization and diffuse functions, and cc-pVTZ as a correlations-consistent basis set to include successively larger shell polarization.

Ab initio electronic structure calculation have been performed using DFT on Gaussian09. Simulations at level 0 and level 1, in this work, have been performed for recombination reaction with the M062X functional and the 6–311+G(d,p) basis set to reach geometry optimization and frequency calculation. The M062X functional has been selected as it is suitable to describe chemical kinetics with reasonable accuracy.

Chapter 4 – PAHs Reactivity

As mentioned in Chapter 2, PAH dimerization reactions play an important role in soot formation. Monomers interact and cluster together to form incipient soot starting from flat and curved PAHs. Density Functional Theory has been exploited in this work to explore cross-link reactions between PAHs of various reactive edge types, knowing that previous studies have proved that physical interactions are not sufficient to describe nucleation flux and chemical contribution need to be considered [47].

4.1 Dimerization Reactions

In this work three classes of PAHs have been considered as monomers, i.e., σ-radicals and π-radicals considering both scenario of localized and delocalized radicals, which are of interest because of their propensity to dimerize, owing to their high concentration in high T combustion environments. They exploit different reactive edges in different position and with different radical delocalization character. The geometries considered in this study are the same as those investigated by Menon et al. [76] and previously mentioned in Section 2.5. In Figure 4.1 all the considered monomers are reported and following the grid layout cross-linking reactions and corresponding products are listed.

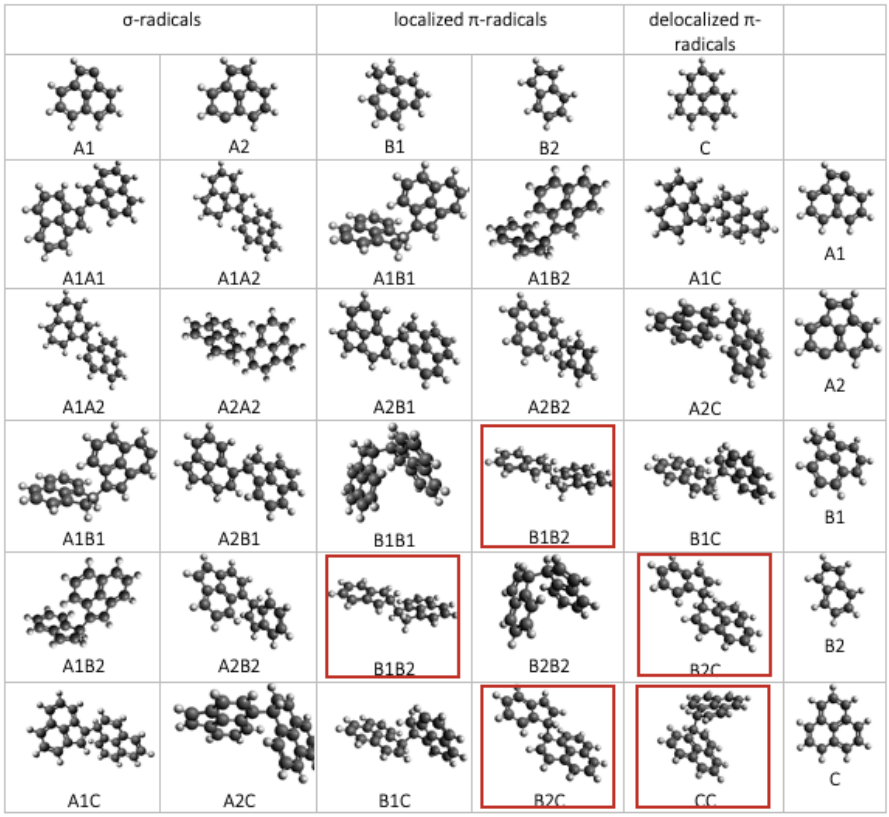

Figure 4.1: Reactants and products of cross-linking reactions for different PAH types.

The entire set of monomers and dimers has been investigated with EStokTP. Geometry optimization and electronic energy computation have been carried out to compute bond energies. However, some preliminary considerations are required regarding the structures involve in the study.

Indenyl structures in Figure 4.2 have been optimized with ab initio electronic structure calculation using DFT in Gaussian09. Simulations at level 0 and level 1 have been performed for recombination reaction with the M062X functional and the 6–311+G(d,p) basis set to reach geometry optimization and frequency calculation with the aim to compare radicals stability. The M062X functional has been selected as it is suitable to describe chemical kinetics with reasonable accuracy. Case a) reaches a lower energy state which means a more stable configuration leading to a dominant radical structure on that site with respects to case b). However, the radical is still localized on both β-positions indiscriminately which guarantee delocalization driven by the aromaticity on the six membered ring providing higher stability.

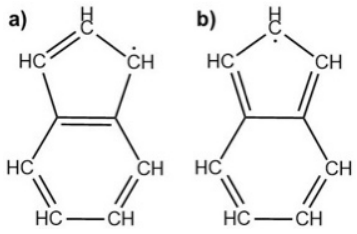

Figure 4.2: Indenyl Resonance Structures.

Previous work from Menon et al. [76] provides a kinetic study on the monomers mentioned above while dealing with PAH recombination reactions participating to PAHs growth. As shown in Figure 4.1, the reactive edges have been described and grouped. In the work of Menon et al. [77] the M06-2X functional has been adopted for molecular optimization along with energies and thermodynamic properties investigation. Single-point energy calculations have been performed to refine previous values with M062X/cc-pVTZ. Coupling together reactants and products, recombination energies, corresponding the bond dissociation energies, have been computed. In the following section the same procedure has been reproduced dealing with different methods and functionals to compare the expected level of accuracy.

The full set of monomers has been considered and the entire class of products from recombination reactions has been investigated from an energetical point of view as preliminary calculations. Then, as a second step, the kinetic analysis with rate constants estimation has been carried out.

Figure 4.1 presents a complete overview of the dimerization reactions that will be assumed as reference for additional considerations. The aim of this study is to find out correlation between smaller PAHs reactions and larger ones to formulate rate rules hypotheses while sequentially adding an aromatic ring. In general, two different classes of reactions can be identified in a radical chain reactive systems, i.e., reactions with and without an energy barrier. Dimers highlighted in red in Figure 4.1 correspond to B1B2, CC and B2C cross-

linking, which are reactions with a barrier. In this case a transition state for the reaction can be easily located. Conversely, all the other dimerization reactions considered in this work are barrierless. In barrierless reactions a common feature is present, the dimer is much more stable than the two monomers together.

The first step of the workflow is the computation of the Bond Dissociation Energy (BDE) or the energy of recombination reactions, respectively considering scission or addition mechanism both implemented in EStokTP routines. Starting from five monomers, twelve reactions are analyzed and classified as barrierless. Reactions among the monomers of different radical type, as reported in Figure 4.1, are accounted for.

As briefly mentioned above some cross-linking reactions result as barrierless but some of them features a transition state, i.e., a not null energy barrier.

4.2 Results

The work of Menon et al. [76] has been taken as the reference for the kinetic study here presented. Additional simulations have been carried out to define the most suitable functional methods to be used when dealing with large aromatic structures, providing quantitative comparison with other literature results. In the following paragraph PES and rate constants calculations are discussed for reaction classes with and without an energy barrier involving chemically sticking PAH. Barrierless reactions require a quite more complex procedure not just for the rate constants computation through VTST, but also in dealing with the construction of a proper PES.

Following the analysis of Martin et al. [52], additional considerations are here reported regarding electronic structure calculations for larger PAHs and subsequent rate rules development. Starting from selected radical PAH monomers which primarily populate the flame environment, their structures have been progressively enlarged and optimized with the addition of one to three aromatic rings and the BDE of the related dimers has been compared to the ones of smaller aromatic structures. The same strategy has been adopted for the rate constants computation.

Radical-radical reactions, as mentioned above, require multi-reference methods to be accurately modeled. However, considering the large size (> 15 C-atoms) of the large aromatic structures investigated in this work, such methods are too expensive computationally to reach numerical solution at a reasonable computational cost. This is also related to the fact that very large active spaces should be considered to properly characterize the phenomena. Therefore, to overcome this issue, different strategies have been adopted as discussed in the following.

4.2.1 Barrierless Reactions

Barrierless reactions analysis starts from reactants and products optimization to estimate the Bond Dissociation Energy (BDE) and to define the related potential energy surfaces. The results obtained by Menon et al. [76] come from broken symmetry calculations with the unrestricted M06-2X functional. According to their analysis the broken symmetry approach allows a good estimation of the energy for the points on the PES. Energy calculations have been performed with M06-2X, as reported in Table 4.1, with good agreement with the results abstained in [76].

Conversely, PES calculation without the broken symmetry approach led to inaccurate prediction of long-range interactions, using restricted M06-2X functional the reference value at 10 Å does not provide reasonable results, with large overestimation (~80 kcal/mol) of the expected plateau value of the PES [76]. Restricted M06-2X works quite well only up to ~ 3.8 Å, where the distance between the dissociating monomers is low and reciprocal interactions are well described by the functional. However, when increasing the C – C distance, a divergent solution is found as reported in

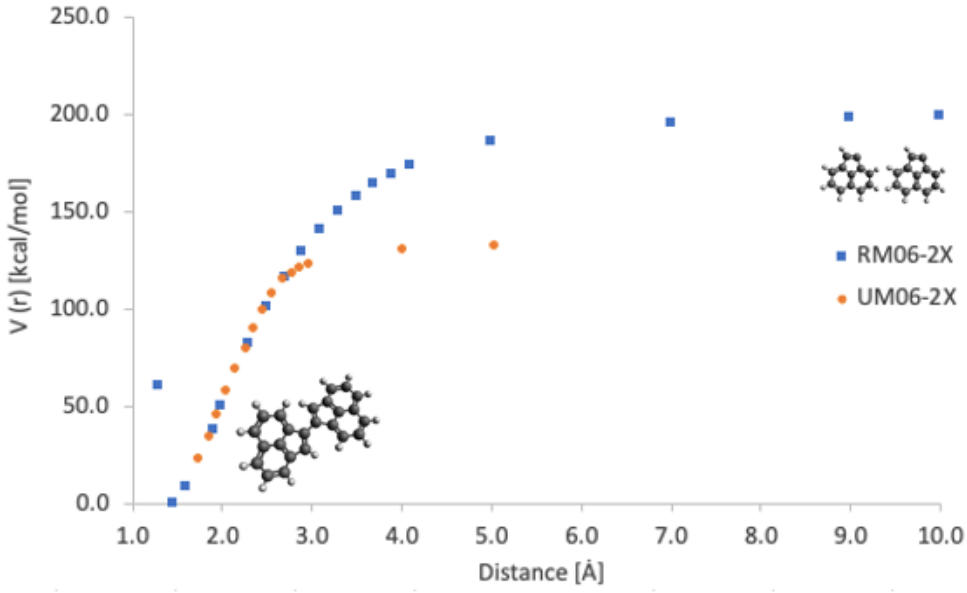

Figure 4.3. Therefore, the unrestricted M06-2X has been adopted. Hybrid functionals such as M06-2X perform better than pure DFT functionals in BS-DFT calculations because the former reduces the self-interaction error of the DFT exchange functionals, which mimics unspecified static electron correlation effects, so that the inclusion of specific static electron correlation effects via the form of the wave function becomes more effective [87].

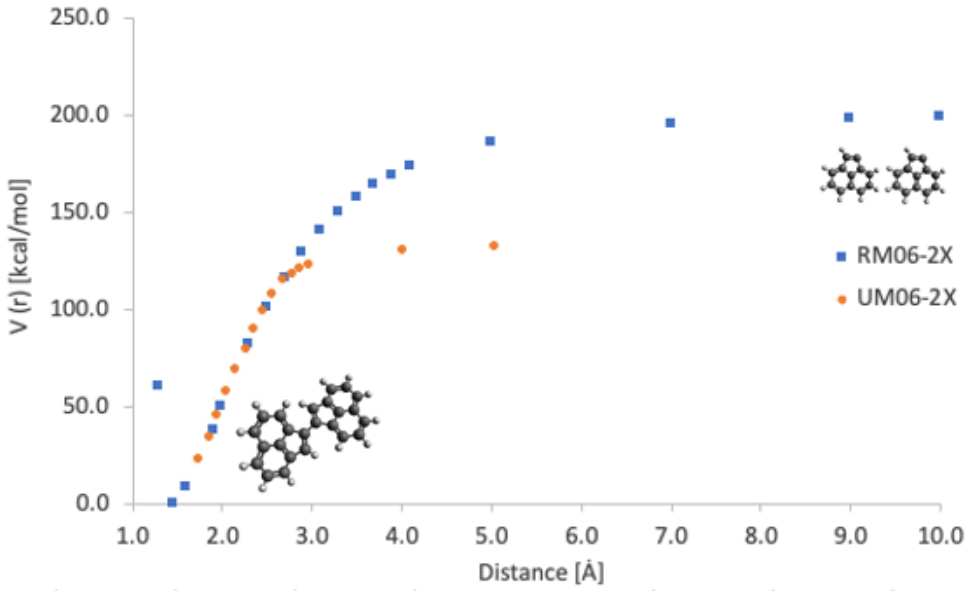

Figure 4.3: PES reproduction with RM06-2X (blue) and UM06-2X (orange).

The inaccuracy of restricted functionals calculations is shown in

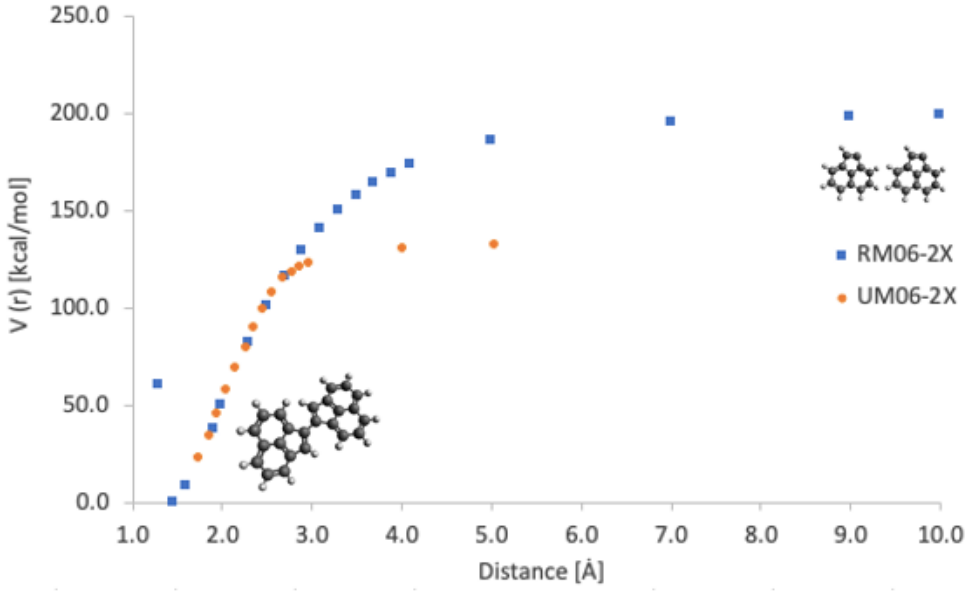

Figure 4.3 where a comparison between UM062-2X/cc-pVTZ results from Menon et al. and RM062-2X/cc-pVTZ is reported. In

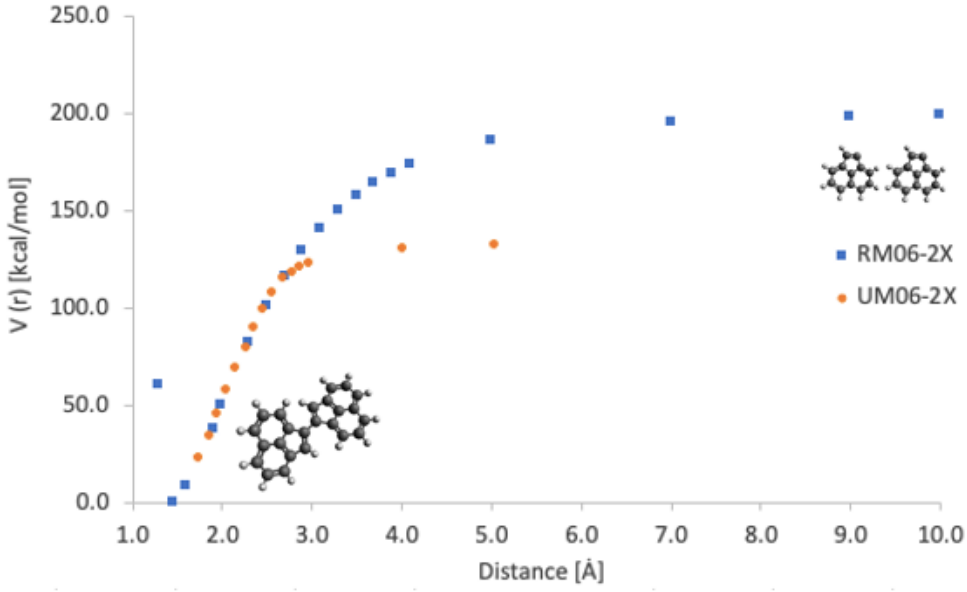

Figure 4.3 the self-recombination reaction between A1 monomers is reported as an example. In proximity of ~ 3.0 Å the last accurate point is located. Progressively enlarging the distance, it is possible to clearly see the divergent behavior. The unrestricted functional is not able to accurately describe open shell singlet behavior as represented by the asymptotical trend of the curve. DFT methods are not able to account for Coulomb interactions which are significantly relevant when complete dimers dissociation is reached [88].

Together with M06-2X, simulations with other functionals have been carried out to estimate the level of accuracy for bond energy evaluation. Every comparison and comment related to functionals accuracy have been done referring to biphenyl recombination energy assumed as a benchmark (117.6 kcal/mol) [89], as discussed later.

Reactions	Bond Energies [kcal/mol] *(Menon et al.)*	Bond Energies [kcal/mol] *(this work)*	Δ [kcal/mol]
A1 + A1 → A1A1	130.40	126.96	3.44
A1 + A2 → A1A2	125.30	121.65	3.65
A1 + B1 → A1B1	97.30	93.51	3.79
A1 + B2 → A1B2	91.00	87.57	3.43
A1 + C → A1C	73.60	69.26	4.34
A2 + A2 → A2A2	120.80	117.27	3.53
A2 + B1 → A2B1	92.60	87.42	5.18
A2 + B2 → A2B2	86.80	82.35	4.45
A2 + C → A2C	69.00	65.93	3.07
B1 + B1 → B1B1	61.90	61.95	-0.05
B1 + C → B1C	39.90	39.42	0.48
B2 + B2 → B2B2	50.90	49.12	1.78

Table 4.1: Bond Recombination Energies computed from Menon et al. with M06-2X/cc-pVTZ (left) and from this work with M06-2X/6-311+G(d,p) (right).

In Table 4.1 bond recombination energies for barrierless reaction from this work are compared to values from Menon et al. In the column on the right the deviation between these results is reported. The main difference between the results in these two columns is linked to the procedure adopted to refine calculations. Indeed, Menon et al. used single point energy calculations, while in this work the hindered rotor scan on twelve geometries has been performed with the same method and basis set implemented at level 0 and level 1 (respectively M06-2X/6-31+G(d,p) and M06-2X/6-311+G(d,p)). An additional difference lies in the basis set selection, i.e., cc-pVTZ vs 6-311+G(d,p), even if they do not strongly impact the accuracy of the results obtained. Ultimately, the refining procedure causes the main change leading to a mean deviation error of ~ 3 kcal/mol which is reasonably low and in the range of the relative uncertainties of the adopted methods.

As already mentioned, in this work a specific refining procedure has been applied by performing 1-D hindered rotor scan with M06-2X/6–311+G(d,p) on twelve geometries after a primary identification of the dihedral angle for each dimer which rotates generating a more accurate first guess for level 1 calculations. The one-dimensional (1-D) hindered rotor model is often used for quantum mechanical treatment of internal rotation. At level 0 of theory a preliminary scan of six geometries has been carried out to identify the first guess for level 1 calculations, after that the refining procedure has been performed with twelve progressive rotations each of them separated by a smaller rotation-interval. This procedure is well consolidated to provide good results for similar classes of molecules involving a dihedral angle which gives reciprocal rotation of the monomers involved and cross-linked. This last-mentioned monomer characteristic suggest that the biphenyl benchmark can be coherent with PAHs dimers nature and features as adopted in the work by Menon et al.

According to the work Menon et al. [76] single-point energy calculation can be performed to increase the accuracy and to refine calculations. High level calculations have been carried out by using same functional as for level 0 and level 1 but with a different basis such as cc-pVTZ which reduced the mean deviation till 2.30 kcal/mol. The implementation of cc-pVTZ basis set allows to reach a more accurate modelling of the interaction energy. The cc-pVTZ basis set is a much larger one, involving more functions per atom than 6-311+G(d,p) and longer computation time, the larger the basis set for a given functional the lower the variational energy. However, the implemented calculation adopting M06-2X/6–311+G(d,p) seems to be quite accurate, reaching geometry optimization and a reasonable small error for BDE computation. As shown in Table 4.1 the utilization of DFT impacts on energies computation even if the reported inaccuracy, with respect to the results of Menon et al., does not influence the current work being the energy gap reasonably low and in the rage of tolerance of ± 5 kcal/mol as expected while changing method and basis set. What it is relevant in this work is the robustness showed by the adopted DFT methods despite of providing a complete overlapping with previous results. The energy gap computed in the last column (Table 4.1) is always coherent

with the DFT implemented and for analogy all the successive results are expected to be scaled according to the energy discrepancy.

To better understand the reasons of the choice of functionals for both level 0 and level 1 some additional simulations have been carried out changing both method and basis set. Some considerations can be done taking biphenyl as a reference structure.

B3LYP was the first functional adopted (see Table 4.2) which underestimate bond energies leading to a much larger mean deviation of 19.32 kcal/mol. B3LYP is the first hybrid method developed, it is generally faster than most post Hartree-Fock techniques and usually yields comparable results. It is also a robust DFT method and generally it is considered a standard choice for large molecules such as aromatic hydrocarbons, as it is less expensive than higher levels of theory [86]. On a more fundamental level, it is not heavily parametrized as other hybrid functionals. B3LYP is commonly adopted together with empirical dispersion, which incorporates a correction for long-range van der Waals interactions reaching more accurate results leading to a smaller error. This last statement is confirmed by the comparison with biphenyl recombination energy which result as 112.6 kcal/mol instead of 117.6 kcal/mol, assumed as the benchmark value [89], proving a margin of just 4 kcal/mol which can be considered reasonable while dealing with ab initio calculations.

Reactions	Bond Energies [kcal/mol] *(Menon et al.)*	Bond Energies [kcal/mol] *(this work)*	Δ [kcal/mol]
A2 + C → A2C	-69.00	-51.09	-17.91
B1 + B1 → B1B1	-61.90	-43.67	-18.23
B1 + C → B1C	-39.90	-21.04	-18.86
B2 + B2 → B2B2	-50.90	-28.63	-22.27

Table 4.2: Bond Recombination Energies computed from Menon et al. with M06-2X/cc-pVTZ (left) and from this work with B3LYP/6-311+G(d,p) (right).

The second method adopted as comparison has been B97D, as reported in Table 4.3, hybrid density which in the dispersion corrected form is known to perform well for geometries and electrostatics describing the dipole moment for aromatic complexes [85]. The B97D/cc-pVTZ level of theory has been adopted in order to ensure minimal basis set superposition errors but it still leads to a deviation of 15.11 kcal/mol. B97D functional for these classes of molecules and corresponding reaction is not accurate even running single-point energy calculation to refine level 1. The bond dissociation energies were calculated from a homolytic bond cleavage using high level energies calculations too including dispersion but M06-2X still provides better results thanks to a better description of HOMO-LUMO gap due to the Fock exchange accounted in those functionals.

Reactions	Bond Energies [kcal/mol] *(Menon et al.)*	Bond Energies [kcal/mol] *(this work)*	Δ [kcal/mol]
A2 + C → A2C	-69.00	-54.50	-14.50

B1 + B1 → B1B1	-61.90	-46.80	-15.10
B1 + C → B1C	-39.90	-24.34	-15.56
B2 + B2 → B2B2	-50.90	-35.64	-15.26

Table 4.3: Bond Recombination Energies computed from Menon et al. with M06-2X/cc-pVTZ (left) and from this work with B97D/cc-pVTZ (right).

As mentioned above the biphenyl C—C bond has a value of 117.6 kcal/mol, with the implementation of previously adopted methodologies some different results have been gained. B3LYP gives an energy gap of 122.66 kcal/mol while M06-2X a more accurate one of 115.38 kcal/mol and B97D of 108.30 kcal/mol, in all case studies dispersion has been included to account for additional interactions. These values confirmed that the assumption of M06-2X as the reference functional for all the calculations listed in this thesis could be considered acceptable while B97D the less accurate for these classes of structures. Without taking account of high-level calculations and dispersion even worst resulted are reached. Therefore, these values should be viewed within this error to provide a comparative look at the reactivity of the different edge sites. In general, the M06 family of density functionals has been assessed for its performance in predicting experimental values with impressive accuracy.

PES scan for barrierless reaction is a challenging reconstruction, as discussed above. The computation of the fictitious transition state energy is calculated for each distance from 1.45 Å (bond length of the dimers) to 5.0 Å (complete dissociation and negligible interactions) with a step of 0.2 Å at the beginning refined with a step of 0.1 Å when necessary to better understand the behavior of the curve. The energy value at 10 Å is needed as reference state. Increasing the bond length till 10 Å and freezing it step-by-step PES has been progressively reconstructed. From 4.3 Å on till reaching 10 Å correlation energy is not negligible and the restricted functional cannot ensure geometry optimization which is important as reference for the limit of reciprocal interactions. Unrestricted DFT performs well for large molecules to simulate ground and excited state calculations.
In Figure 4.4 Menon et al. [76] PES have been reported for the involved barrierless reactions which have been computed with M06-2X/cc-pVTZ as functionals and the comparison with 6-311+G(d,p) basis set has been provided.

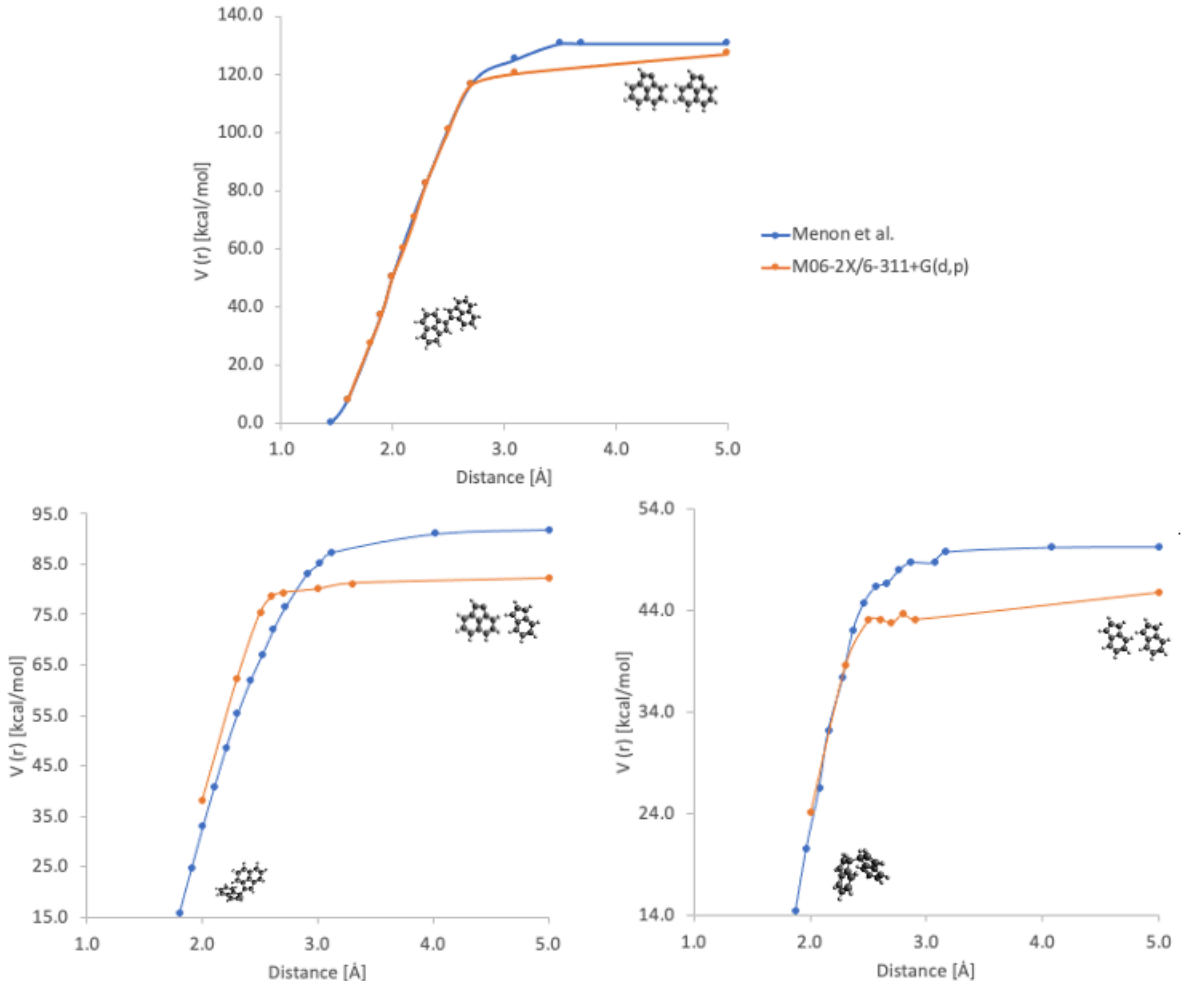

Figure 4.4: Potential Energy Surfaces comparison for Reaction with Barriers from Menon et al. with M06-2X/cc-pVTZ and from this work with M06-2X/6-311+G(d,p).

Orange profiles, which have been derived with M06-2X/6-311+G(d,p), present some disagreements in correspondence distance between 2.7 Å and 3.5 Å close to the plateau. It is necessary to refine calculations being these points fundamental for the computation of the rate constants as the minimum is located in this range. The problem in the underestimation of these energy values comes from wrong frequency calculation for the transition state if the hindered rotor scan is not considered.

In Figure 4.4 just three barrierless reactions have been reported as reference for the upper and the lower reactivity limit.

4.2.2 Reactions with Barriers

Reactions with barriers are just few of the total class of dimerization listed in the previous paragraph. As reported in Figure 4.1, the dimers which are characterized by recombination with an energy barrier are three and more precisely the so called B1B2, B2C and CC. Bond recombination energies have been computed as for barrierless reactions with M06-2X/6-311+G(d,p) and in Table 4.4 and Table 4.5 a comparison with the M06-2X/cc-pVTZ functional used by Menon et al. has been reported [76]. Being a much simpler class of reactions

computational effort to provide concrete and reliable results is much lower and so less trials have been carried out. Energy barriers calculations come from reactants, products and transition states simulations which are located at the maximum energy peak on the PES.

Reactions	Bond Energies [kcal/mol] *(Menon et al.)*	Bond Energies [kcal/mol] *(this work)*	Δ [kcal/mol]
B1 + B2 → B1B2	34.00	30.78	3.22
B2 + C → B2C	33.40	32.97	0.43
C + C → CC	17.00	16.89	0.11

Table 4.4: Recombination Energies for Reaction with Barrier computed from Menon et al. with M06-2X/cc-pVTZ (left) and from this work with M06-2X/6-311+G(d,p) (right).

Reactions	Energy Barriers [kcal/mol] *(Menon et al.)*	Energy Barriers [kcal/mol] *(this work)*	Δ [kcal/mol]
B1 + B2 → B1B2	4.10	0.76	3.34
B2 + C → B2C	2.50	0.24	2.26
C + C → CC	9.90	3.94	5.96

Table 4.5: Energy Barrier computed from Menon et al. with M06-2X/cc-pVTZ (left) and from this work with M06-2X/6-311+G(d,p) (right).

Recombination reactions selected for this study involve previously mentioned monomers which are the most abundant in flame environment because of their stabilization by resonance such as B1 and B2, also monomer C has been considered which is characterized by a more delocalized electron density. These considered reactions lead to reasonably high energy barriers not being submersed by functional change sensibility. However, some other high barrier-low enthalpy reactions include both B1 and B2 involving five-membered ring carbon in bond formation but providing a much higher barrier. This would suggest that bonds between five-membered rings are likely less favorable unless there is sufficient radical character among the reacting PAHs. Counter wise, when the barrier is low the bonds formed are easier to be formed but weaker.

As reported in Figure 4.5 changing the basis set some deviations are highlighted, according to the orange line there is an underestimation of the values reported in the work by Menon et al. [76]. The cc-pVTZ basis set results as more accurate to account for reciprocal interactions between radical molecules, while 6-311+G(d,p) is less expansive from a computational point of view and the calculation time is much lower. Considering computational costs advantages in the adoption of a smaller basis-set and relatively small deviation reported in the plots also the implementation of M06-2X/6+G(d,p) can be quite reasonable in term of accuracy. The same couple of methods have been adopted to carried out biphenyl simulations assumed as benchmark which reports a deviation of approximatively 2.4 kcal/mol as a confirmation of the consistency of the schematized results.

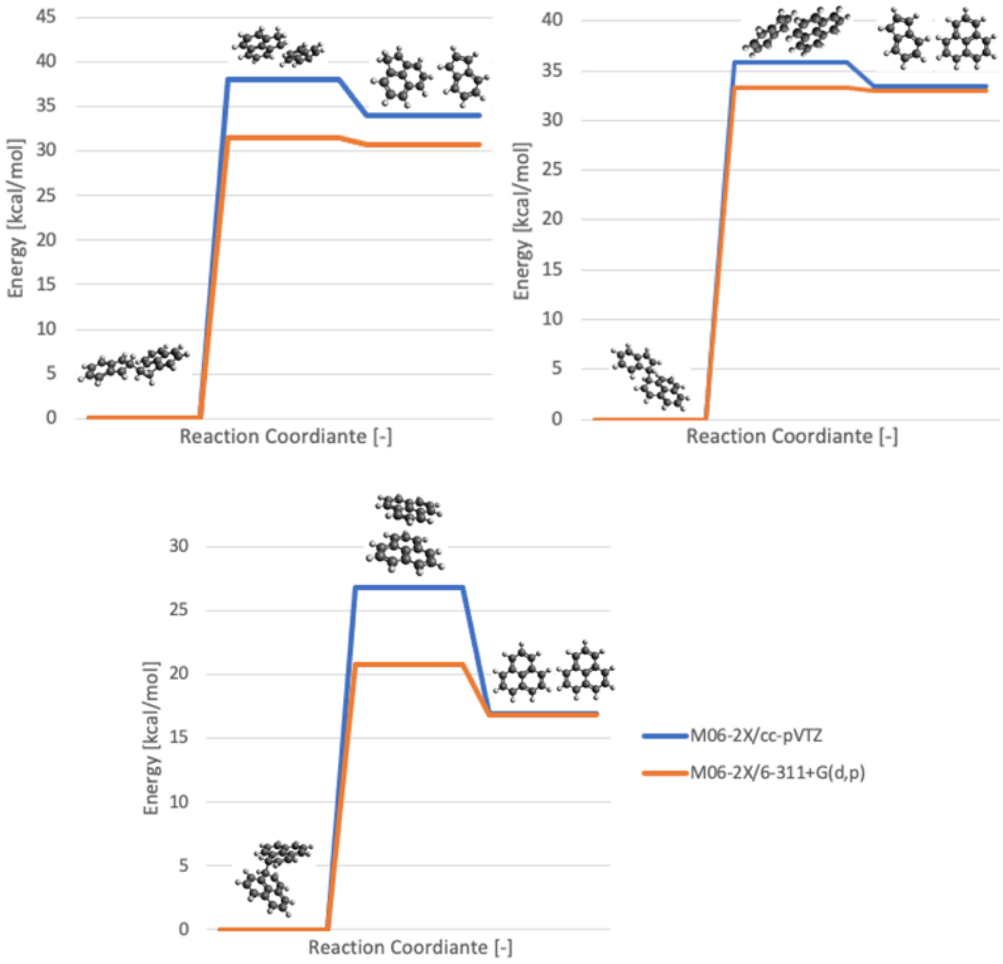

Figure 4.5: Potential Energy Surfaces comparison for Reaction with Barriers from Menon et al. with M06-2X/cc-pVTZ and from this work with M06-2X/6-311+G(d,p).

According to Figure 4.5, in the PES regarding reactions with barrier some disagreements are reported referring to the error between the two methods, the enthalpy of reaction values seem to be generally well predicted indeed the activation energy values appear underestimated by M06-2X/6-311+G(d,p) with respect to the results reported by Menon et al. [76] which refer to single point energy calculation performed with M06-2X/cc-pVTZ providing a larger basis set. However, level 0 and level 1 calculations have been performed with B3LYP/6-311+G(d,p) which is less performing as a DFT to model this kind of large radical being less accurate in reproducing the orbitals behavior.

In this work additional simulations have been carried out with the same method, M06-2X, but assuming a different and larger basis set such as cc-pVTZ. Performing simulation at level 0 and level 1 the bond dissociation energy value seems to be more accurate even if the energy barrier appears largely underestimated. To refine these values single point energyl calculations have been performed with the same method and the same basis set allowing to reach more accurate results compared to those of Menon et al. [76] as shown in Figure 4.6. Considering the change in the basis set and the intrinsic higher accuracy linked to single point energy

calculations also level 1 results reached with M06-2X can be assumed reasonably reliable in a range of uncertainty of approximatively ±5 kcal/mol. According to the orange line it is possible to highlight that the DFT of level 0 and level 1 is more impacting with the final goal to reach higher performance with respect to high level calculations which, in this case, contribute just as a refining procedure.

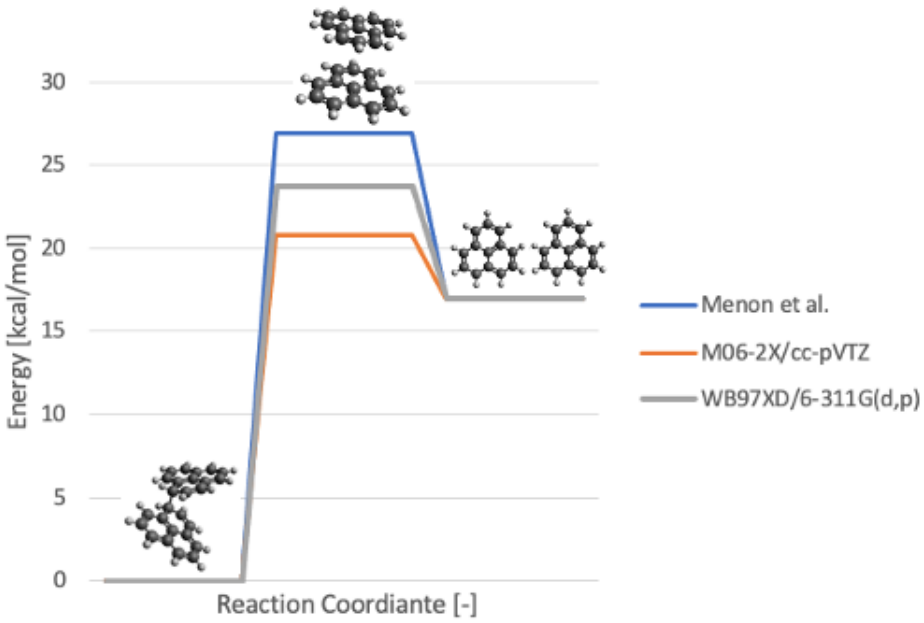

Figure 4.6: DFT comparison for delocalized π-radicals' recombination reaction.

An alternative refining procedure, presented in Figure 4.6, has been performed with the WB97XD method and with a smaller basis set, i.e. 6-311G(d,p), if compare to cc-pVTZ starting from level 1 guess previously optimized. The grey line reports a more accurate reproduction of the PES being the BDE value coherent with the previous one and the energy barrier less underestimated in its magnitude. The main advantage provided by the implementation of WB97XD as a DFT is linked to the possibility to better account for short-range and long-range interactions being classified as a separate-range functional.

It is known that barrier heights for a family of reactions tend to have a linear relationship between the barrier height and the enthalpy of reaction [90]. Figure 4.7 presents a plot of the barrier heights of the various cross-linking reactions against their bond enthalpy confirming the linearity and so the consistency of these values.

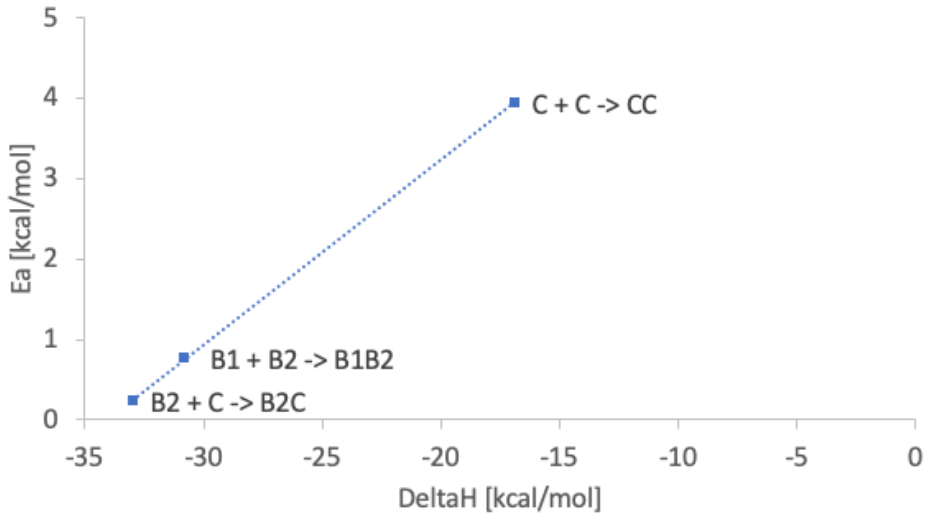

Figure 4.7: Plot of Enthalpy of Reaction vs. Barrier Height.

4.3 Rate Constants Computations

Following geometries optimization and preliminary calculations concerning thermodynamics properties and BDE computations the next steps are the rate constants and so rate rule derivation.

4.3.1 Barrierless Reactions

Barrierless reactions requires the implementation of a variational transition state theory procedure to compute kinetic constants as implemented on EStokTP. For this class of reactions, the similarity between the properties of transition state and reactant is pronounced and usually occurs when the geometry of the transition state is very similar to that of reactant molecule. In this case the reaction transition state is named loose, as already discussed, and it is not properly a physical transition state, but it is just a structure located on the PES in correspondence in a specific distance which provides the minimum flux and so the minimum rate constant. VTST defines the value of the rate of reaction as that assumed for that coordinate of reaction that minimizes the flux of reacting molecules.

In general, initially the rate constant decreases rapidly till reaching a minimum while the reaction coordinate increases. This sudden decrease is strictly correlated to the increase of the energy of the system that weight for a term $exp\left(-\frac{Ea}{RT}\right)$. After the prelaminar increase, to highlight a minimum on the kinetic constant curve those values start to growth again. Such increase of the kinetic constant is linked to the increase of the degree of freedom of the system involved in the reaction, in this case of the two monomers which are involved in the dissociation reaction till the chemical bond is broken. Increasing the distance and so the C—C bond length the rotational and vibrational partition functions increase too in their values at the transition state. The molecular

moment of inertia increases and while a decreasing trend is exploited by frequencies of vibration associated to the bending motions and to the torsional motions relatives to the bond that is breaking. The increase of the kinetic constant for elevated value of the reaction coordinate is often accompanied by the degeneration of the internal vibrational motions in internal rotational motions.

The computation of the variational rate constant is implemented with a non-automatic procedure on EStokTP which involves several steps:

- Potential energy surface reconstruction progressively increasing and freezing the bond length assuming a beta-scission reaction protocol following preliminary calculations regarding reactants and products.
- Transition state search, geometry optimization and energy calculation for each distance starting from 1.45 Å (C—C dimer bond length) to 10 Å assumed as reference bulk state with complete dimer dissociation.
- Transition state energy correction to account for correlation contribution and substitution of already corrected energies in input files for the rate constants computation at each distance.
- Ktp module activation on EStokTP, which recall the MESS solver, and output collection in rate.out.

The output of this procedure is a set of rate constants as a function of temperature and pressure.

Assuming the high-pressure limit, constants are reported in excel to reproduce the expected trend where the minimum can be located and selected as the variational rate constants expressed at different temperatures. It should be also noted that, for this methodology, limitations in the description of the transitional modes may limit the accuracy of its predictions. Significant deviation from predictions of any reaction path-based approach can be caused by the large amplitude nature of the transitional mode motions. It is also known that the Variable Reaction Coordinate TST (VRC-TST) approach provides a more accurate description of the transitional mode contributions even if as this procedure requires CASPT2 level calculations it could be too high computationally demanding while dealing with large PAHs as studied in this thesis.

As already mentioned, biphenyl radical recombination can be assumed as a reasonable benchmark reaction. In the work from Menon et al. the same reference has been adopted and **Errore. L'origine riferimento non è stata trovata.** suggests quite good agreement between the rate constant for phenyl radical recombination computed using BS-UM06-2X/cc-pVTZ and VTST and the predictions of Tranter et al. [91] and Jin et al. [92] in the range of 1000−2000 K. The negative temperature dependence and the order of magnitude predicted are captured by the use of the broken symmetry approach, although the decrease in the rate constant is steeper in comparison. This is likely due to the less accurate interaction energy predicted by the DFT method used here compared to the multireference methods employed by Tranter et al. [91], as well as differences in the

prediction of the enthalpy of reaction for the recombination, which is predicted to be −119.1 kcal/mol by BS-UM06-2X/6-311+G(d,p) compared to -117.9 predicted by CASPT2(2e,2o)/cc-pVDZ. Nevertheless, this comparison suggests that the methodology should suffice for initial estimates of the rate constants of radical-radical PAH reactions.

Rate constants are computed concerning the scission reaction procedure in a range of temperatures from 800 K to 2000 K, by accounting also pressure dependance. Starting from the PES scan the rate constant profile has been reconstructed considering just the temperature dependance and assuming the high-pressure limit. The distance which provides the minimum rate constant has been identify and the values isolated.

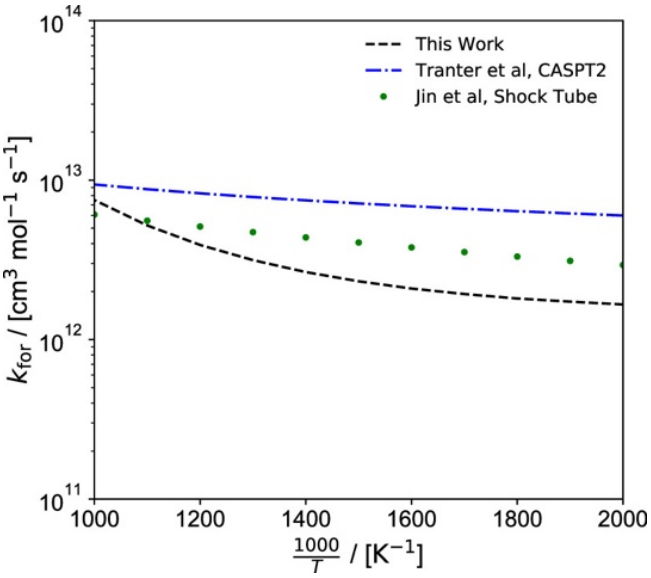

Figure 4.8: Comparison of the rate constant of phenyl radical recombination estimated using BS-UM06-2X/6.311+G(d,p) and VTST to those estimated by Tranter et al. [91] *and Jin et al.* [92]

In Figure 4.9 rate constants for recombination reactions have been reported. The trend highlights a more pronounced reactivity when σ-radicals are involved leading to higher rate constant and so to faster reactions. Counter wise, dealing with π-radicals the rate constants are lower and the kinetic less favored.

Just three barrierless reactions have been reported in Figure 4.9 as reference for the kinetic constants computation being A1 the most reactive radical and B2 one of the less reactive because of the stability provided by delocalization.

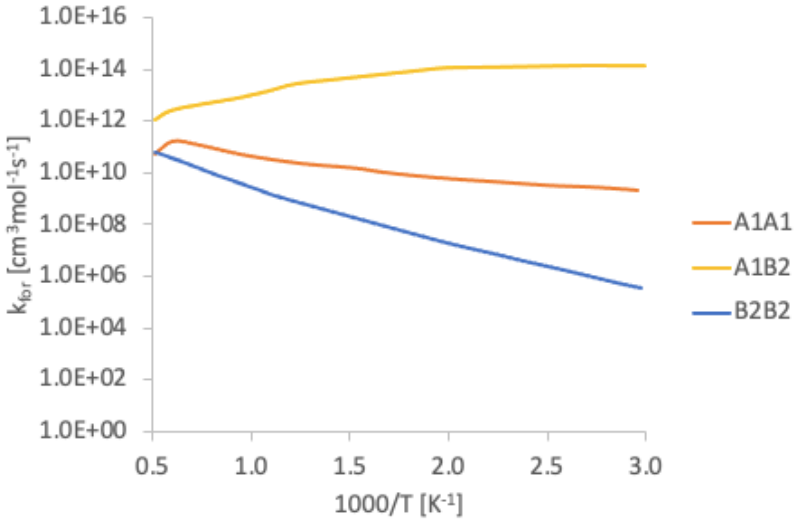

Figure 4.9: Rate Constants for Barrierless Reactions.

4.3.2 Reactions with Barriers

Counter wise, concerning reactions with barriers traditional transition state theory provides the desired result without issues linked to the computational procedure as previously mentioned for barrierless reactions. EStokTP routine for rate constants computation has been exploited which runs the master equation calculations running the MESS program. The coupled EStokTP and MESS codes are suitable for studying the pressure dependance of reaction kinetics.Monomers involved in the study are the same mentioned in Section 4.2.2 and the forward rate constants have been computed while dealing with recombination reactions. After a preliminary analysis of monomers and corresponding dimers energies, with the same method as before transition state search has been performed at different reciprocal C – C distances.

Calculations have been carried out at the same level of theory as previously discussed for the RRHO 1D HR model. Rate constants have been determined using the 1TS model which does not involve any reactant well. Adopting TST M06-2X/6-311+G(d,p) functional have been implemented for energies (such as dissociation energy and energy barrier) calculations followed by the kinetic constants computation.

In Figure 4.10 the whole set of rate constants for reactions with barrier are reported, the order of magnitude is approximatively always the same coherently with the consistency of their barrier height.

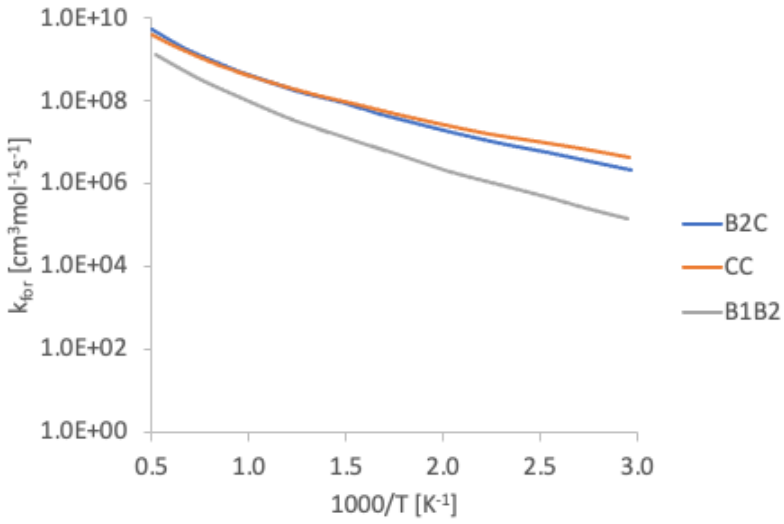

Figure 4.10: Rate Constants for Reactions with Barrier.

As stated at the beginning in 3.2 the main goal of EStokTP is to provide a theoretical framework that allows for high accuracy rate predictions. Occasionally, TST can be inaccurate because of the basic assumption of this theory such as nonrecrossing which limited the accuracy. In some cases, the energy is not randomized among all the molecular degrees of freedom, which can lead, among other things, to a situation where some of the potential PES sections are not explored. When this happens, predictions of rates and general computation results can become significantly inaccurate. The most proper approach is the study of the reaction dynamics using trajectory simulations with DFT energies and gradients. The level of uncertainty of the rate constant calculations is also expected to increase when the reacting system being considered has several coupled internal rotors, but this is not the case as it is just a 1D problem. Fortunately, such theoretical failure are quite limited and rate constants predictions by EStokTP becomes intrinsically safe and enough accurate for the class of reaction involved in this study.

4.4 Larger PAHs

The importance of the role of PAHs while dealing with soot nanoparticles formation has been already highlighted in previous chapter. As already discussed, dimerization reactions played as a fundamental step in the soot inception mechanism. However, monomers mentioned above are just a portion of molecules which compete as precursor and resonantly-stabilized radicals are key players in PAH growth. Recent studies build hypothesis to describe PAHs behavior correlated to their dimension by assuming their reactivity, beyond a critical size, as that of radicals. Resonantly-stabilized radicals (RSRs) are chief intermediates in soot inception and growth following the CHRCR mechanism which describe PAHs growth as reactions between radicals and hydrocarbons not just increasing cluster dimension but also providing regeneration of RSRs. PAHs require

activation through H-abstraction in order to reach radical state and in the following paragraphs dimerization of larger PAHs is going to be deeply investigated.

First of all, to better understand the aim of this study it is crucial to state which PAHs are going to be considered in the growth process by the addition step-by-step of an aromatic ring in different positions with respect to the starting molecular structure. According to Figure 4.1 the most interesting monomers are A1, B2 and C which are reported as example of each one of the categories considered in this work as σ-radicals and π-radicals both localized and delocalized. Starting from the already optimized structure of each of these monomers and the corresponding dimers, recombination reactions of larger PAHs are here considered, while dimerization reaction investigated in previous sections state as reference for BDE comparison and discussion. B2 and C have been selected as a reference for odd-C-numbered PAHs involving 6-membered rings and A1 as even-C-numbered PAH. These two classes of monomers have been considered separately to investigate different mechanism and different behaviors in reacting conditions. Odd-C-numbered PAHs rapidly loose a hydrogen atom form RSRs in combustion conditions, while even-C-numbered PAHs react as open shell rather than closed-shell molecules.

A complete overview of thermodynamic properties of all the investigated chemical species has been determined by the implementation of ab initio calculations using DFT functionals in Gaussian09. M06-2X has been adopted as functional and 6-311+G(d,p) as basis set providing enough accurate results. M06-2X allows to reach suitable predictions to describe chemical kinetics, it is also accurate concerning single-triplet energy gaps (ΔE_{S-T}) estimation for even-C-numbered PAHs with remarkable agreement with experimental data. Dealing with aromatic structures non-covalent interactions are relevant and both functional and basis set ensure precise modeling. Geometry optimization and energy computation accounts for level 0 and level 1 calculations corrected with ZPE value. Rate constants deal with H-abstraction as the starting step and dimerization reactions concerning self-recombination of PAHs monomers. EStokTP has been used to couple automatically electronic structure calculations, transition state theory and ME simulations to provide a priori predictions of temperature and pressure dependent rate constants.

4.4.1 Even-C-numbered PAHs

The starting point for the analysis of even-C-numbered PAHs is the monomer A1 (see Figure 4.1). Then the aromatic rings have been added progressively to increase PAHs size in order to define rate rule for PAH recombination reaction under combustion conditions. Aromatic rings addition starts from $C_{12}H_7$ (A1) which is a σ-radical, without changing the oddity of the large PAHs obtained. Two isomers of $C_{16}H_9$ have been investigated, i.e., adding one aromatic ring to A1 in two different positions as reported in Figure 4.11.

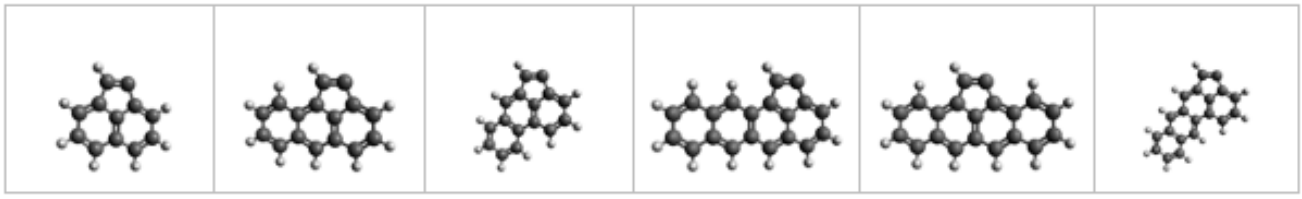

Figure 4.11: Even-C-numbered PAHs monomers.

In Table 4.6 three different isomers of $C_{20}H_{11}$ have been proposed with the corresponding energies reported as differences with the first isomer energy assumed as ground energy state as reference.

Isomers	Relative Energies [kcal/mol]
$C_{20}H_{11}$ – Isomer1	0.00
$C_{20}H_{11}$ – Isomer2	-1.46
$C_{20}H_{11}$ – Isomer3	-12.08

Table 4.6: Relative Energetic Stability of $C_{20}H_{11}$ Isomers.

All molecular structures have been investigated by simulations at level 0 and level 1 with the M06-2X functional as already mentioned. The energy of the isomers analyzed were found to be almost identical, as shown by the relatively small difference in the radical stability as highlighted Figure 4.12.

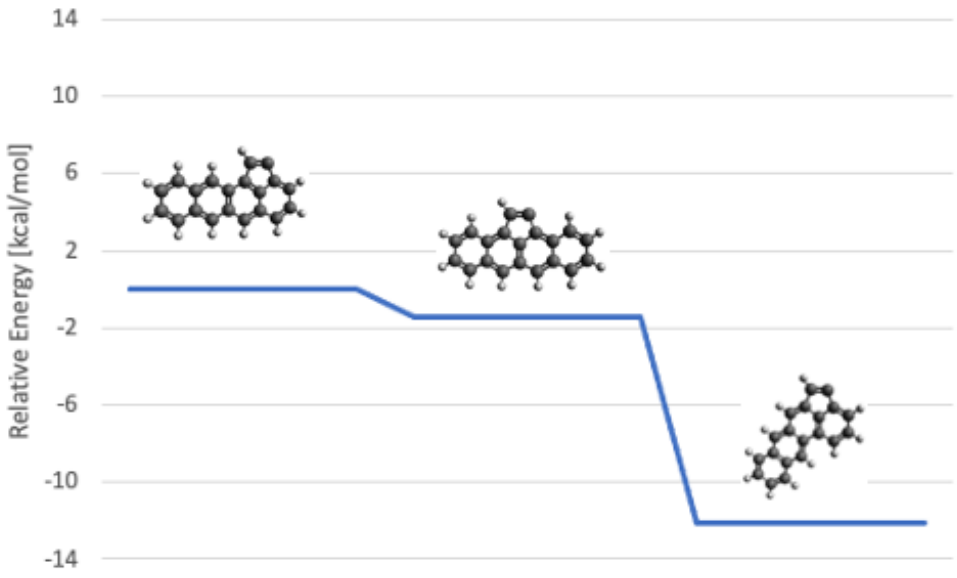

Figure 4.12: Relative Isomers Stability.

Therefore, only one related conformation has been considered for further calculations. For each of the monomers considered, the corresponding dimer has been optimized, such as $C_{24}H_{14}$, $C_{32}H_{18}$ and $C_{40}H_{22}$ as reported in Figure 4.13.

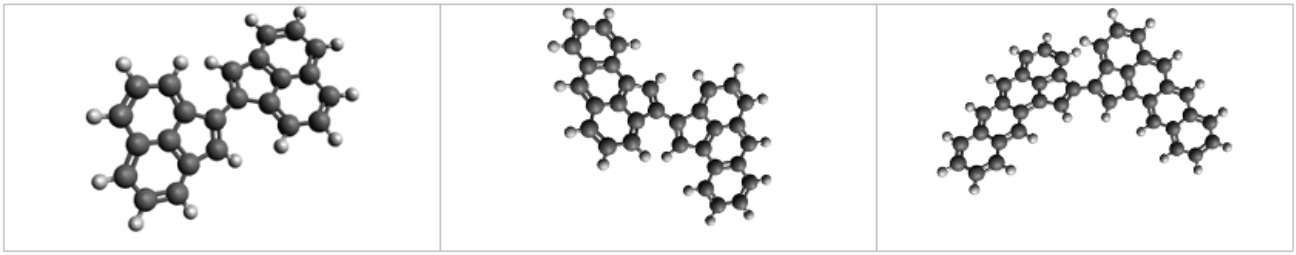

Figure 4.13: Even-C-numbered PAHs dimers.

Such dimers listed above have been optimized with same functionals and basis set. In the formulation of larger PAHs, it is important to take also into account the distortion of their structures, compared to flat, linear conformation such that of acenes, influencing the relative stability of the closed- and open-shell counterparts [93].

As shown in Table 4.7 bond energies have been computed considering self-recombination reactions of monomers reported in Figure 4.11. The energy gap between reactants and products agrees with the one of the same reactions but considering smaller structures such as A1 monomer and A1A1 dimer. The reference reaction has a recombination energy variation of 130.4 kcal/mol which is coherent with what obtained from these calculations. The trend which can be highlighted is that larger the structure smaller the energy gap but with a reasonably low change which can be considered quite negligible because of functionals uncertainties changing the implemented method. For such class of molecules, the spin density is localized as already discussed, increasing the number of carbon atoms no rearrangement in present and radicals do not delocalize.

Reactions	Bond Energies [kcal/mol]
$2C_{12}H_7 \rightarrow C_{24}H_{14}$	126.96
$2\ C_{16}H_9 \rightarrow C_{32}H_{18}$	127.92
$2\ C_{20}H_{11} \rightarrow C_{40}H_{22}$	127.86

Table 4.7: Bond energies for self-recombination reactions of larger PAHs.

Even-C-numbered PAHs molecules react exploiting open shell behavior rather than the close shell one. The same radical can populate the flame environment in two configurations such as in singlet or triplet form. In this specific case, considering a σ-radicals the dominant resonant structure is the singlet one reaching a higher energy state being the most reactive one. The same consideration can be done for dimers which are even-C-numbered too. Bond-recombination energies in Table 4.7 have been computed considering for both monomers and dimers the singlet configurations being the most diffuse in the studied conditions. Some additional considerations can be done referring to previous studies about the behavior of PAHs with increasing number of C-atoms. Even-C-numbered PAHs behave as acenes and per-acenes of different size and due to chemical similarity between the zigzag edges of acenes and the surface of peri-condensed PAHs and soot particles, peri-acenes represent a convenient model useful to study peri-condensed PAHs and soot particles.

As for acenes also in this case the triplet-single energy gap (ΔE_{S-T}) decreases with molecular weight. The decrease of (ΔE_{S-T}) with increasing molecular size is a common feature of even-C-numbered PAHs. Increasing the molecular weight ΔE_{S-T} tends to vanish such that triplet and singlet energy are progressively more similar. An inverse proportionality between barrier height and spin density, describing the localization/delocalization of unpaired electron density shows that these molecules react following a radical-like behavior. As in Figure 4.14.

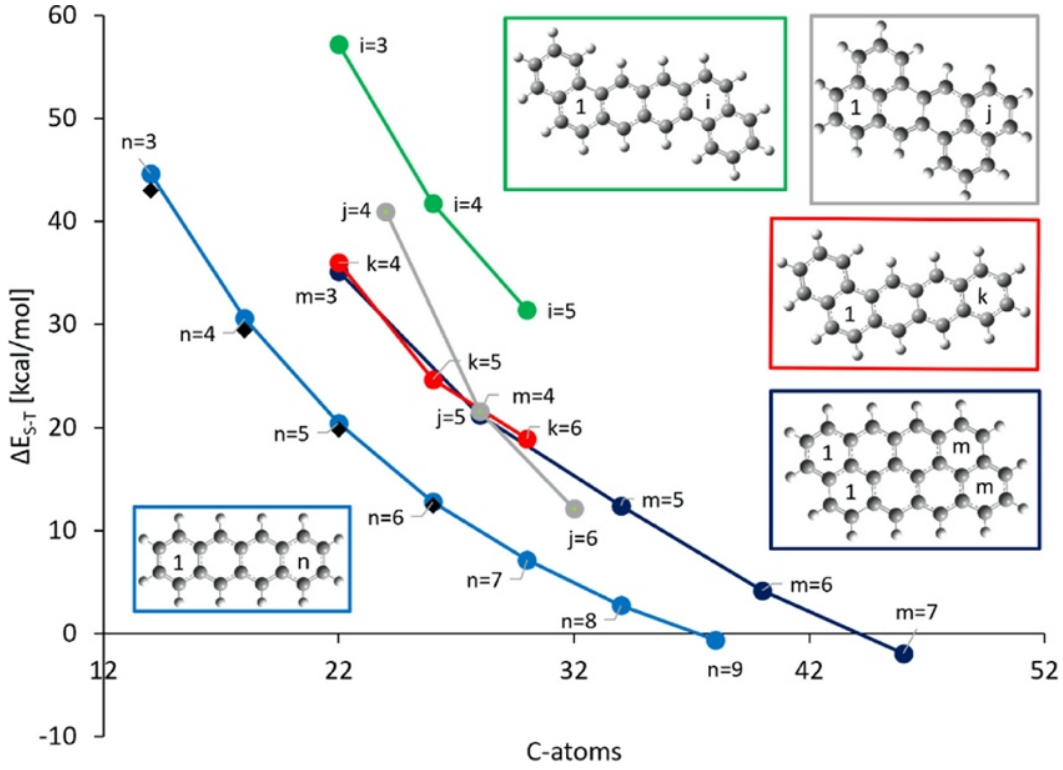

Figure 4.14: Singlet-Triplet Energy Gap ΔE_{S-T} adopted from [93] .

Monomers and dimers with A1-related structure, in Figure 4.11 and Figure 4.13, are not reported in Figure 4.14 but considering the even number of carbon atoms some considerations can be done. Being A1 a distortion, in terms of aromatic rings, of the species highlighted in blue but with n = 2, it is reasonable to assume that the curve describing the relative stability of singlet-triplet configurations could be located as the continuation of the blue one in correspondence of higher ΔE_{S-T}. This hypothesis confirm that the singlet configuration is the more reactive one and so reasonably assumed as the one which mostly reacts leading to self-recombination dimerization reactions. Considering $C_{16}H_9$ with n = 3 and $C_{20}H_{11}$ with n = 4, both structures can be reasonably located on the blue curve according to Figure 4.14 providing a decreasing energy gas between singlet and triplet radical conformation. Considering the corresponding dimers, they could be located on a curve split on the right side on the plot with a number of C-atoms between 24 and 40 but coupled with higher energy deviations being the species considered even more reactive and so being ΔE_{S-T} even higher but continuously decreasing with increasing molecular weight. The deviation just mentioned is linked to a

perturbation of the studied structures involving dimers of σ-radicals and rim-based pentagonal rings with respect to what is represented in Figure 4.14.

This analysis of the reaction kinetics of even-C-numbered PAHs shows that their reactivity is more like an open shell singlet diradical or a triplet with spin number equal to 1 a parallel spin, rather than a close shell singlet which is characterized by a spin number equal to 0. Starting from the monomer molecule as closed shell, with paired electrons, H-abstraction occurs, and radical behavior is exploited leading to self-recombination to dimers. Being the energy gap between reactant and products quite independent from molecules dimensions it leads to dimerization reactions reaching larger structures as intermediates in soot growth. In this specific case, concerning σ-radicals enhanced reactivity, the reaction is expected to be quite fast and favored as in the case study previously analyzed involving A1 and the corresponding dimer. Open shell reactivity predicted for PAHs is independent not just from dimension but also to temperature being the recombination energy quite constant because of the absence of delocalization. Even if the number of C-atoms in increased the radical behavior does not change and the relative stability of the radical monomers is constant so the tendence to react is not really influenced and these monomers are still the most reactive ones in combustion conditions.

According to the behavior exploited by monomers and dimers of larger PAHs while dealing with bond recombination energy, kinetic constants have been expected to have the same trend. While bond energies are quite similar each other and so independent from PAHs dimension the kinetic of these dimerization reactions might present similarity with the one of previously studied reactions such as A1 dimerization being these monomers reactive as the corresponding smaller one.

4.4.2 Odd-C-numbered PAHs

Following the pervious analysis for even-C-numbered PAHs, this paragraph deals with odd-C-numbered PAHs. Again, monomers optimization has been performed starting from B2 and C as reference for respectively localized and delocalized π-radicals, respectively, and the increase of PAHs dimension is studied for by adding progressively from one to three aromatic rings on different sites.

Odd-C-numbered PAHs which form during combustion processes can have a huge variety of possible structures and in their nonradical conformation they are characterized by the presence of a methylene group (Rn – CH2 – Rn) within a ring [93]. Differently from even-C-numbered PAHs, for odd-C-numbered PAHs H-abstraction from a methylene group of the closed-shell configuration takes place and resonantly-stabilized π-radicals are formed, resulting more and more stable as C-atom number increases. Two groups of π-radicals have been investigated in this work, by systematically adding fused-benzene rings to different edges of indene and phenalene as the simplest odd-C-numbered PAHs. Firstly, C_9H_7 (B2)-type monomers have been studied by

adding one aromatic ring up to $C_{17}H_{11}$ isomers, where two aromatic rings have been added, as shown in Figure 4.15. The starting configuration (B2), which is a localized radical, is assumed as reference. By increasing the number of carbon atoms, much more delocalization is provided. In this class of monomers, the methylene group is located on the free edge carbon atom of the partially embedded pentagonal ring. Also, C-type monomers have been considered in the study as delocalized π-radicals, with the methylene group located at the saturated carbon atom of the peripheral benzenoid ring, as shown in Figure 4.16.

PAHs reported in Figure 4.15 and Figure 4.16 are thermodynamically stable and the corresponding π-radical as a function of the molecular size is determined by the C – H bond dissociation energy of the methylene to generate the radical configuration, as RSRs. B2-type monomer PAHs generate localized radicals from H-abstractions, as C-type monomer PAHs which are even more stable due to enhanced unpaired electron delocalization [52].

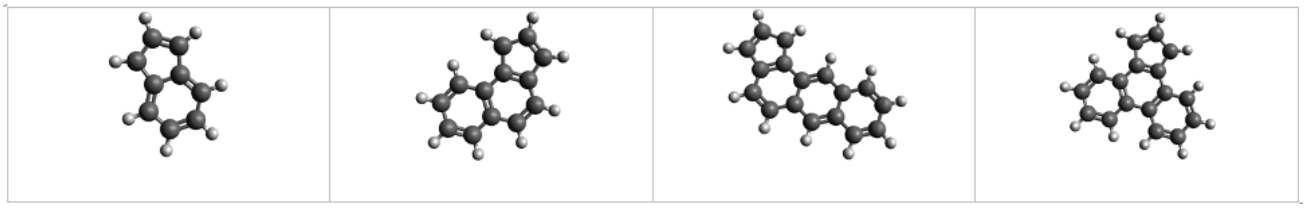

Figure 4.15: B2-based Larger PAHs odd-C-numbered.

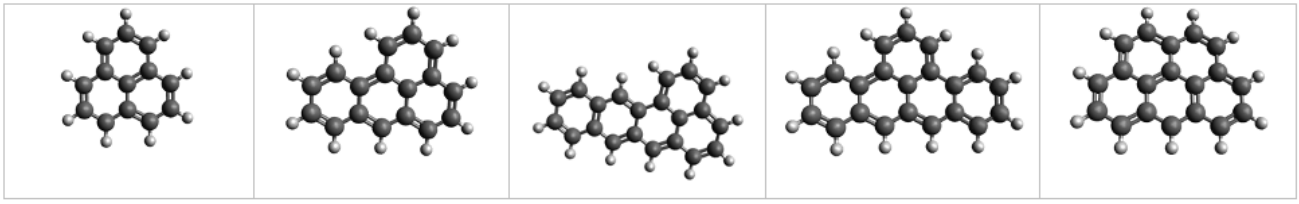

Figure 4.16: C-based Larger PAHs odd-C-numbered.

The dissociation energy reported in Figure 4.17 has been computed referring to the reaction which leads to the π-radical generation as PAH → H + πPAH. Group I, group II and group III are just partially of interest in this thesis being derivates of the considered monomers. I-1, II-2, III-1 and III-2 have been studied in detailed concerning dimerization reactions. The relative stability of those molecules has been investigated with respect to H-abstraction radical product.

Some different trends can be highlighted considering different family of PAHs molecules and so different generated radicals. Considering Group I, no strong dependence between the increase of molecular weight and the enthalpic contribution was found. Group II PAHs, instead, present higher stability with increasing number of C-atoms, and the same holds for Group III but with an even more pronounced stabilization of larger structures thanks to π-radical delocalization. Since entropy change in this system is similar for all the investigated reactions, so enthalpy is computed as the main energy contribution at 0K (ΔH_r^0) [93].

Such tendency of even-C-numbered PAH radical stabilization is confirmed in a wide range of temperatures ranging from 1500 K to 2200K.

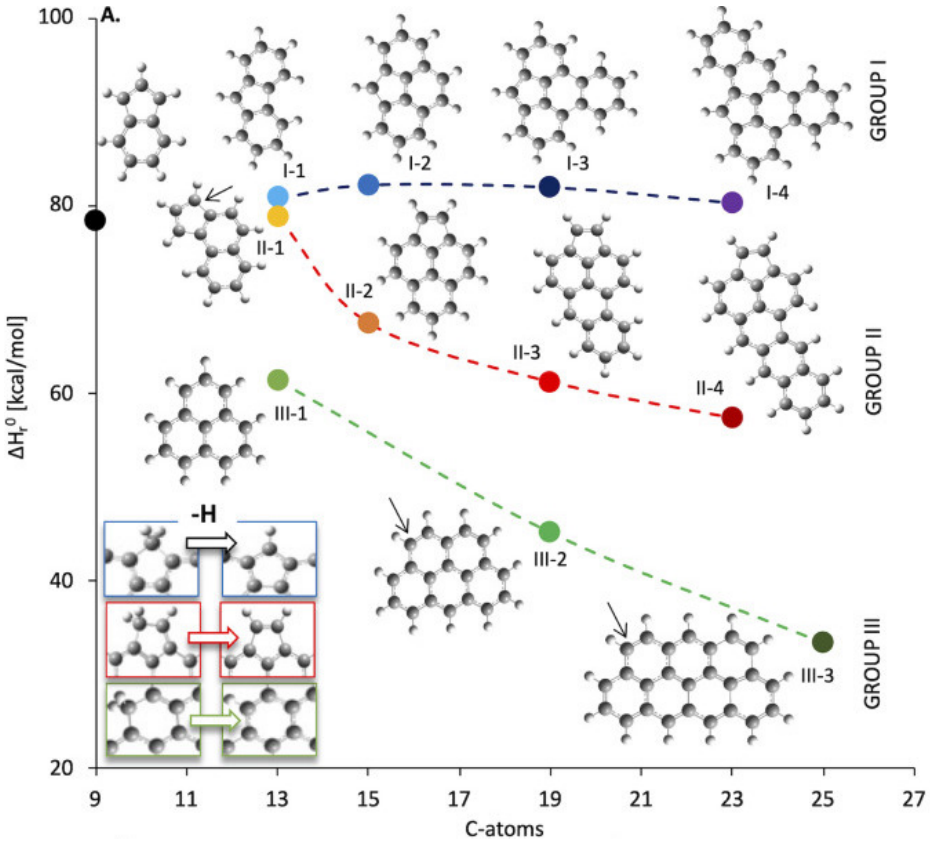

Figure 4.17: Relative Stability of odd-C-numbered PAHs adopted from [93].

From the aromatic structures discussed above, other lager monomers undergoing self-recombination have been considered. Starting from B2, some considerations are necessary, since with the stability of larger B2-type isomers is always similar and quite independent from the position of the added aromatic ring. Therefore, only one of them has been considered when determining recombination rates toward larger dimers. The same behavior has been identified concerning C-type PAH monomers, so that just some structures from Figure 4.16 have been considered.

In Figure 4.18 and Figure 4.19, larger dimers in their optimized geometry studied in this work have been reported.

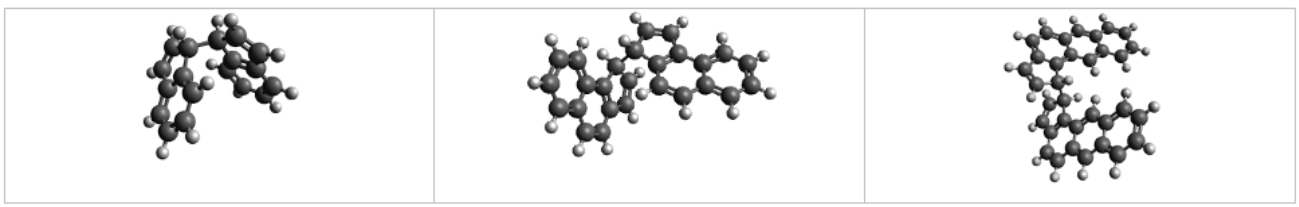

Figure 4.18: B2-based dimers even-C-numbered PAHs.

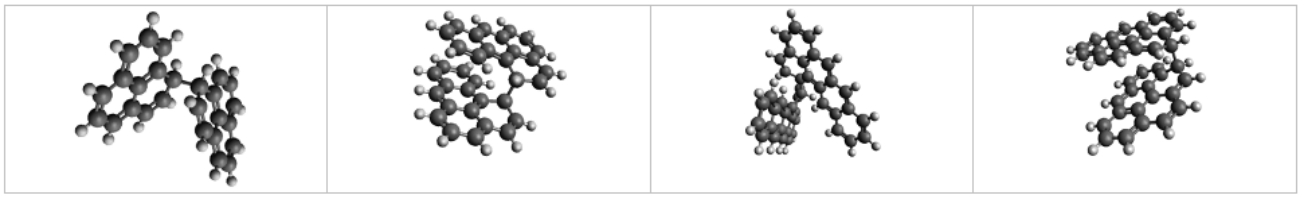

Figure 4.19: C-based dimers even-C-numbered PAHs.

Both monomers and dimers have been optimized with M06-2X functional and 6-311+G(d,p) basis set. Regarding geometry optimization of larger dimers, non-converging solution of the numerical simulation can often occur due to the high molecular weight of the species analyzed. To overcome this problem, a preliminary scan at level 0 of different geometries has been performed with the M06-2X functional, but with a smaller basis set as 6-31+G(d,p) which provided less computational effort. Level 1 calculations presented the same problem so they have been implemented firstly with M06-2X/6-31+G(d,p) to generated a reasonable first guess for the second optimization provided with M06-2X/6-311+G(d,p). The larger basis-set allowed to reach more accurate values finally used to compute the energies reported in Table 4.8 and Table 4.9.

Indene-based radical monomers and the corresponding dimers have been adopted for self-recombination energies computation. According to the results reported in Table 4.8 they are not influenced by the increase of molecular weight. By assuming B2B2 bond energies as 50.9 kcal/mol as reference in Table 4.1 and by considering the uncertainty due to the different functionals application used to reach optimization, they are reasonably in agreement, and it is possible to state that no dependance on the number of C-atoms is present. Being the monomers less reactive and with lower tendence to dimerize, the reactions class of these πPAH are expected to be slower than the one assumed as the reference following a slower H-abstraction being the molecules stabilized by resonance as already discussed.

Reactions	Bond Energies [kcal/mol]
2 C_9H_7 → $C_{18}H_{14}$	49.12
2 $C_{13}H_9$ → $C_{26}H_{18}$	50.61
2 $C_{17}H_{11}$ → $C_{34}H_{22}$	49.48

Table 4.8: Odd-C-numbered indene PAHs self-recombination energies.

Self-recombination energies have been estimated by ab initio calculations also for C-type monomer and the corresponding dimers, following the same computational procedure previously described. The corresponding trend of the BDE obtained is quite different from the previous case related to B2-type monomers. Assuming CC dimers reaction as the reference a reduction in the bond energy can be highlighted leading to less strong bond while dimerization occurs. Delocalized π-radical reaction has a self-recombination energy of 16.89 kcal/mol (see Table 4.4), which is much higher than 8.87 kcal/mol (see Table 4.9) being the corresponding

radicals much more stable due to the delocalization of unpaired electrons it is reasonable that the tendency of such monomers to stick together increases.

In Table 4.9 the reaction energies involving six-membered rings as C-type monomers are reported. They have been computed assuming the same DFT functionals as before. Considering PAH growth, from one to three aromatic rings have been added on different sites and considering dimers with more than 38 C-atoms many convergence problems have been encountered linked to the large molecular structure and the presence of a hindered rotor which further complicates the first guess structure and the optimization procedure. Many trials have been performed trying to find convergence with smaller basis set and then refining the calculations adopting larger basis set but no reasonable results have been gained. No consistency is present regarding negative bond energies.

Reactions	Bond Energies [kcal/mol]
2 $C_{13}H_8$ → $C_{26}H_{16}$	16.89
2 $C_{17}H_{11}$ → $C_{34}H_{22}$	8.87
2 $C_{19}H_{11}$ → $C_{38}H_{22}$	-12.27
2 $C_{21}H_{13}$ → $C_{42}H_{26}$	-23.99

Table 4.9: Odd-C-numbered six-membered-ring PAHs self-recombination energies.

The dimerization reactions between delocalized π-radicals, differently from the others previously discussed, are not barrierless. It could be useful to investigate how the energy barrier changes with the increase of PAH size, in order to reach a deeper understanding on such large PAH-type reactivity, by assuming a reference barrier of 3.94 kcal/mol for C+C→CC reaction (see Section 4.2.2).

Some additional considerations can be done considering that all dimers cited above are even-C-numbered and so their behavior may be influenced by spin singlet fission toward a triplet ground state [93]. Being dimers, their configuration is a perturbation of those reported in Figure 4.14 and none of the designed curves can be assumed as reference. $C_{26}H_{18}$ and $C_{34}H_{22}$ can be located on a fictitious line as the blue one but shifted on the right being the monomer composed of a six-membered ring and the dimers with a higher number of carbon atoms. Considering C-based larger dimers such as $C_{34}H_{22}$ and $C_{42}H_{26}$ they can be located on a curve similar to the grey one being similar but with structural perturbation because of the dimerization bond. $C_{38}H_{22}$ shows a similarity from a geometrical point of view with the dark-blue highlighted specie even if the number of aromatic ring disposition is different. From this dimers collocation on Figure 4.14 it is possible to assume that they are more stable in their triplet configuration even if with larger structures the energy gap is progressively reduced till zeroing.

To confirm this observation in Table 4.10 some triplet-singlet energy gaps have been reported showing that C-based monomers are much less stable behaving as singlet rather than triplet. C-type dimers have been

studied because, as mentioned above, during the optimization procedure they presented difficulties to convergence for singlet configuration so the possibility to be more stable as triplet emerged. This hypothesis has been confuted by a successive optimization changing the spin number from 1 to 3 and so considering the dimer as a singlet. As stated by the positive values for the ΔE_{S-T} (see Table 4.10) the singlet configuration is much more stable.

Dimers	ΔE_{S-T} [kcal/mol]
$C_{38}H_{22}$	18.8253
$C_{42}H_{26}$	12.5502

Table 4.10: Singlet-Triplet Energy Gap (ΔE_{S-T}).

The ΔE_{S-T} decreases while structures become larger being the relative stability of the two studied configurations much more similar. The main problem correlated to these data is the inconsistency of the absolute values of the dimers electronic energies which do not reach convergence with the adopted DFT methods but dealing with differences some considerations can be reasonably done. Bond energy values can be located in Figure 4.14 as the predicted trend is correctly reproduced.

4.5 Rate Rules

The estimation of kinetic parameters for larger molecules is object of discussion in this Section dealing with previously mentioned PAH dimerization reactions. The prediction of the reactivity of complex molecules such as larger PAHs is obtained starting from rate constants of smaller radicals as a reference [94]. The goal is to understand the reactivity of a specific reaction class involving PAHs and to develop a rate rule-based model able to describe the kinetic of PAHs with analogous radical behavior but increasing C-atoms number.

4.5.1 Rate Rules for PAH reactions family

In previous work, effective methods for rate parameters prediction have been developed dealing with H-abstraction reactions from hydrocarbon species. Starting from a large set of well-defined experimental rate values and making use of proper analogy rules larger structures reactivity can be accurately predicted. Assuming as reference the work from Ranzi et al. [95], H-abstraction reactions can be characterized. Most of the predicted values agree reasonably with literature rate constants and these values can be useful when modeling larger kinetic schemes with more reactions and bigger molecules. The approach adopted in their work is based on an empirical model for predicting kinetic parameters, based on analogies among both radicals and H-atom types in the molecules. This method results easy to use and it gives results which agree reasonably

with large set of literature data and can be applied for estimating rate constants to most of the H-abstraction reactions where no experimental information is available.

Rate rules definition is a powerful tool to describe PAHs reactivity, being a wide class of reactions involving thousands of different isomers. As discussed in Section 4.4, increasing the number of C-atoms, i.e., PAH size, different reactive radicals and the related dimers were studied. Preforming ab initio calculations for geometry optimization and electronic energy computation, the bond recombination energy has been computed for each reaction considered in the study. For each class of larger PAHs, such as A1-type, B2-type and C-type, dimerization energies have been compared with the correspondent smaller PAH as reference, previously investigated by Menon et al. [76], respectively A1, B2 and C. Rate rules for the PAH family have been determined with a scaling factor applied on the pre-exponential factor in the Arrhenius expression of the rate constant, based on the assumption that the reactivity of the system remains substantially unchanged even if the radical structure becomes larger by aromatic ring addition. This trend is shown in Table 4.7, Table 4.8 and Table 4.9. The term reactivity expresses the bond energy analogy previously presented which is correlated to a similar behavior of radicals following the recombination pathways and showing no dependance from the size of the aromatic structure. To formulate rate rules for a whole reaction class it is a necessary condition that the network does not change with the system size. For the specific systems under investigation, dominated by recombination reactions mainly behaving as barrierless it is important that no additional channels become active as reactants get larger. The same behavior needs to be exploited by reactions with barrier.

The rate rules are summarized by taking the average values of rate constants of a representative set of reactions in each class, which are applicable for the chemical model construction and later validation of PAHs while dealing with soot formation. Considering different reactions with the same type of PAHs but with progressively enlarging structures a correction factor might be adopted to scale the kinetic constants with respect to the number of C-atoms. The effect of PAH sizes, structures, and reaction sites on the rate constants has been examined. The results show that the PAH sizes have a negligible effect on the rate constants, while the structures of PAHs influence the rate constant significantly exploiting the same trend as for smaller structures. Such considerations drive to the assumption of a unitary scaling factor for the rate rules development. Being the enthalpy of reaction constant for PAH radicals of the same type (i.e., σ-radicals, localized π-radicals, delocalized π-radicals), it is reasonable to assume that the same size-independent behavior is featured by the corresponding rate constants

In Table 4.11 rate rules results are provided and divided according to the class of radicals involved, such as σ-radicals, localized π-radicals and delocalized π-radicals. The kinetic parameters reported have been derived according to a modified Arrhenius expression, $k=A*T^{n}*\exp(-Ea/RT)$, for reactions with barrier and to a sum of two modified Arrhenius expressions for barrierless reactions.

PAH GROWTH								
Reaction class	Applied on	Reference reaction	A1	n1	Ea1	A2	n2	Ea2
σ-radicals *Radical Recombination Reactions (RRR)*	2 $C_{16}H_9$ → $C_{32}H_{18}$ 2 $C_{20}H_{11}$ → $C_{40}H_{22}$	2 $C_{12}H_7$ → $C_{24}H_{14}$	23.3	2.83	-0.24	6.26E+04	2.65	26.26
localized π-radical *Radical Recombination Reactions (RRR)*	2 $C_{13}H_9$ → $C_{26}H_{18}$ 2 $C_{17}H_{11}$ → $C_{34}H_{22}$	2 C_9H_7 → $C_{18}H_{14}$	146	2.62	5.95	2.42E+36	-5.54	76.25
delocalized π-radical *Radical Recombination Reactions (RRR)*	2 $C_{17}H_{11}$ → $C_{34}H_{22}$ 2 $C_{19}H_{11}$ → $C_{38}H_{22}$ 2 $C_{21}H_{13}$ → $C_{42}H_{26}$	2 $C_{13}H_8$ → $C_{26}H_{16}$	2.02	2.64	5.6	-	-	-

Table 4.11: Rate rules adopted in PAH molecules. The kinetic parameters refer to the modified Arrhenius expression $k=A*T^n*exp(-Ea/RT)$ and units are mol, cm^3, kcal, s.

Chapter 5 – Model Validation

In this chapter a general overview about CRECK kinetic mechanism for PAH and soot formation is presented. Starting from PAH recombination reactions previously discussed, an attempt to validate the model has been considered necessary.

5.1 Model Introduction

The formation mechanism of small PAHs composed of one and two aromatic rings are relatively well understood, and the estimates of the relevant kinetic parameters are supported by experimental data. In contrast, understanding the growth to larger PAHs are rare and data typically do not include species larger than pyrene, because of the low abundance of these larger structures in flames.

Experiments and flame simulations taken together enable to follow quantitatively the transition from parent fuel molecule to PAHs and, eventually, soot. Importantly this approach resolved spatially the structure of flames even in the presence of steep gradients and, in turn, allowed to follow the molecular growth process in unprecedent detail. However, the accuracy of the data is often questionable because flame boundary conditions and flame temperature are often poorly characterized. The aim of the present chapter is the soot model validation dealing with previously discussed dimerization reactions for the inception step together with already computed rate constants.

Since reaction kinetics forming larger PAHs are not quantitatively established, the soot inception step in often modeled heuristically by considering the dimerization of PAHs with reaction rates that are turned to match experimentally measured soot volume fraction and particles size. This tuning procedure is more accurate under restricted flame conditions. The goal is to track PAH radicals evolution into dimers and, ultimately, soot in a highly controlled flame under incipient soot conditions to ensure soot nucleation stage in an environment which is favorable for the evolution from fuel to soot.

In this work different flames are going to be considered such as the burner-stabilized ethylene-oxygen-premixed flame and the diffusion flame of ethylene-nitrogen mixture. Starting from the CRECK kinetic model reactive species have been lumped according to their reactive edges and associated for similarity to the recombination reactions investigated above. Detailed particles size distribution functions and their time evolution, flame temperature, soot volume fraction and number density profiles were determined and reported. The aim is to track the evolution from parent molecule to multi-ring PAHs and, ultimately, to soot in a highly controlled flame under incipient soot conditions, to ensure compatibility of the diagnostics with soot load. The structure of the flames is computed using 1-D governing equations and so 1-D laminar flames

configurations, i.e., premixed burner-stabilized, premixed burner-stabilized stagnation and counterflow diffusion flames.

In order to accurately predict the soot emission from different practical fuels' combustion, the detailed description of soot precursor formation in the key sub-model. Detailed theoretical models are comprehensive of both gas-phase kinetic and dynamic of soot particles. Despite of the wide range of reactions and components involved in these models the main drawbacks are the computational cost and lost in efficiency especially when it is integrated into CFD simulations of engine combustion.

Laminar flame governing equations are implemented and solved using `OpenSMOKE++` suite, in Figure 5.1 the schematic structure of the solver is reported. It allows to simulate both ideals reactor (0-D solver) and 1-D laminar flames. The detailed combustion kinetic mechanism of combustion written in the standard CHEMKIN® format [96] is used and it is coupled with the fluid dynamics of the system in 1D simulations. Species, gas mixtures, kinetics models, equations of state, ODE integrators, and reaction path diagrams, etc are provided in the different classes of `OpenSMOKE++` library, written in object-oriented C++. The software is structured in classes, i.e., the Species class, the Mixture class, the Reaction class, and the Chemistry class, which menage the computation of thermodynamic and transport properties of mixture, the stoichiometry data, the kinetic parameters of each reaction and a collection of all the reactions involved in a specific kinetic mechanism.

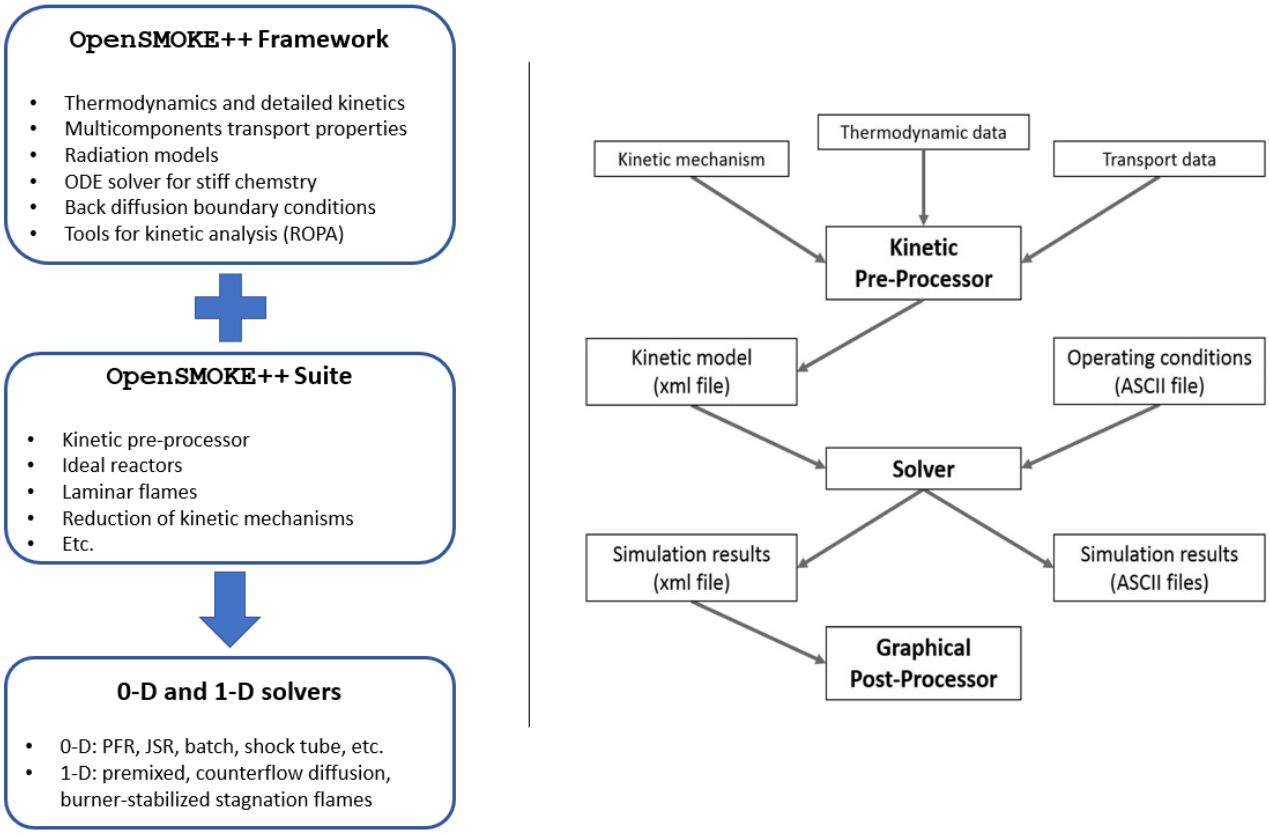

Figure 5.1: On the left the solvers employed for numerical simulations and on the right the structure of the `OpenSMOKE++` suite.

5.2 PAH Radical Recombination Rate Analysis

In Figure 5.2 the rate constants dependance with temperature is reported. Rate constants are computed from CRECK model [96] for different recombination reaction classes barrierless reactions, hereafter named CRECK1, and CRECK2, CRECK3 and CRECK4, which correspond to reactions with barrier but considering different parameters depending on the radicals involved in the recombination process such as σ-radicals and π-radicals. As expected barrierless reactions are faster than reactions involving π-radicals which are slower because of the more pronounced stability of the involved radicals. The main difference is how barrierless reactions are considered. In the CRECK kinetic mechanism no temperature dependance is accounted for, while in this thesis the rate constants here computed as the sum of two modified Arrhenius equations as in the work by Menon et al. [76].

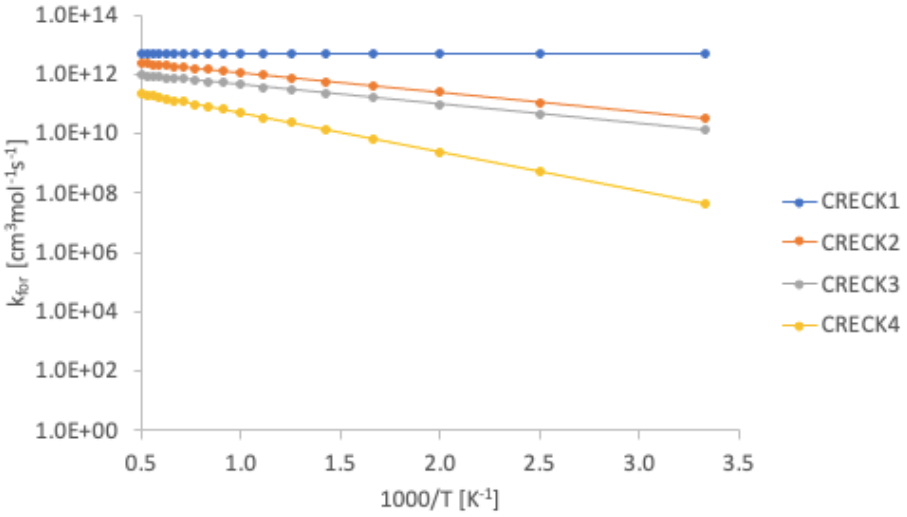

Figure 5.2: Forward rate constants from CRECK kinetic mechanism divided in different reaction classes according to the types of radicals involved.

For each one of the previously mentioned CRECK reactions classes, implemented through analogy rules [25], a comparison with the rate constants computed in this work from first-principles method is presented. The comparison reports rate constants involving different reactive edges but with common features in agreement with the CRECK classification according to the reactive behavior (with or without barrier) and to the PAH radical type (σ-radicals and π-radicals).

In Figure 5.3 the CRECK1 reactions class is compared with A1A1, A2B1 and B2B2 rate constants which are all barrierless reactions. The CRECK1 rate constant appears to be more than one order of magnitude higher than that computed in this work, providing a consequent overestimation of the soot inception rate, thus indicating a likely source of soot yield overestimation in flames where the contribution of CRECK1 to soot inception is significant, as discussed in the following section. On the right some additional reference reactions previously

discussed in this work and computed in [76] are reported, such as A2C and B1C, to confirm this trend even involving localized π-radicals.

Accordingly, the CRECK model has been updated with the rate constant computed in this work, also considering the different reactivity of aromatic structures involving different reactive edges, which was a missing information in the PAH radicals recombination in the CRECK model.

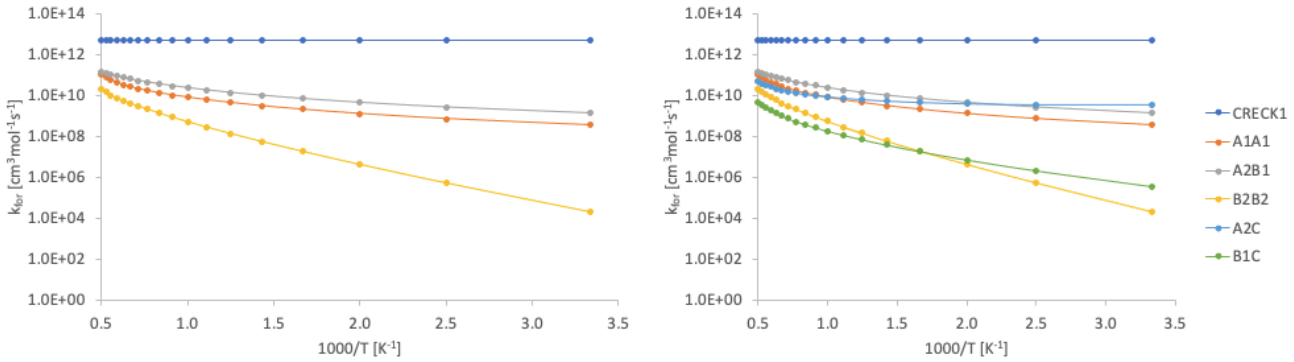

Figure 5.3: Barrierless Reactions Rate Constants.

Specifically, the CRECK rate constants for reactions with barrier are compared with reactions studied in this work involving σ-radicals and localized π-radicals in Figure 5.4. It highlights the same overestimation, as for barrierless reactions, of the rate constants adopted CRECK kinetic mechanism compared to that computed in this work, thus leading again to a likely overpredicted soot inception rate.

The reported reactions from the CRECK mechanism have been compared with A2B1 and A2C which involve the same types of recombining radicals.

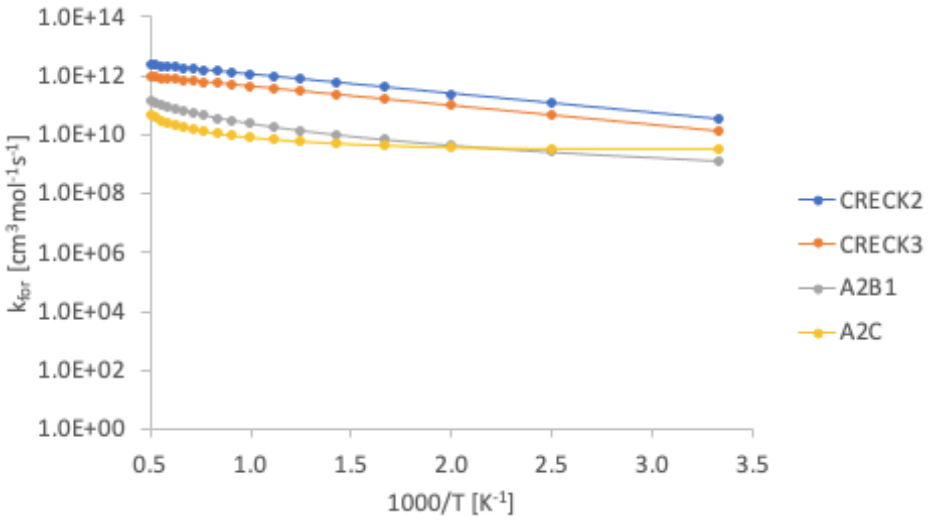

Figure 5.4: Rate Constants for Recombination Reactions of σ-radicals and localized π-radicals.

The same conclusions as before can be drawn dealing with delocalized π-radicals recombination reactions considered in the CRECK mechanism as reactions with barrier as for CC, B1B2 and B2C dimerization reactions.

Delocalized π-radicals stability leads to a lower order of magnitude in the rate constants presenting an even more pronounced overestimation with respect to the CRECK kinetic constants as reported in Figure 5.5.

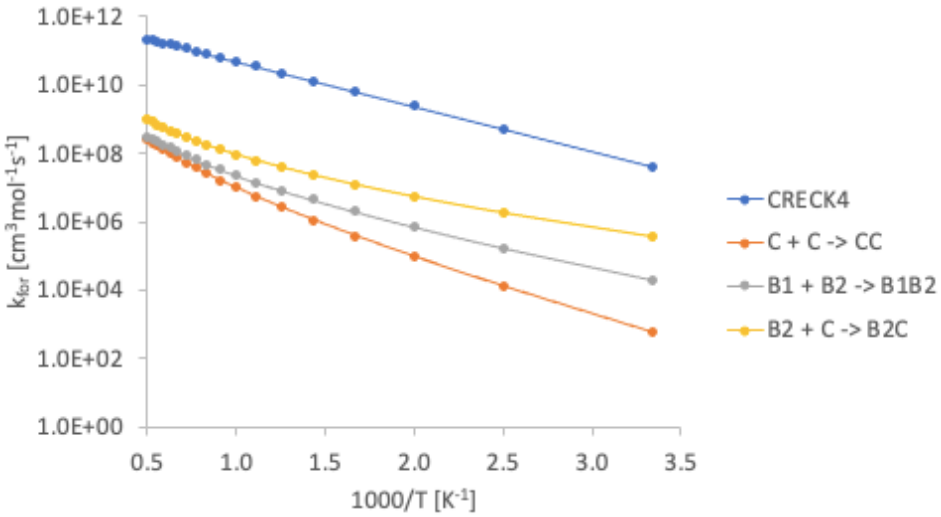

Figure 5.5: Rate Constants for Recombination Reactions of localized and delocalized π-radicals.

In Table 5.1 and Table 5.2 the kinetic parameters for the rate constants computation of the previously mentioned reactions are reported and grouped according to the radicals involved.

In Table 5.1 the main barrierless reactions parameters have been reported together with reactions characterized by recombination between σ-radicals and π-radicals which present a similarity with the dimerization reactions deeply investigated in this work.

	A1	n1	Ea1	A2	n2	Ea2
CRECK1	5.00E+12	0.00	0.00	-	-	-
CRECK2	5.00E+12	0.00	3000	-	-	-
CRECK3	2.00E+12	0.00	3000	-	-	-
A1A1	2.33E+01	2.83	-240	6.26E+04	2.65	26260
A2B1	1.01E+03	2.45	-70	2.11E+21	-2.19	37140
B2B2	1.46E+02	2.62	5950	2.42E+36	-5.54	76250
A2C	9.32E+02	2.20	-1530	2.14E+21	-2.18	34720
B1C	2.16E-01	3.12	2070	2.37E+36	-6.32	56990

Table 5.1: Kinetic Parameters for Recombination Reactions involving σ-radicals and π-radicals. The units are cm, kcal, mol, K, and s.

In Table 5.2 the kinetic parameters reported refers to localized and delocalized π-radicals which have been considered comparable for similarity to reactions with barrier.

	A1	n1	Ea1
CRECK 4	1.00E+12	0.00	6000
CC	2.02E+00	2.64	5620
B1B2	2.43E+00	2.57	3360
B2C	2.64E+00	2.66	2010

Table 5.2: Kinetic Parameters for Recombination Reactions involving localized and delocalized π-radicals. The units are cm, kcal, mol, K, and s.

5.3 PAH Radical Recombination Rate Analysis

The impact on the updated PAH radical recombination rates presented throughout this work to the CRECK soot model predictions is finally analyzed by comparing measured and simulated soot volume fraction profiles in several sooting flames characterized by different fuels. Then, kinetic analyses are performed to highlight the relative contribution of the main reaction classes considered in the model which govern soot inception in the set of flames investigated.

Firstly, three atmospheric ethylene flames characterized by different configuration (i.e., laminar premixed and counterflow) and different sooting tendency (i.e., low and high) are selected [ref a, ref b, ref c, see below], considering that ethylene is the most widely adopted fuel in experimental and modeling studies of soot formation [97]. The soot volume fraction profiles of the three ethylene flames are reported in Figure 5.6. The simulation results obtained with the base model (i.e., the original CRECK soot model [93]) are compared with three different updated models (Model A, Model B, Model C in Table 5.3). They include the recombination rates computed in this work for from two to four rings-PAHs along with different recombination rate of larger gas-phase PAHs considered in the model as lumped pseudo species, named BIN1 (20 C-atoms), BIN2 (40 C-atoms), BIN3 (80 C-atoms) and BIN4 (160 C-atoms) [93].

	BIN1-2J+BIN1-2J	BIN3-4J+BIN3-4J
Model A	with barrier	with barrier
Model B	barrierless	with barrier
Model C	barrierless	barrierless

Table 5.3: Reaction classes assumed for lumped gas-phase PAH radicals (i.e., BIN1-4J) recombination in Model A, Model B and Model C.

Figure 5.6 shows that for all the three ethylene flames considered there is no differences in the soot volume fraction computed with the updated models (A, B and C) and the base model. This result is consistent with the fact that in ethylene flames soot inception is primarily governed by HACA mechanism, while PAH

recombination has a negligible role in the formation of the first soot nuclei, independently of flame configuration, temperature, pressure, and equivalence ratio [47].

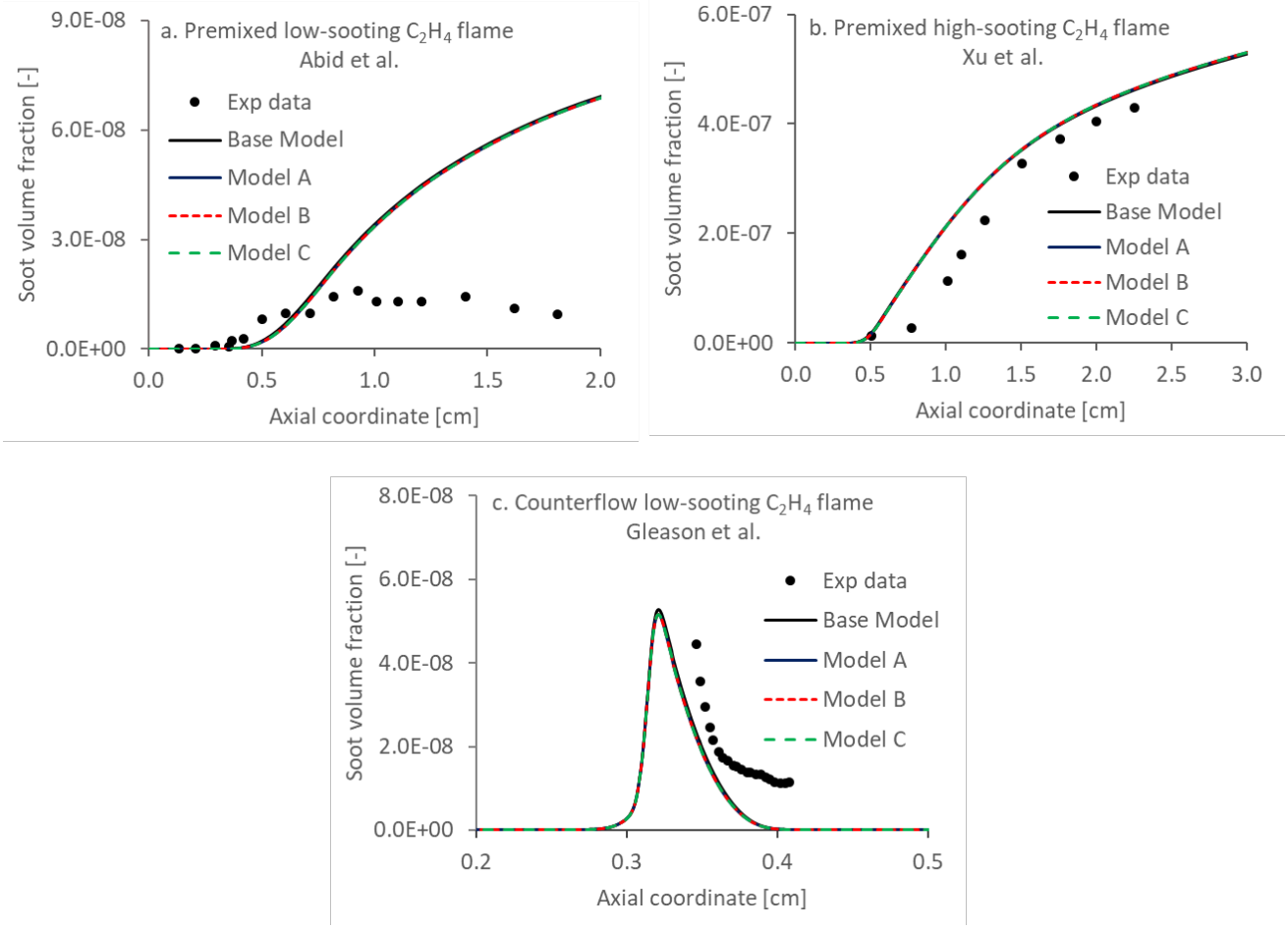

Figure 5.6: Measured and simulated soot volume fraction profiles in three different atmospheric ethylene flames: a) premixed low-sooting flame [98]*; b) premixed high-sooting flame* [99]*; c) counterflow low-sooting flame* [100].

Therefore, sooting flames characterized by fuels different from ethylene are selected aiming to analyze reactive conditions where the role of PAH radical recombination plays a major role in soot inception. Specifically, atmospheric counterflow sooting flames of six different conventional and alternative jet fuels, i.e. AJT, FT-SPK, HEFA-Camelina, Jet-A, JP-8 and JP-5 [101], are investigated. Details of the operative conditions, fuel and oxidizer mixtures are reported in [101]. The first three fuels are characterized by an almost negligible aromatic content, while in the latter three fuel mixtures the aromatic content is 18.53%, 13.56% and 20.36%, respectively. Moreover, they are rich of cycloparaffins (31.80%, 22.91% and 47.39%, respectively), whose dehydrogenation represents an additional source of aromatic species in the reactive environment. In Figure 5.7, measured soot volume fraction profiles of such flames are compared with the ones simulated with the base CRECK model and the updated one (Model B), i.e., the most representative of large PAH reactivity according to a recent theoretical study [93].

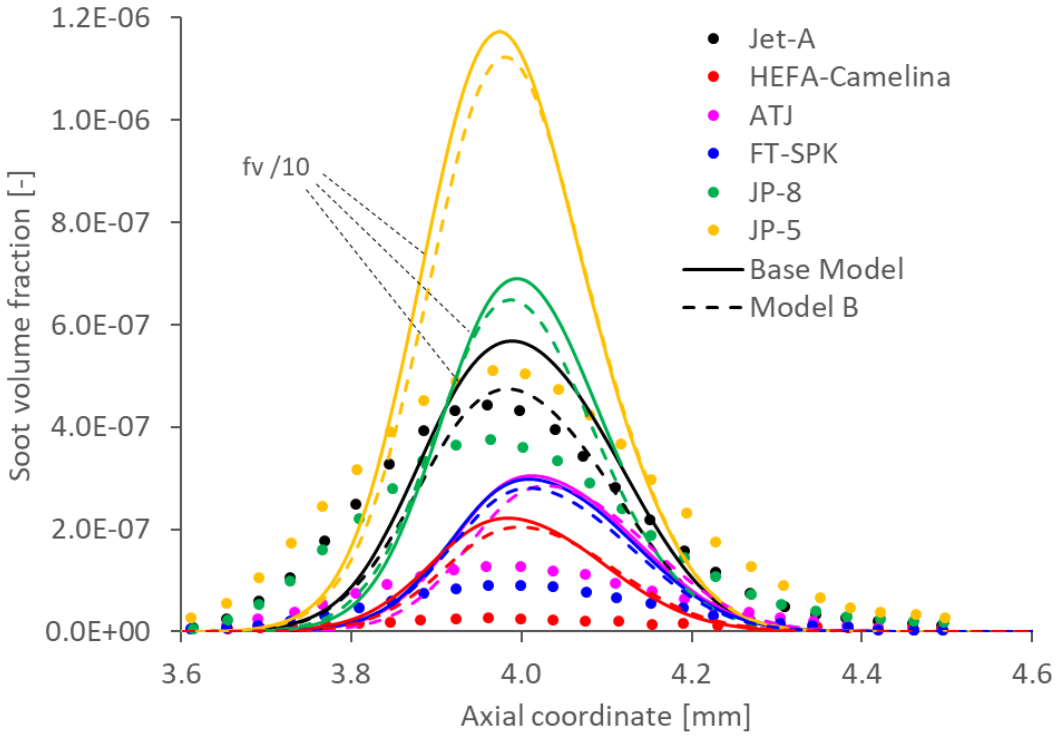

Figure 5.7: Measured and simulated soot volume fraction profiles of conventional and alternative jet-fuels. Symbols: experimental data [ref]; lines: model simulations.

Figure 5.7 clearly shows that the base CRECK model overpredicts the measured soot volume fraction in all the flames considered, but with a much larger overestimation in flames characterized by aromatic-rich fuels, i.e., Jet-A, JP-8 and JP-5. Similar results are obtained with the Model B, where PAH radical recombination rates were updated as explained in the previous chapters. However, due to the much lower PAH radical recombination rates considered in Model B (see 5.2), it can be observed a reduction in the predicted soot volume fraction compared to the results obtained with the base model. Such reduced soot yield is more important in aromatic-rich fuels, while it is much less significant in aromatic-poor jet-fuel flames (ATJ, HEFA-Camelina and FT-SPK), indicating a significant contribution of aromatic recombination to soot inception and consequently soot formation in the former, as expected being PAHs well-known soot precursors [28].

To highlight the role of PAH radical recombination as a function of the aromatic content in the jet-fuels, kinetic analyses are carried out considering ATJ and JP-5 flames as references for aromatic-poor and aromatic-rich flames, respectively.

In Figure 5.8, soot inception rates of different reaction classes considered in the CRECK soot model in ATJ, and JP-5 flames are compared. In both cases Figure 5.8a-c, the contribution on large gas-phase PAH radical class (BINgas+BINgas) dominates over other soot inception classes, i.e., smaller PAH radical recombination (PAHrad+PAHrad), PAH radical addition (PAHrad+PAHmol) and physical dimerization (PAHmol+PAHmol). However, the ratio between BINgas+BINgas and PAHrad+PAHrad peaks decreases from ~50 to ~30 in ATJ and

JP-5 flames, respectively, proving the much more important role of the latter reaction classes to soot inception when the fuel features a high aromatic content.

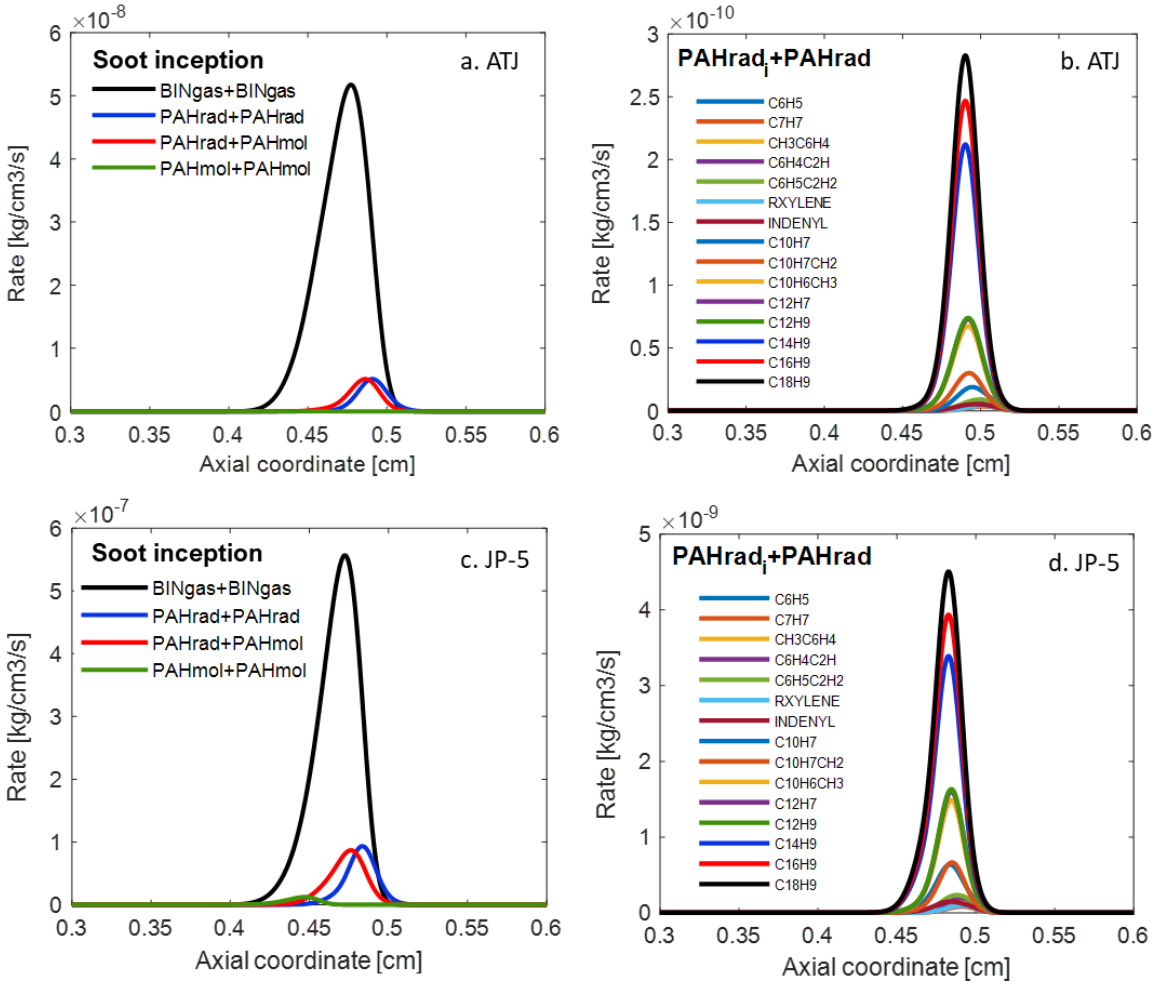

Figure 5.8: a) Soot inception rates of different reaction classes considered in the CRECK soot model in a) ATJ and c) JP-5 flame. Contribution of different PAH radicals to soot inception through PAH radical recombination reaction class model in b) ATJ and d) JP-5 flame. Soot inception rates for PAHrad+PAHrad, PAHrad+PAHmol and PAHmol+PAHmol are multiplied by a factor of 5 to allow a better graphical visualization.

Also, the total soot inception rate is larger in JP-5 flame compared to that in ATJ flame, leading to the corresponding much larger soot yield shown in Figure 5.7. The not negligible contribution of PAHmol+PAHmol class in Figure 5.8c corroborates the expected larger contribution of PAHs interaction to soot inception in JP-5 flame. Interestingly, a similar contribution between PAHrad+PAHrad and PAHrad+PAHmol classes is observed in Figure 5.8a-c. Furthermore, deepening the kinetic analysis in PAHrad+PAHrad class, it can be observed that role of α-methylnaphthalene radicals ($C_{10}H_6CH_3$ and $C_{10}H_7CH_2$) in JP-5 fuel is larger than that in ATJ being α-methylnaphthalene included only in the JP-5 fuel mixture Figure 5.8b-d.

Finally, the direct contribution of PAHrad+PAHrad class to the formation of the first lumped pseudo species assumed in the soot model, i.e. BIN1, is highlighted by considering the rate of production analysis (ROPA) of BIN1B (see in Figure 5.10), which has the largest mole fraction compared to the related lumped pseudo species

with same number of C-atoms but different hydrogenation level (BIN1A and BIN1B) and the related radicals (BIN1AJ, BIN1BJ, BIN1CJ), as shown in Figure 5.9 for both the flames considered. From Figure 5.9a-b it can be also observed a larger mole fraction of BIN1A in JP-5 rather than in ATJ flame, with BIN1A directly formed from PAH radical recombination (see kinetic mechanism attached in [93]).

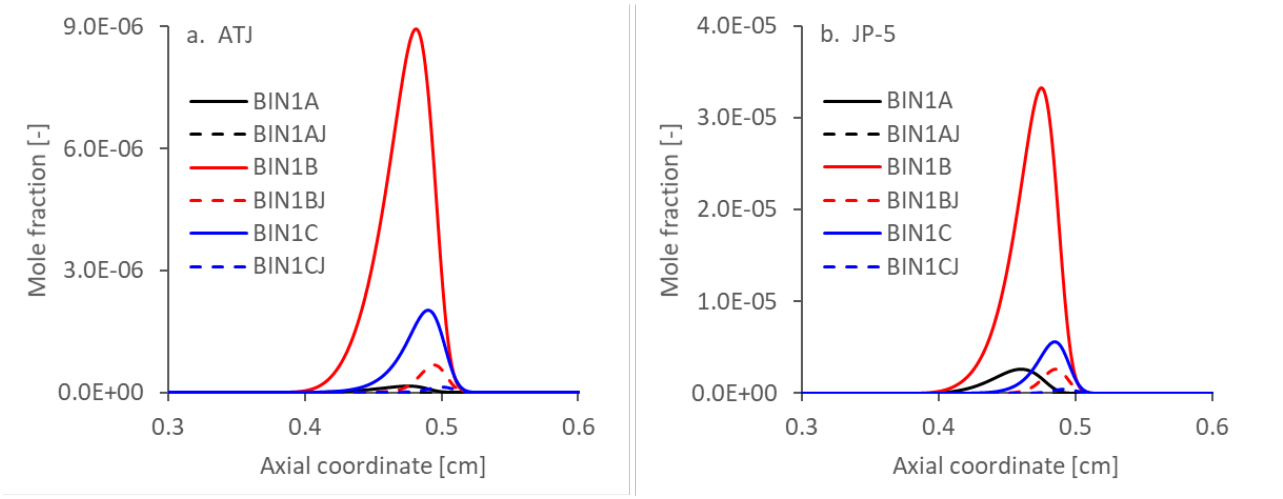

Figure 5.9: Mole fraction of the first lumped pseudo species (BIN1) considered in the CRECK soot model computed in a) ATJ and b) JP-5 flames. "J" indicates an open shell structure, i.e., a radical, while "A", "B", "C", indicates different hydrogenation level of a lumped pseudo species with the same number of C-atoms.

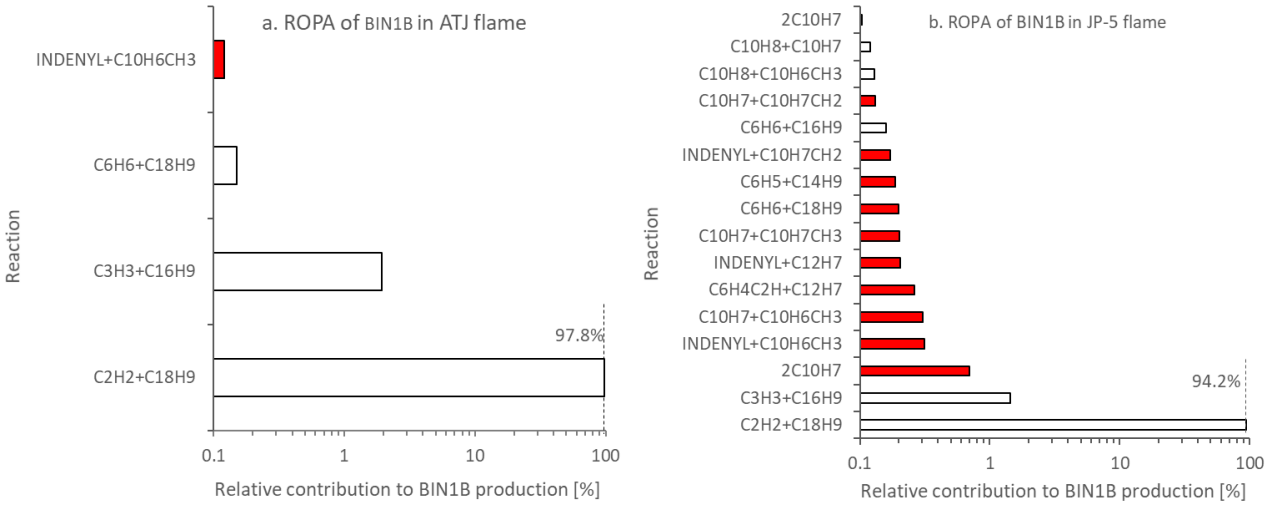

Figure 5.10: Computed relative contribution to BIN1B production of different reaction involving PAHs in a) ATJ and b) JP-5 flames.

As shown in Figure 5.10, while in ATJ flame BIN1B is almost completely produced by acetylene addition to C18H9 radical (97.8%), i.e., HACA mechanism, and propargyl recombination to pyrenyl (1.9%) (Figure 5.10a), in JP-5 flame there is a much larger contribution of PAHrad+PAHrad and PAHrad+PAHmol classes to BIN1B formation, including several combination of PAH as reactants, despite it is still governed by far by HACA mechanism (94.2%). Again, this result underlines the key role played by PAH radical recombination reactions in soot inception from aromatic-rich fuel combustion. On the other hand, it explains why in Figure 5.7 it was possible only to partially improve model predictions with the updated PAHrad+PAHrad rates computed in this

work, much lower than that implemented in the base CRECK model, being soot inception governed by HACA mechanism in both in ATJ and JP-5 flame. Therefore, future analysis should be dedicated to such mechanism with the aim of further reducing model overestimation of soot yield in both the jet-fuel flames investigated.

5.4 Evaluation of the Reversibility of PAH Recombination Reactions

Previous works on physical dimerization between small PAHs such as pyrene have fast forward rate constants, but they are known to be highly reversible at flame temperatures. It is known that reversibility is particularly important in soot nucleation. To get an idea of the reversibility and favorability at flame temperatures of the cross-linking reactions preciously investigated, the equilibrium constant can be computed. In Figure 5.11 forward and backward rate constants have been reported for three barrierless reactions from the previously analyzed set concerning PAH dimerization, i.e. A1A1, A1B2 and B2B2. These reactions have been reported as example involving both π-radicals and σ-radicals. Rate constants for barrierless reactions, as stated above, are described by the sum of two modified Arrhenius and in this section just the dominant contribution is going to be considered for the forward rate term. Counter wise, the backward rate constants have been automatically computed by `OpenSMOKE++` assuming the equilibrium and exploiting the thermodynamic consistency.

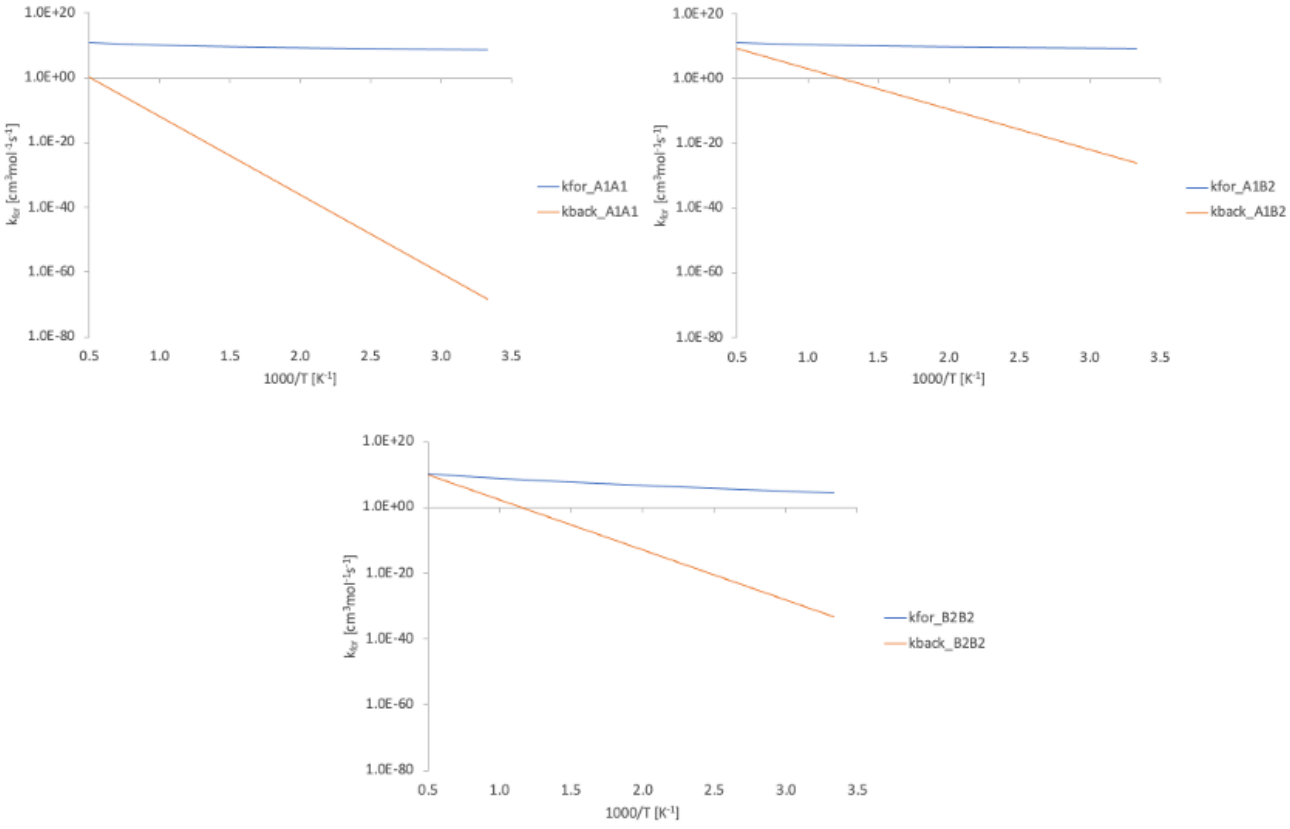

Figure 5.11: Rate Constants Comparisons, Forward vs Backward.

The comparison between forward and backward rate constants shows that cross-linking between certain reactive edge typed on PAHs form very stable bonds, which are much less likely to be reversible.

As shown in Figure 5.11 the backward rate constants are much lower than the forward contribution leading to an equilibrium constant well above 1 at flame temperatures and thus reactions have low reversibility as a result. At high temperature quite more consistent values have been gained where the reverse rate constants have the same order of magnitude as the forward one, but this temperature range is not of interest for the present study. The largest equilibrium constants and so the less enounced reversibility, as expected, are seen for the reactions containing σ-radicals edge type as A1 followed by reactions between these radicals and localized π-radicals, i.e. B2, as a consequence of the radicals reactivity and so to the tendency to dimerize.

Chapter 6 – Conclusions and Future Perspectives

Kinetics of cross-linking reactions between PAHs possessing different reactive edge types have been studied by means of density functional theory calculations being key intermediate in the soot formation process. The relevance of PAHs contribution comes from the relative abundance in the flame environment and to their tendency to the H-abstraction leading to the radical form which presents an enounced reactivity. Different molecules and different abstraction sites lead to different radical edges and consequently to different reactive behavior.

Firstly, some preliminary calculations have been performed with Gaussian09 providing geometry optimization and electronic energy computation. Reactions involving two PAH radicals have been observed to be broadly barrierless, namely, reactions between two PAHs of types A (aryl σ-radicals), B (localized π-radicals), and C (delocalized π-radicals). However, some reactions with barriers have been also investigated involving stabilized radicals, such as delocalized π-radicals, presenting a non-negligible activation energy being less reactive. Generally, cross-linking reactions resulted in the formation of strong chemical bonds had low barriers. For the computations of the bond energies and barrier heights dealing with recombination reactions different DFT methods have been tested with M06-2X/311+G(d,p).

The computation of the forward rate constants, with the MESS solver, confirmed that reactions involving edge type A are faster than others. It was noted that generally having the σ-radical on the five-member ring resulted in faster kinetics than when the σ-radical was on the six-member ring. Reactions involving combinations of edge types B and C were generally seen to be slower in comparison. Generally, all computed rate constants are unlikely to be high enough to result in significant fluxes for processes such as soot formation on their own, as the higher rate constants involve reactions between two radical PAHs that are expected to be in lower concentrations. This is also true for suggestions involving cross-links on five-member rings and delocalized π-radical PAHs.

Then, the modeling activity has been focused on the rate rules development dealing with larger PAH structures. For each one of the previously analyzed radical class, such as σ-radical and π-radicals, one monomer has been selected and the structures has been progressively enlarged with the addition of one to three aromatic ring on different edges. Larger structures spacing from 9 to 42 C-carbon atoms have been optimized and energies have been collected. The computation of the recombination energy for these dimerization reactions allows to develop a rate rule which states that no scaling factor is required to describe their reactivity so no dependance on PAHs dimensions has been reported. For such phenomena the kinetic

parameters computed for the reference species can be considered reasonably accurate also to model reactions involving larger PAHs.

The second part of this work concerns the validation of the CRECK soot kinetic mechanism updated with the PAH radicals recombination rate constants computed in the first part, assuming as rate parameters those associated to reactions between monomers with an explicate similarity in the reactive edges. Some simplify assumptions have been done to lumps the whole set of species provided in the model in reactions classes as those analyzed in this work. Generally, a good qualitative agreement has been observed between the modeled and experimental results, for both gaseous species and soot. A strong relationship between soot formation and aromatic species concentrations has confirmed the importance of coupling gas-phase with soot models. Specifically, the simulations of plug flow reactors and laminar premixed flat flames at different conditions have evidenced the relevance of PAHs contribution to the nucleation step. The rate parameters substitution in the kinetic mechanism highlighted an overestimation of the rate constants previously implemented in the model which consequently overestimates the soot formation rate. Specifically, for aromatic-rich jet-fuel counterflow flames, the current model is able to reduce the soot yield of the original CRECK model, where PAH recombination rates were significantly overestimated thus leading to a too fast soot inception. However, additional analysis on the mechanisms governing soot inception, such as HACA mechanism, must be carried out to further improve model predictions of soot volume fraction in such flames.

Further studies of likely competitive soot inception mechanisms could provide crucial insights to understand nascent soot nanostructure, which strongly affects the optical and electronic properties of carbon nanoparticles [102], varying the fuel and the operating conditions, also providing further contribution to the improvement of soot model capability to accurately describe the transition from gas phase to the solid phase.

References

[1] BP p.l.c, “Statistical Review of World Energy 2021,” *Bp*, vol. 70, 2021.

[2] B. P. Hands and D. Latest, “World Energy Review,” 2021.

[3] G. Baumbach, “Origin and Sources of Air Pollution,” in *Air Quality Control*, Berlin, Heidelberg: Springer Berlin Heidelberg, 1996, pp. 15–78.

[4] A. J. Koivisto *et al.*, “Source specific exposure and risk assessment for indoor aerosols,” *Sci. Total Environ.*, vol. 668, no. March, pp. 13–24, 2019, doi: 10.1016/j.scitotenv.2019.02.398.

[5] World Health Organization, “Modes of transmission of virus causing COVID-19: implications for IPC precaution recommendations,” *Geneva World Heal. Organ.*, no. March, pp. 19–21, 2020, doi: 10.1056/NEJMc2004973.Cheng.

[6] C. Mühlfeld, B. Rothen-Rutishauser, F. Blank, D. Vanhecke, M. Ochs, and P. Gehr, “Interactions of nanoparticles with pulmonary structures and cellular responses,” *Am. J. Physiol. Cell. Mol. Physiol.*, vol. 294, no. 5, pp. L817–L829, May 2008, doi: 10.1152/ajplung.00442.2007.

[7] F. Karagulian *et al.*, “Contributions to cities’ ambient particulate matter (PM): A systematic review of local source contributions at global level,” *Atmos. Environ.*, vol. 120, pp. 475–483, Nov. 2015, doi: 10.1016/j.atmosenv.2015.08.087.

[8] M. S. Callén, M. T. de la Cruz, J. M. López, and A. M. Mastral, “PAH in airborne particulate matter.,” *Fuel Process. Technol.*, vol. 92, no. 2, pp. 176–182, Feb. 2011, doi: 10.1016/j.fuproc.2010.05.019.

[9] A. D’Alessio, A. D’Anna, P. Minutolo, and L. A. Sgro, *Chapter 14: Nanoparticles of Organic Carbon (NOC) formed in Flames and their effects in urban atmospheres*. 2009.

[10] H. Shen *et al.*, “from 1960 to 2008 and Future Predictions,” *Environ. Sci. Technol.*, vol. 47, pp. 6415–6424, 2013.

[11] P. Rodrigues, B. Franzelli, R. Vicquelin, O. Gicquel, and N. Darabiha, “Coupling an LES approach and a soot sectional model for the study of sooting turbulent non-premixed flames,” *Combust. Flame*, vol. 190, pp. 477–499, Apr. 2018, doi: 10.1016/j.combustflame.2017.12.009.

[12] P. Yu *et al.*, “Black carbon lofts wildfire smoke high into the stratosphere to form a persistent plume,” *Science (80-.).*, vol. 365, no. 6453, pp. 587–590, Aug. 2019, doi: 10.1126/science.aax1748.

[13] H. Kasuga, *Health effects of air pollution*, vol. 38, no. C. 1989.

[14] Agency for Toxic Substances and Disease Registry (ATSDR), “Public Health Statement: Polycyclic Aromatic Hydrocarbons (PAHs),” *Atsdr.Cdc.Gov*, p. 6, 1995, [Online]. Available: http://www.atsdr.cdc.gov/toxprofiles/tp16-a.pdf.

[15] N. A. Yusof, S. F. Abd Rahman, and A. Muhammad, “Carbon Nanotubes and Graphene for Sensor Technology,” in *Synthesis, Technology and Applications of Carbon Nanomaterials*, Elsevier, 2019, pp. 205–222.

[16] R. L. Vander Wal and A. J. Tomasek, “Soot nanostructure: dependence upon synthesis conditions,” *Combust. Flame*, vol. 136, no. 1–2, pp. 129–140, Jan. 2004, doi: 10.1016/j.combustflame.2003.09.008.

[17] A. Luekewille *et al.*, “A Framework to Estimate the Potential and Costs for the Control of Fine Particulate Emissions in Europe,” no. November, pp. 1–33, 2001, [Online]. Available: http://pure.iiasa.ac.at/id/eprint/6497/.

[18] R. Belmans and P. Vingerhoets, “Molecules : Indispensable in the Decarbonized Energy Chain,” 2020, [Online]. Available: http://fsr.eui.eu/.

[19] W. Yuan, Y. Li, and F. Qi, “Challenges and perspectives of combustion chemistry research,” *Sci. China Chem.*, vol. 60, no. 11, pp. 1391–1401, Nov. 2017, doi: 10.1007/s11426-017-9066-9.

[20] A. N. Gachanja and P. K. Maritim, “Polycyclic Aromatic Hydrocarbons—Determination,” in *Reference Module in Chemistry, Molecular Sciences and Chemical Engineering*, Elsevier, 2018.

[21] M. Frenklach and H. Wang, “Detailed modeling of soot particle nucleation and growth,” *Symp. Combust.*, vol. 23, no. 1, pp. 1559–1566, Jan. 1991, doi: 10.1016/S0082-0784(06)80426-1.

[22] K. Kohse-Höinghaus, J. Troe, J.-U. Grabow, M. Olzmann, G. Friedrichs, and K.-D. Hungenberg, “Kinetics in the real world: linking molecules, processes, and systems,” *Phys. Chem. Chem. Phys.*, vol. 20, no.

16, pp. 10561–10568, 2018, doi: 10.1039/C8CP90054J.

[23] C. H. Wu, H. J. Singh, and R. D. Kern, “Pyrolysis of acetylene behind reflected shock waves,” *Int. J. Chem. Kinet.*, vol. 19, no. 11, pp. 975–996, Nov. 1987, doi: 10.1002/kin.550191104.

[24] M. Keller, T. De Bruin, M. Matrat, A. Nicolle, and L. Catoire, “A Theoretical Multiscale Approach to Study the Initial Steps Involved in the Chemical Reactivity of Soot Precursors,” *Energy and Fuels*, vol. 33, no. 10, pp. 10255–10266, 2019, doi: 10.1021/acs.energyfuels.9b02284.

[25] H. Richter and J. . Howard, “Formation of polycyclic aromatic hydrocarbons and their growth to soot—a review of chemical reaction pathways,” *Prog. Energy Combust. Sci.*, vol. 26, no. 4–6, pp. 565–608, Aug. 2000, doi: 10.1016/S0360-1285(00)00009-5.

[26] G. Blanquart and H. Pitsch, “Analyzing the effects of temperature on soot formation with a joint volume-surface-hydrogen model,” *Combust. Flame*, vol. 156, no. 8, pp. 1614–1626, Aug. 2009, doi: 10.1016/j.combustflame.2009.04.010.

[27] A. D’Anna and A. Violi, “A kinetic model for the formation of aromatic hydrocarbons in premixed laminar flames,” *Symp. Combust.*, vol. 27, no. 1, pp. 425–433, Jan. 1998, doi: 10.1016/S0082-0784(98)80431-1.

[28] H. Wang and M. Frenklach, “A detailed kinetic modeling study of aromatics formation in laminar premixed acetylene and ethylene flames,” *Combust. Flame*, vol. 110, no. 1–2, pp. 173–221, Jul. 1997, doi: 10.1016/S0010-2180(97)00068-0.

[29] M. Schenk, N. Hansen, H. Vieker, A. Beyer, A. Gölzhäuser, and K. Kohse-Höinghaus, “PAH formation and soot morphology in flames of C4 fuels,” *Proc. Combust. Inst.*, 2015, doi: 10.1016/j.proci.2014.06.139.

[30] F. Xu, P. B. Sunderland, and G. M. Faeth, “Soot formation in laminar premixed ethylene/air flames at atmospheric pressure,” *Combust. Flame*, vol. 108, no. 4, pp. 471–493, 1997, doi: 10.1016/S0010-2180(96)00200-3.

[31] J. A. Cole, J. D. Bittner, J. P. Longwell, and J. B. Howard, “Formation mechanisms of aromatic compounds in aliphatic flames,” *Combust. Flame*, vol. 56, no. 1, pp. 51–70, Apr. 1984, doi: 10.1016/0010-2180(84)90005-1.

[32] J. P. Senosiain and J. A. Miller, “The Reaction of n - and i -C 4 H 5 Radicals with Acetylene †,” *J. Phys. Chem. A*, vol. 111, no. 19, pp. 3740–3747, May 2007, doi: 10.1021/jp0675126.

[33] T.-C. Chu, Z. J. Buras, P. Oßwald, M. Liu, M. J. Goldman, and W. H. Green, “Modeling of aromatics formation in fuel-rich methane oxy-combustion with an automatically generated pressure-dependent mechanism,” *Phys. Chem. Chem. Phys.*, vol. 21, no. 2, pp. 813–832, 2019, doi: 10.1039/C8CP06097E.

[34] M. R. Djokic, K. M. Van Geem, C. Cavallotti, A. Frassoldati, E. Ranzi, and G. B. Marin, “An experimental and kinetic modeling study of cyclopentadiene pyrolysis: First growth of polycyclic aromatic hydrocarbons,” *Combust. Flame*, vol. 161, no. 11, pp. 2739–2751, 2014, doi: 10.1016/j.combustflame.2014.04.013.

[35] J. A. Miller and C. F. Melius, “Kinetic and thermodynamic issues in the formation of aromatic compounds in flames of aliphatic fuels,” *Combust. Flame*, vol. 91, no. 1, pp. 21–39, Oct. 1992, doi: 10.1016/0010-2180(92)90124-8.

[36] M. B. Colket, “The pyrolysis of acetylene and vinylacetylene in a single-pulse shock tube,” *Symp. Combust.*, vol. 21, no. 1, pp. 851–864, Jan. 1988, doi: 10.1016/S0082-0784(88)80317-5.

[37] C. F. Melius, M. E. Colvin, N. M. Marinov, W. J. Pit, and S. M. Senkan, “Reaction mechanisms in aromatic hydrocarbon formation involving the C5H5 cyclopentadienyl moiety,” *Symp. Combust.*, vol. 26, no. 1, pp. 685–692, Jan. 1996, doi: 10.1016/S0082-0784(96)80276-1.

[38] C. Saggese *et al.*, “Kinetic Modeling Study of Polycyclic Aromatic Hydrocarbons and Soot Formation in Acetylene Pyrolysis,” *Energy & Fuels*, vol. 28, no. 2, pp. 1489–1501, Feb. 2014, doi: 10.1021/ef402048q.

[39] H. Ghiassi, P. Toth, I. C. Jaramillo, and J. S. Lighty, “Soot oxidation-induced fragmentation: Part 1: The relationship between soot nanostructure and oxidation-induced fragmentation,” *Combust. Flame*, vol. 163, pp. 179–187, Jan. 2016, doi: 10.1016/j.combustflame.2015.09.023.

[40] C. Saggese, A. Frassoldati, A. Cuoci, T. Faravelli, and E. Ranzi, “A wide range kinetic modeling study of pyrolysis and oxidation of benzene,” *Combust. Flame*, vol. 160, no. 7, pp. 1168–1190, Jul. 2013, doi: 10.1016/j.combustflame.2013.02.013.

[41] C. Cavallotti, M. Pelucchi, and S. J. Klippenstein, "EStokTP From Electronic Structure to Temperature and Pressure Dependent Rate Constants," pp. 1–42, 2017.

[42] C. Cavallotti, M. Pelucchi, Y. Georgievskii, and S. J. Klippenstein, "EStokTP: Electronic Structure to Temperature- and Pressure-Dependent Rate Constants-A Code for Automatically Predicting the Thermal Kinetics of Reactions," *J. Chem. Theory Comput.*, vol. 15, no. 2, pp. 1122–1145, 2019, doi: 10.1021/acs.jctc.8b00701.

[43] Y. Georgievskii, J. A. Miller, M. P. Burke, and S. J. Klippenstein, "Reformulation and Solution of the Master Equation for Multiple-Well Chemical Reactions," *J. Phys. Chem. A*, vol. 117, no. 46, pp. 12146–12154, Nov. 2013, doi: 10.1021/jp4060704.

[44] S. Gudiyella, Z. J. Buras, T.-C. Chu, I. Lengyel, S. Pannala, and W. H. Green, "Modeling Study of High Temperature Pyrolysis of Natural Gas," *Ind. Eng. Chem. Res.*, vol. 57, no. 22, pp. 7404–7420, Jun. 2018, doi: 10.1021/acs.iecr.8b00758.

[45] K. O. Johansson, M. P. Head-Gordon, P. E. Schrader, K. R. Wilson, and H. A. Michelsen, "Resonance-stabilized hydrocarbon-radical chain reactions may explain soot inception and growth," *Science (80-.).*, vol. 361, no. 6406, pp. 997–1000, Sep. 2018, doi: 10.1126/science.aat3417.

[46] H.-B. Zhang, D. Hou, C. K. Law, and X. You, "Role of Carbon-Addition and Hydrogen-Migration Reactions in Soot Surface Growth," *J. Phys. Chem. A*, vol. 120, no. 5, pp. 683–689, Feb. 2016, doi: 10.1021/acs.jpca.5b10306.

[47] W. Pejpichestakul *et al.*, "Examination of a soot model in premixed laminar flames at fuel-rich conditions," *Proc. Combust. Inst.*, vol. 37, no. 1, pp. 1013–1021, 2019, doi: 10.1016/j.proci.2018.06.104.

[48] M. Frenklach and A. M. Mebel, "On the mechanism of soot nucleation," *Phys. Chem. Chem. Phys.*, vol. 22, no. 9, pp. 5314–5331, 2020, doi: 10.1039/D0CP00116C.

[49] T.-C. Chu, Z. J. Buras, B. Eyob, M. C. Smith, M. Liu, and W. H. Green, "Direct Kinetics and Product Measurement of Phenyl Radical + Ethylene," *J. Phys. Chem. A*, vol. 124, no. 12, pp. 2352–2365, Mar. 2020, doi: 10.1021/acs.jpca.9b11543.

[50] H. Sabbah, L. Biennier, S. J. Klippenstein, I. R. Sims, and B. R. Rowe, "Exploring the role of PAHs in the formation of soot: Pyrene dimerization," *J. Phys. Chem. Lett.*, vol. 1, no. 19, pp. 2962–2967, 2010, doi: 10.1021/jz101033t.

[51] A. Faccinetto *et al.*, "Evidence on the formation of dimers of polycyclic aromatic hydrocarbons in a laminar diffusion flame," *Commun. Chem.*, vol. 3, no. 1, pp. 1–8, 2020, doi: 10.1038/s42004-020-00357-2.

[52] J. W. Martin *et al.*, "Reactivity of Polycyclic Aromatic Hydrocarbon Soot Precursors: Implications of Localized Radicals on Rim-Based Pentagonal Rings," *J. Phys. Chem. C*, vol. 123, no. 43, pp. 26673–26682, 2019, doi: 10.1021/acs.jpcc.9b07558.

[53] J. W. Martin *et al.*, "Polar curved polycyclic aromatic hydrocarbons in soot formation," *Proc. Combust. Inst.*, vol. 37, no. 1, pp. 1117–1123, 2019, doi: 10.1016/j.proci.2018.05.046.

[54] C. Cavallotti and D. Polino, "On the kinetics of the C5H5 + C5H 5 reaction," *Proc. Combust. Inst.*, vol. 34, no. 1, pp. 557–564, 2013, doi: 10.1016/j.proci.2012.05.097.

[55] M. Dente, G. Bozzano, T. Faravelli, A. Marongiu, S. Pierucci, and E. Ranzi, "Kinetic Modelling of Pyrolysis Processes in Gas and Condensed Phase," 2007, pp. 51–166.

[56] M. B. Colket and D. J. Seery, "Reaction mechanisms for toluene pyrolysis," *Symp. Combust.*, vol. 25, no. 1, pp. 883–891, Jan. 1994, doi: 10.1016/S0082-0784(06)80723-X.

[57] J. Houston Miller, K. C. Smyth, and W. G. Mallard, "Calculations of the dimerization of aromatic hydrocarbons: Implications for soot formation," *Symp. Combust.*, vol. 20, no. 1, pp. 1139–1147, Jan. 1985, doi: 10.1016/S0082-0784(85)80604-4.

[58] A. D'Anna and J. H. Kent, "Modeling of particulate carbon and species formation in coflowing diffusion flames of ethylene," *Combust. Flame*, vol. 144, no. 1–2, pp. 249–260, Jan. 2006, doi: 10.1016/j.combustflame.2005.07.011.

[59] M. J. Thomson, "No Title," 2019.

[60] M. Frenklach and H. Wang, "Detailed Mechanism and Modeling of Soot Particle Formation," in *Soot Formation in Combustion: Mechanisms and Models*, 1994, pp. 165–192.

[61] M. Commodo, G. De Falco, A. Bruno, C. Borriello, P. Minutolo, and A. D'Anna, "Physicochemical

evolution of nascent soot particles in a laminar premixed flame: from nucleation to early growth," *Combust. Flame*, vol. 162, no. 10, pp. 3854–3863, Oct. 2015, doi: 10.1016/j.combustflame.2015.07.022.

[62] C. A. Schuetz and M. Frenklach, "Nucleation of soot: Molecular dynamics simulations of pyrene dimerization," *Proc. Combust. Inst.*, vol. 29, no. 2, pp. 2307–2314, Jan. 2002, doi: 10.1016/S1540-7489(02)80281-4.

[63] B. . Stanmore, J. . Brilhac, and P. Gilot, "The oxidation of soot: a review of experiments, mechanisms and models," *Carbon N. Y.*, vol. 39, no. 15, pp. 2247–2268, Dec. 2001, doi: 10.1016/S0008-6223(01)00109-9.

[64] M. E. Mueller, G. Blanquart, and H. Pitsch, "Modeling the oxidation-induced fragmentation of soot aggregates in laminar flames," *Proc. Combust. Inst.*, 2011, doi: 10.1016/j.proci.2010.06.036.

[65] R. L. Vander Wal and A. J. Tomasek, "Soot oxidation: Dependence upon initial nanostructure," *Combust. Flame*, 2003, doi: 10.1016/S0010-2180(03)00084-1.

[66] H. Guo, P. M. Anderson, and P. B. Sunderland, "Optimized rate expressions for soot oxidation by OH and O2," *Fuel*, vol. 172, pp. 248–252, 2016, doi: 10.1016/j.fuel.2016.01.030.

[67] H. Ghiassi, P. Toth, I. C. Jaramillo, and J. A. S. Lighty, "Soot oxidation-induced fragmentation: Part 1: The relationship between soot nanostructure and oxidation-induced fragmentation," *Combust. Flame*, vol. 163, pp. 179–187, 2016, doi: 10.1016/j.combustflame.2015.09.023.

[68] H. Ghiassi, I. C. Jaramillo, P. Toth, and J. A. S. Lighty, "Soot oxidation-induced fragmentation: Part 2: Experimental investigation of the mechanism of fragmentation," *Combust. Flame*, vol. 163, pp. 170–178, 2016, doi: 10.1016/j.combustflame.2015.09.022.

[69] D. E. Edwards, "Elementary Kinetics of Soot Oxidation by OH," University of California, Berkeley, 2014.

[70] X. Cheng, H. Jv, and Y. Wu, "Application of a Phenomenological Soot Model for Diesel Engine Combustion," in *ASME 2008 Internal Combustion Engine Division Spring Technical Conference*, Jan. 2008, pp. 205–214, doi: 10.1115/ICES2008-1629.

[71] J. L. Emdee, K. Brezinsky, and I. Glassman, "A kinetic model for the oxidation of toluene near 1200 K," *J. Phys. Chem.*, vol. 96, no. 5, pp. 2151–2161, Mar. 1992, doi: 10.1021/j100184a025.

[72] J. NAGLE and R. F. STRICKLAND-CONSTABLE, "OXIDATION OF CARBON BETWEEN 1000–2000°C," in *Proceedings of the Fifth Conference on Carbon*, Elsevier, 1962, pp. 154–164.

[73] M. Sirignano, J. Kent, and A. D'Anna, "Modeling Formation and Oxidation of Soot in Nonpremixed Flames," *Energy & Fuels*, vol. 27, no. 4, pp. 2303–2315, 2013, doi: 10.1021/ef400057r.

[74] J. Camacho, Y. Tao, and H. Wang, "Kinetics of nascent soot oxidation by molecular oxygen in a flow reactor," *Proc. Combust. Inst.*, vol. 35, no. 2, pp. 1887–1894, 2015, doi: 10.1016/j.proci.2014.05.095.

[75] P. R. Johnson, R. K. Chakrabarty, and B. M. Kumfer, "A modeling approach for soot formation in non-premixed flames with elevated stoichiometric mixture fraction," *Combust. Flame*, vol. 229, p. 111383, Jul. 2021, doi: 10.1016/j.combustflame.2021.02.029.

[76] A. Menon, J. W. Martin, J. Akroyd, and M. Kraft, "Reactivity of Polycyclic Aromatic Hydrocarbon Soot Precursors: Kinetics and Equilibria," *J. Phys. Chem. A*, vol. 124, no. 48, pp. 10040–10052, 2020, doi: 10.1021/acs.jpca.0c07811.

[77] A. Menon *et al.*, "Reactive localized π-radicals on rim-based pentagonal rings: Properties and concentration in flames," *Proc. Combust. Inst.*, vol. 38, no. 1, pp. 565–573, 2021, doi: 10.1016/j.proci.2020.07.042.

[78] E. Chemistry, "Introduction to Gaussian program 1," *Convergence*, no. 1993, pp. 1–17, 1999.

[79] A. Szabo and N. S. Ostund, *Modern quantum chemistry. Introduction to advanced electronic structure theory.* USA: McGraw-Hill, 1989.

[80] F. Jensen, *Introduction to Computational Chemistry*, 3rd ed. USA: John Wiley Sons, Inc., 2006.

[81] J. Foresman and a Frisch, "Exploring chemistry with electronic structure methods, 1996," *Gaussian Inc, Pittsburgh, PA*. 1996, [Online]. Available: http://scholar.google.com/scholar?hl=en&btnG=Search&q=intitle:Exploring+Chemistry+With+Electronic+Structure+Methods#1%5Cnhttp://scholar.google.com/scholar?hl=en&btnG=Search&q=intitle:Exploring+chemistry+with+electronic+structure+methods,+1996#1.

[82] B. A. Pettitt and W. Danchura, "Rovibrational momentum densities of diatomic molecules in the rigid rotor-harmonic oscillator approximation," *Chem. Phys. Lett.*, vol. 142, no. 6, pp. 455–462, Dec. 1987,

doi: 10.1016/0009-2614(87)80643-7.
[83] J.-M. Mouesca, “Density Functional Theory–Broken Symmetry (DFT–BS) Methodology Applied to Electronic and Magnetic Properties of Bioinorganic Prosthetic Groups,” 2014, pp. 269–296.
[84] D. Lunz, G. Batt, J. Ruess, and J. F. Bonnans, “Beyond the chemical master equation: Stochastic chemical kinetics coupled with auxiliary processes,” *PLOS Comput. Biol.*, vol. 17, no. 7, p. e1009214, Jul. 2021, doi: 10.1371/journal.pcbi.1009214.
[85] Y. Zhao and D. G. Truhlar, “The M06 suite of density functionals for main group thermochemistry, thermochemical kinetics, noncovalent interactions, excited states, and transition elements: Two new functionals and systematic testing of four M06-class functionals and 12 other function,” *Theor. Chem. Acc.*, vol. 120, no. 1–3, pp. 215–241, 2008, doi: 10.1007/s00214-007-0310-x.
[86] M. Walker, A. J. A. Harvey, A. Sen, and C. E. H. Dessent, “Performance of M06, M06-2X, and M06-HF Density Functionals for Conformationally Flexible Anionic Clusters: M06 Functionals Perform Better than B3LYP for a Model System with Dispersion and Ionic Hydrogen-Bonding Interactions,” *J. Phys. Chem. A*, vol. 117, no. 47, pp. 12590–12600, Nov. 2013, doi: 10.1021/jp408166m.
[87] J. Gräfenstein, E. Kraka, M. Filatov, and D. Cremer, “Can Unrestricted Density-Functional Theory Describe Open Shell Singlet Biradicals?,” *Int. J. Mol. Sci.*, vol. 3, no. 4, pp. 360–394, Apr. 2002, doi: 10.3390/i3040360.
[88] H. Nakata, D. G. Fedorov, S. Yokojima, K. Kitaura, M. Sakurai, and S. Nakamura, “Unrestricted density functional theory based on the fragment molecular orbital method for the ground and excited state calculations of large systems,” *J. Chem. Phys.*, vol. 140, no. 14, p. 144101, Apr. 2014, doi: 10.1063/1.4870261.
[89] R. S. Tranter, S. J. Klippenstein, L. B. Harding, B. R. Giri, X. Yang, and J. H. Kiefer, “Experimental and theoretical investigation of the self-reaction of phenyl radicals,” *J. Phys. Chem. A*, vol. 114, no. 32, pp. 8240–8261, 2010, doi: 10.1021/jp1031064.
[90] and M. P. Evans, Merdith G., “Some applications of the transition state method to the calculation of reaction velocities, especially in solution,” *Trans. Faraday Soc.*, vol. 31, pp. 875–894, 1935.
[91] R. S. Tranter, S. J. Klippenstein, L. B. Harding, B. R. Giri, X. Yang, and J. H. Kiefer, “Experimental and Theoretical Investigation of the Self-Reaction of Phenyl Radicals,” *J. Phys. Chem. A*, vol. 114, no. 32, pp. 8240–8261, Aug. 2010, doi: 10.1021/jp1031064.
[92] H. Jin, B. R. Giri, D. Liu, and A. Farooq, “A high temperature shock tube study of phenyl recombination reaction using laser absorption spectroscopy,” *Proc. Combust. Inst.*, vol. 38, no. 1, pp. 919–927, 2021, doi: 10.1016/j.proci.2020.06.164.
[93] A. Nobili *et al.*, “On the radical behavior of large polycyclic aromatic hydrocarbons in soot formation and oxidation,” *Combust. Flame*, p. 111692, Sep. 2021, doi: 10.1016/j.combustflame.2021.111692.
[94] El. RANZI, M. DENTE, T. FARAVELLI, and G. PENNATI, “Prediction of Kinetic Parameters for Hydrogen Abstraction Reactions,” *Combust. Sci. Technol.*, vol. 95, no. 1–6, pp. 1–50, Dec. 1993, doi: 10.1080/00102209408935325.
[95] El. RANZI, M. DENTE, T. FARAVELLI, and G. PENNATI, “Prediction of Kinetic Parameters for Hydrogen Abstraction Reactions,” *Combust. Sci. Technol.*, vol. 95, no. 1–6, pp. 1–50, Dec. 1993, doi: 10.1080/00102209408935325.
[96] “http://creckmodeling.chem.polimi.it/.” .
[97] “International Sooting Flame (ISF) Workshop.”
[98] A. D. Abid, N. Heinz, E. D. Tolmachoff, D. J. Phares, C. S. Campbell, and H. Wang, “On evolution of particle size distribution functions of incipient soot in premixed ethylene–oxygen–argon flames,” *Combust. Flame*, vol. 154, no. 4, pp. 775–788, Sep. 2008, doi: 10.1016/j.combustflame.2008.06.009.
[99] F. Xu, “Soot formation in laminar premixed ethylene/air flames at atmospheric pressure,” *Combust. Flame*, vol. 108, no. 4, pp. 471–493, Mar. 1997, doi: 10.1016/S0010-2180(96)00200-3.
[100] K. Gleason, F. Carbone, A. J. Sumner, B. D. Drollette, D. L. Plata, and A. Gomez, “Small aromatic hydrocarbons control the onset of soot nucleation,” *Combust. Flame*, vol. 223, pp. 398–406, Jan. 2021, doi: 10.1016/j.combustflame.2020.08.029.
[101] X. Xue, X. Hui, P. Singh, and C.-J. Sung, “Soot formation in non-premixed counterflow flames of conventional and alternative jet fuels,” *Fuel*, vol. 210, pp. 343–351, Dec. 2017, doi: 10.1016/j.fuel.2017.08.079.

[102] “https://linkinghub.elsevier.com/retrieve/pii/S0360128515300393.” .